Analytical techniques for reaction monitoring, mechanistic investigations, and metal complex discovery

by

Gilian T. Thomas
M.Sc. Chemistry, Carleton University, 2018
B.Sc. Biochemistry & Biotechnology, Carleton University, 2016

A dissertation submitted in partial fulfillment of the requirements for the degree of

Doctor of Philosophy

in the

Department of Chemistry

University of Victoria
Victoria, British Columbia

Analytical techniques for reaction monitoring, mechanistic investigations, and metal complex discovery

by

Gilian T. Thomas
M.Sc. Chemistry, Carleton University, 2018
B.Sc. Biochemistry & Biotechnology, Carleton University, 2016

Supervisory Committee

Prof. J. Scott McIndoe, Supervisor
Department of Chemistry

Prof. Christopher Gill, Departmental Member
Department of Chemistry

Prof. C. Peter Constabel, Outside Member
Department of Biochemistry

Abstract

A variety of analytical techniques are showcased for their ability to provide insights into reaction mechanisms as well as active intermediate speciation.

Pressurized Sample Infusion-Mass Spectrometry (PSI-ESI-MS), ion mobility-mass spectrometry (IMS-MS), and Nuclear Magnetic Resonance (NMR) spectroscopy are powerful analytical techniques capable of reaction monitoring. Contamination from vulcanized rubber was an issue with the PSI-ESI-MS technique as ions unrelated to the reaction were convoluting the mass spectrum. This was resolved by re-designing the PSI flask such that the septum was positioned above a condenser, preventing heat degradation of the septum and subsequent leaching of contaminants into the reaction solution. The technique was then used to analyze the Buchwald-Hartwig amination reaction in real-time. The innovative use of Multiple Reaction Monitoring (MRM) scans facilitated observation of all catalytic intermediates, and elucidation of relative reaction rates for each step of the catalytic cycle.

PSI-ESI-MS and NMR are complementary methods whereby catalytic intermediates are monitored via PSI-ESI-MS, and the rate of product formation is monitored via NMR spectroscopy. This combination of analytical methods was employed in the investigation of the Barluenga cross-coupling reaction between *N*-tosylhydrazones and aryl halides. A reaction screen revealed optimized homogeneous conditions, and the turnover limiting step was found to be off-cycle.

IMS separates gaseous ions based on their size and shape immediately prior to MS analysis. Upon investigation of $[PtCl_3(C_2H_4)]$, and $[PtCl_3(CO)]$, it was found that residual $[PtCl_3]$ was forming $[PtCl_3(N_2)]$ in the source of the instrument. Ion mobility was able to separate these isobaric ions, and DFT calculations and collision-induced dissociation experiments confirmed the existence of the gaseous $[PtCl_3(N_2)]$ complex.

NMR spectroscopy may also be employed as a strong reaction monitoring technique. The mechanism of C–H silylation by trimethyl(trifluoromethyl)silane and tetrabutylammonium difluorotriphenylsilicate was investigated using ^{19}F-NMR. All intermediates and reaction byproducts were quantitatively observed, and the reaction conditions were optimized. A stopped-flow NMR system was used to gather data points in the first 0.2 seconds of the reaction.

Contents

List of Figures

List of Tables

List of Schemes

List of Abbreviations

Å = Angstrom

CCS = Collisional cross section

CE = Collision energy

CID = Collision-induced dissociation

Da = Dalton

DC = Direct current

DME = Dimethoxyethane

ESI = Electrospray ionization

HAT = Hydrogen atom transfer

IMS-MS = Ion mobility spectrometry-mass spectrometry

IR = Infrared

KE = Kinetic energy

kJ = Kilojoules

kV = Kilovolts

m/s = Meters per second

MS/MS = Tandem mass spectrometry

m/z = Mass-to-charge ratio

MHz = Megahertz

MRM = Multiple reaction monitoring

MS = Mass spectrometry

NMR = Nuclear magnetic resonance

ppm = Parts per million

PSI = Pressurized sample infusion

RF = Radio frequency

RT = Room temperature

SET = Single electron transfer

SRIG = Stacked ring ion guide

TBAT = $[Ph_3SiF_2][Bu_4N]$

THF = Tetrahydrofuran

TMSCF$_3$ = Trifluoromethyltrimethylsilane

TOF = Time-of-flight

TWIMS = Travelling wave ion mobility spectrometry

Acknowledgments

I would first like to thank my committee for their contributions to this dissertation, and for giving me your time over the years.

The largest thank you goes to my supervisor Professor Scott McIndoe. Thank you for your words of wisdom and guidance throughout my PhD. I appreciate the independence to grow as a scientist, and the opportunity for improvement in all areas. Most of all, I appreciate that you always had my best interests in mind, and that you were always open to new ideas and discussion. Additionally, I would not have succeeded in publishing without Scott and my co-authors.

I would like to thank the Department of Chemistry administrative team, Sandra, Lori, Hiromi, Erin, and Cathy you've all been very helpful. Whether it's a simple print job, or a super complicated paperwork question, you always know what to do and ease my stress.

I'd like to thank my friends, both old and new, for being a pillar of strength. The tail-end of this PhD especially wouldn't have been nearly as much fun without Greg Gaube. You've been an incredible collaborator, and an even better friend. Our 6am gym sessions and Friday night drinks really got me through this last year of the grind. Thank you for always supporting me, believing in me, and encouraging me. And of course, thank you for reading/editing chapters of this dissertation. I'll definitely be pushing your wheelchair one day, old man.

I'd like to acknowledge my family as well for their patience and support. Dad, thank you for instilling this unbelievable work ethic. I would not be where I am today without it. Alison, the frequent cards of encouragement never ceased to lift me up and keep me going.

Dedication

Success necessitates sacrifice.

In acknowledgement of all the sacrifices I made to get here.

Chapter 1

Background

1.1 Mass Spectrometry

Joseph John Thomson created the first instrument capable of separating ions by their mass-to-charge ratio (m/z).[1,2] From there innovations to mass spectrometry (MS) have been highly extensive, however the fundamental principles remain constant. Mass spectrometers are made up of six essential parts: a vacuum source, an inlet for sample introduction, an ionization source, a mass analyzer, a detector, and a recorder. Ions are generated, separated by electric or magnetic fields based on their m/z, and detected. The resulting mass spectrum is a plot of abundance/intensity versus m/z.

Following its emergence in the early 1900s, mass spectrometry has quickly grown to be one of the most sensitive analytical techniques available. Its versatility, reliability, and robustness allow scientists to heavily rely on its detection capabilities in various contexts. Mass spectrometry applications range from the development and discovery of new pharmaceuticals, to overall molecular structure determination and characterization, and much more.

In order for an analyte to be detected by a mass spectrometer it must be charged. Several ionization methods have been developed to facilitate analyte ionization at atmospheric pressure. These ions must then be transferred into the mass analyzer under vacuum which leads to a loss of ions, however the ion yield of atmospheric pressure sources is higher compared to ionization sources under vacuum.[3] Soft atmospheric pressure ionization techniques generally do not cause fragmentation and are commonly used for weakly-bound analytes, such as cell extracts[4] and metal complexes.[5,6] Two of these soft ionization methods, electrospray ionization (ESI) and Matrix-assisted Laser Desorption Ionization (MALDI) provided the ability to probe biomolecules, and were eventually awarded the 2002 Nobel Prize in chemistry.

1.1.1 Electrospray Ionization

Introduced in 1968 by Malcolm Dole,[7] ESI has quickly grown to be one of the most popular ionization methods for mass spectrometry after seeing significant innovations by John Fenn almost two decades later.[8]

One of the main features of ESI is the desorption of solution-phase analytes into the gas phase under atmospheric conditions. Samples flow through a stainless steel capillary charged at a relatively high voltage, typically between 2 and 5 kV. A positive or negative charge is imparted on the analyte depending on the mode of analysis; in positive ion mode the capillary has a positive charge, and in negative ion mode the capillary holds a negative charge. Charges may be brought about on an analyte by constituting the analyte in acidic or basic solution for positive or negative mode analysis, respectively. Samples may also hold inherent charges on the molecule.

The charged sample solution experiences an electric field at the end of the capillary causing separation of the ions, and creating a Taylor cone at the tip (Figure 1.1). Charged particles are expelled from the Taylor cone, and the droplets travel toward the mass analyzer. As the droplets move through the chamber they are desolvated quickly, thus concentrating the charge within each droplet as the radius of the droplets decreases. The Coulombic repulsion within each droplet results in ejection of singular ions into the gas-phase when the Rayleigh instability limit is reached, and the ions

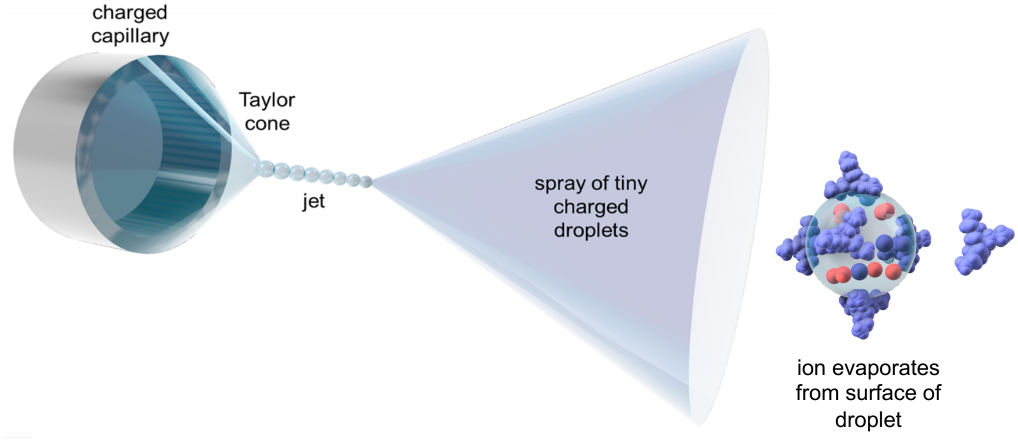

Figure 1.1: Electrospray ionization (ESI).

are drawn into the instrument by electric fields and reduced pressure.

Compared to other soft ionization methods, such as MALDI, ESI is well-equipped for analysis of small *m/z* analytes as the signal-to-noise ratio in the low *m/z* region of the spectrum is higher. Additionally, ESI can be coupled to a variety of mass analyzers, and/or liquid chromatography for further analyte separation.

1.1.2 Triple Quadrupole Mass Analyzer

One of the most common mass analyzers coupled to ESI is a triple quadrupole mass analyzer.[9] The quadrupole consists of four equally-spaced metal rods in parallel. Although named a ‘triple quadrupole’ the instrument often contains a hexapole collision cell, rather than a quadrupole, consisting of six rods as opposed to four. Radio frequency (RF) and direct current (DC) potentials are applied to the rods equal and opposite one another, i.e. a positive potential is applied to rods opposite each other in the x-direction and a negative potential is applied to the two rods opposite each other in the y-direction. Electric fields are applied to ions in the xz plane and the yz plane, forcing the ions to travel in the z-direction. If only RF potential is applied to the rods ions of every *m/z* will be transmitted through to the detector. However, when both RF and DC potentials are applied they switch rapidly between the rods allowing the quadrupole to act as a mass filter (Figure 1.2).

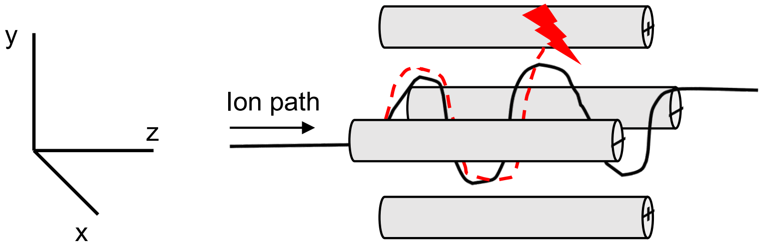

Figure 1.2: Schematic of a quadrupole mass analyzer with applied voltages, illustrating the ion path of a stable trajectory ion (black line), and unstable trajectory ion (red line).

A triple quadrupole instrument consists of three quadrupoles in succession: Q1, q2, and Q3. Q1 and Q3 are mass selective, while q2 is a collision cell and only experiences RF potential. The voltages applied to Q1 and Q3 ensure the selected m/z of all ions in a m/z range have stabilized trajectories throughout their journey. All m/z not selected will have unstable trajectories resulting in collision with the rods thus not be transmitted to the detector.

1.1.2.1 Tandem Mass Spectrometry

Tandem mass spectrometry scans (MS/MS or MS^2) are one of the main features of a triple quadrupole instrument. Collisions with inert gas in q2 facilitate fragmentation of ions, illuminating its structural properties in a process called Collision Induced Dissociation (CID).[3]

There are several types of MS/MS scans available, including product ion scans, precursor ion scans, and Multiple Reaction Monitoring (MRM) scans. Product ion scans involve Q1 set to select for a specific m/z and transferring only this m/z to q2, where it undergoes CID, and Q3 scans the m/z of all fragments. Precursor ion scans involve Q1 transmitting and scanning all m/z, ions are then fragmented in q2, and

Q3 is set to select for a specific m/z. The resulting spectrum displays the parent ion of the fragment selected for in Q3.

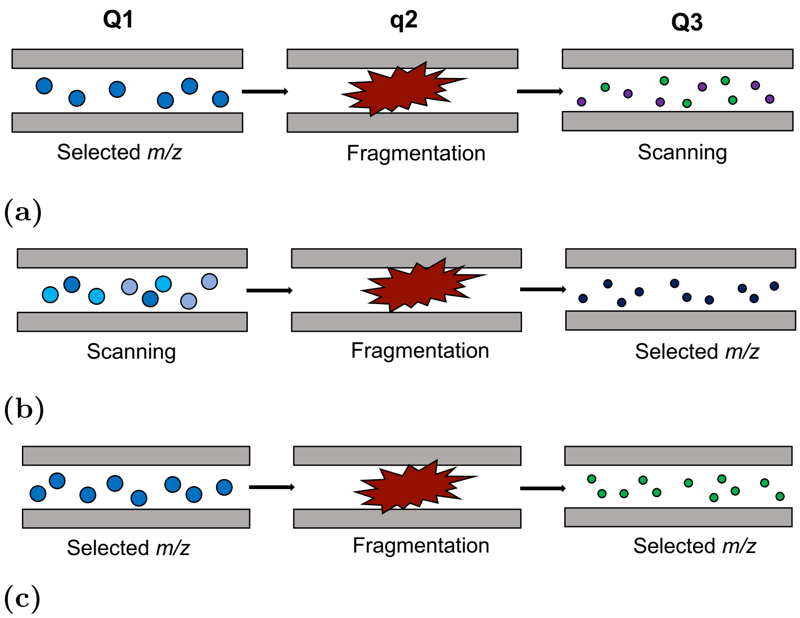

Figure 1.3: MS/MS schematic of (a) product ion scan; (b) precursor ion scan; and (c) Multiple Reaction Monitoring (MRM) scan. Colours represent various m/z.

While product ion scans and precursor ion scans aid in uncovering structural features of an ion, the primary objective of an MRM scan is sensitivity enhancement. Q1 is set to select for a m/z of interest, this ion is transferred into q2 where it is fragmented, and Q3 then selects for a specific fragment m/z produced during CID. By selecting for a single analyte in both Q1 and Q3 the signal-to-noise ratio is increased as all other m/z are filtered away. Additionally, the dwell time for each ion can be increased relative to the dwell time for a full scan.

1.1.3 Time-of-Flight Mass Analyzer

Recent advances in time-of-flight (TOF) technology and design have led to its increasing popularity. Its high resolution data output and compatibility with several ionization sources make it suitable for various analyses.

The overarching principles of TOF technology are based on the kinetic energy (KE) of ions as they travel through the drift region, related by the equation KE = $1/2mv^2$. Ions are accelerated by an electric field and then passed into the field-free drift region with a specific KE. Ions with lower KE travel at a slower velocity, and ions with higher KE travel at a higher velocity. The high resolution of the instrument is facilitated by orthogonal acceleration into the drift tube, high vacuum, as well as the introduction of the reflectron – one of the greatest advances in the TOF mass analyzer.[1]

The reflectron, also known as the ion mirror, is composed of several ring electrodes holding increasing potential situated at the opposite end of the drift region.[3] Ions are allowed to enter the reflectron region based on their acquired KE, so ions with higher velocity will penetrate the reflectron more deeply and spend more time in the reflectron region to ensure they reach the detector at the same time as ions of the same *m/z* with lower velocity (Figure 1.4). When the ions exit the reflectron their velocities are reversed allowing them to travel the length of the drift tube a second time, and all ions of the same *m/z* arrive at the detector simultaneously. Newer TOF instruments, such as the Waters Synapt G2-Si, are equipped with an elongated reflectron opposite the detector, and provide the option of engaging a second ion mirror on the same side of the drift tube as the detector. This hardware setup allows the ions to traverse the length of the TOF four times prior to detection, further increasing the resolution of the instrument.

The TOF analyzer is often sequentially combined orthongonally with a quadrupole mass analyzer to form a QqTOF instrument. In doing so mass filtering becomes an option, and some tandem MS experiments are available. QqTOF instruments combine the adaptability of the quadrupole with the high resolution of the TOF. These instruments are capable of performing MS/MS experiments, however are more limited than triple quadrupole instruments due to the lack of mass selectivity of a

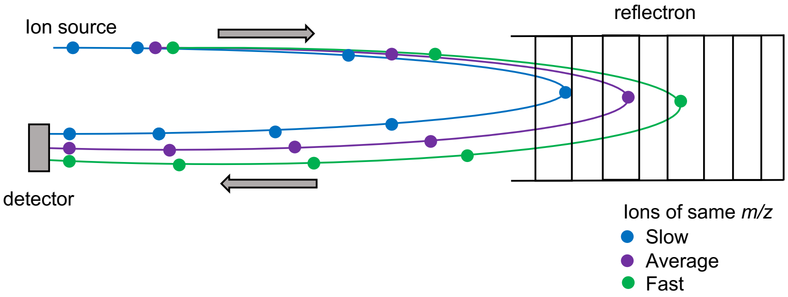

Figure 1.4: Time-of-Flight (TOF) mass analyzer equipped with a reflectron. Coloured lines represent respective ion trajectories.

TOF analyzer.

1.2 Ion Mobility Spectrometry

When ion mobility spectrometry (IMS) was first developed as a standalone instrument the ionization source was commonly ^{63}Ni.[10] The main principle of IMS is that it accelerates analytes in the gas-phase through an electric field, and simultaneously slows them using an inert gas to facilitate separation based on their collisional cross section (CCS).[11] The CCS is indicative of the size and shape of the analyte; for example, an unfolded protein would be more likely to travel slower through the drift tube because it experiences more drag compared to the folded version of the same protein. In this way IMS has proven itself to be a powerful analytical instrument capable of aiding in structure elucidation.[12–14] In practice the ions enter the drift tube as 'packets' and travel through the drift tube at a rate (m/s) proportional to the product of mobility and electric field.

The CCS of an analyte can also be modelled computationally. There are four ways to calculate the collisional cross section of an analyte: the trajectory method, the projection approximation method, the exact hard sphere scattering method, and the projection superposition approximation method.[15] The trajectory method is the simplest as it only takes into account long-range interactions between the analyte and the drift gas and determines the trajectories and scattering angle at which the gas molecules are deflected. The exact hard spheres method is based on the assumption that all of the atoms in the ion are hard spheres, and calculates the scattering angle from the trajectories the gas molecules are propelled through collisions with the analyte ion. The projection approximation method rotates the structure of the analyte through all possible orientations and generates a ‘shadow’ on a defined plane. Finally, the projection superposition approximation method calculates the collisional cross section of an ion very similarly to the projection approximation method, however the ion’s atoms are assumed to be soft spheres. This method is the most complex and expensive.

1.2.1 Travelling Wave Ion Mobility Spectrometry

A more recent advance in the field of IMS was the development of travelling wave technology (TWIMS). The same basic principles apply, however a DC voltage is pulsed through the stacked ring ion guide (SRIG) to create a traveling wave.[1] The SRIG is composed of ring electrodes arranged consecutively in a stack (Figure 1.5a).

Collisions with gas molecules inherently slow the ions as they experience collisional resistance, and as a result they often spend more time in the SRIG. The travelling voltage is superimposed to the RF voltage and causes the ions to follow the wave through the SRIG, thus reducing their residence time (Figure 1.5b).[16] The smaller residence time increases the number of ions transmitted through the drift cell. Separation is enhanced as low mobility ions will simply roll over the wave, while high mobility ions will keep up. The TWIMS technology effectively increases the duty cycle of the instrument, thereby increasing sensitivity.

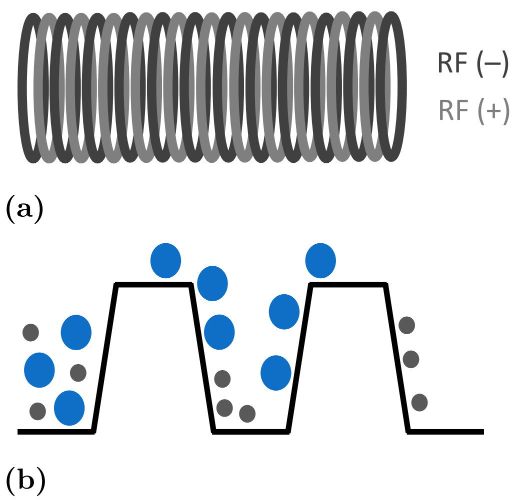

Figure 1.5: a) Stacked ring ion guide (SRIG) composed of electrodes creates the 'travelling wave' by pulsing voltage down the SRIG. b) Schematic of ion separation facilitated by the travelling wave.

1.2.2 Ion Mobility Spectrometry-Mass Spectrometry

As the technology has advanced, IMS systems have been coupled to mass spectrometers (IMS-MS) thus eliminating the need for an ionization source as MS is equipped with ionization sources of its own, e.g. ESI.[12,17] In combination with an MS, IMS allows for analytes holding the same m/z value to be separated and differentiated based on their structural features (Figure 1.6). The system functions similar to a chromatographic separation, but on a seconds timescale as opposed to minutes.

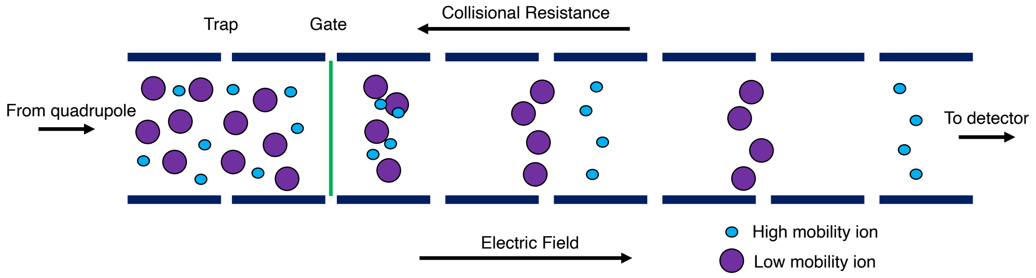

Figure 1.6: Schematic of ion mobility separation in an IMS-MS instrument.

The instrument used in this dissertation was equipped with an ion guide prior to a quadrupole mass filter, followed by the IMS drift tube (Figure 1.7). The IMS section of the instrument is divided into three parts: the trap, the IMS drift tube, and the transfer cell. The SRIG trap gathers ions as they emerge from the quadrupole to ensure they enter the drift tube simultaneously. When the gate opens the ions are permitted entry into the IMS drift tube where they are separated. Ions are then gathered in the SRIG transfer cell before moving into the TOF. This instrument is not equipped with a collision cell, rather MS/MS experiments can be done by performing CID in the trap and/or SRIG transfer cell after selecting the analyte m/z in the quadrupole as these cells are equipped with inert gas.

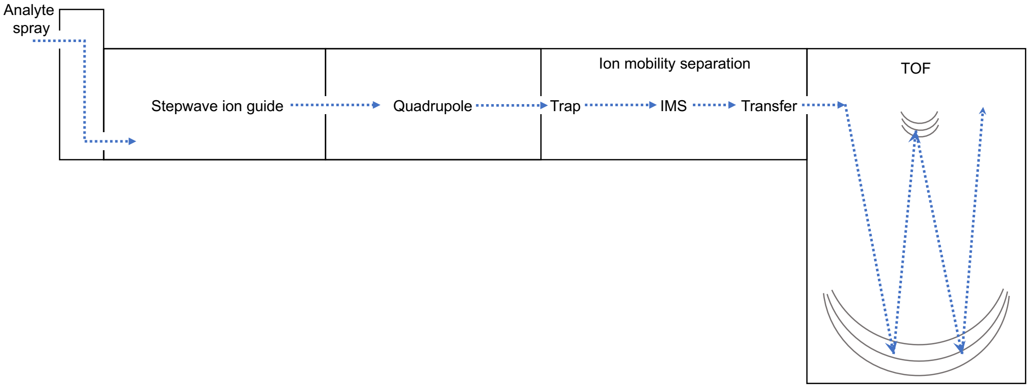

Figure 1.7: Schematic of a Waters Synapt G2-Si IMS-QqTOF instrument.

1.3 Nuclear Magnetic Resonance Spectroscopy

One of the most common analysis methods is nuclear magnetic resonance (NMR) spectroscopy. Its structure elucidation capabilities have aided researchers over the years, and its applications are ever-evolving.[18]

When a sample is placed into an NMR instrument it experiences a strong magnetic field, and nuclei with magnetic moments have a tendency to align with the applied magnetic field.[19] This allows the nuclei to absorb energy, and they are said to be in 'resonance' with the magnetic field. Each resonance generates a signal on the spectrum at a specified chemical shift (δ) measured in parts per million (ppm), one for each magnetically distinct nuclei. If a nucleus is in the same region as another nucleus, the electron cloud surrounding each nucleus is felt by all other nuclei in the vicinity, thus influencing the position of the resonance on the spectrum. Additionally, the magnetic field it experiences is no longer equal to the applied magnetic field. These will often result in a split signal reflecting the number of adjacent nuclei, and the nuclei are said to be ‘coupled’.

The area under each peak observed in the NMR spectrum can be integrated as this area is proportional to the number of protons present at that chemical shift. The integration values can be used to calculate the concentration of an analyte relative to an internal standard.

The resolution of an NMR instrument is dependent on the magnetic field strength of the instrument, typically this can range from 60 MHz to 800 MHz. These units refer to the frequency at which a proton will resonate in the applied magnetic field. Low resolution instruments produce broad peaks compared to high resolution instruments, and often signals overlap with one another. However, the chemical shift value of a nucleus will remain constant regardless of the spectrometer used.

1.4 Catalytic Reaction Monitoring

Observing reaction progress over time has become progressively more important as scientists attempt to optimize product generation in terms of time, materials, and yield. Offline reaction monitoring can become problematic when short-lived intermediates are present, or the reaction kinetics are very fast. Several methods exist to facilitate online monitoring of catalytic reactions,[20–24] and the primary techniques used throughout this dissertation are Pressurized Sample Infusion (PSI) and stopped-flow NMR.

1.4.1 Pressurized Sample Infusion

Portions of this section have been reproduced from G.T. Thomas, S. Donnecke, I.C. Chagunda, J.S. McIndoe,"Pressurized Sample Infusion", *Chemistry Methods*, accepted October 2021. Gilian Thomas completed the literature review and video of the PSI set-up. S. Donnecke produced the following sections: interpretation of time course data, as well as normalization. I.C. Chagunda produced the filtration section. The manuscript was written collaboratively by Gilian Thomas and Prof. Scott McIndoe.

HPLC is one of the most common ways of introducing sample into the mass spectrometer as it separates analytes by flowing through a column, and allows for small volume injections.[25] Syringe pumps may also be used as they are compatible with a multitude of solvents and facilitate sample introduction at a set flow rate (typically lower than HPLC flow rates); however in terms of reaction monitoring, temperature and solution mixing are relatively uncontrollable.[26] Mass spectrometers may be connected to a microreactor, however each data point is collected in a separate experiment.[27,28] A pressurized sample injection bomb apparatus capable of cleanup has been described with pneumatic control.[29] Flow injection systems have also been developed to facilitate sample delivery on a nL/min and µL/min scale enabling injection of up to 1200 samples per day without carryover.[30]

In terms of air- and moisture-free sample introduction, some techniques have been described whereby a nitrogenous atmosphere is either attached to the MS source, such as a glove bag[31,32] and a small glove chamber.[33] On a larger scale, a glovebox can be modified to accommodate a feedthrough port for tubing going directly into the MS source.[34,35] The need for a simple, cheap, robust method of air- and moisture-free sample introduction was obvious, hence the development of Pressurized Sample Infusion (PSI).[36]

Description of the Method

First reported in 2010, pressurized sample infusion (PSI) is a sample introduction method providing online reaction monitoring of reaction solutions.[36] It is essentially a positive pressure cannula transfer[37] of a reacting solution directly into an electrospray ionization mass spectrometer (ESI-MS). It does not require mechanical pumping, and infuses a raw reaction mixture without further treatment. ESI-MS is a technique limited to the analysis of species that carry a charge or are readily able to acquire one (e.g., a molecule with a basic site that can associate with a proton or an alkali metal ion) since it is capable of detecting only ions pre-formed in solution. It is also best suited to species present at very low concentration. With those two principal restrictions in mind, ESI-MS is especially well suited to systems involving charged catalysts.[38] When a charged catalyst is not an option, charged-tags are often used to apply a charge to a species of interest, with the reactivity of these charged-tags observed using PSI-ESI-MS.[39–41]

In terms of concentration limitations, the level of response yielded by ESI-MS is dictated by the nature of the analyte under study. For anything that carries a permanent charge, concentrations should be kept to low millimolar and below. If that species is also lipophilic and rigid (i.e. highly surface active and hence prone to be disproportionately found on the surface of the sprayed droplets and overrepresented in the mass spectrum),[42] that concentration should be micromolar or lower. Species that are not charged can generally be run at higher concentrations, but such species exhibit variability not just in surface activity but also in extent of ionization.[43–52] Bases can be readily protonated and acids deprotonated, giving good response factors, but neutral molecules lacking any such sites will generally be invisible to ESI-MS. The addition of a tee-piece connector can also be added to dilute the concentration of solution injected.[53,54]

ESI-MS solvents need to be reasonably polar in order to enable the electrochemistry that creates the excess charge for the ESI process.[55] Non-polar solvents are widely known as incompatible with ESI-MS due to their low conductivity, however addition of a lipophilic ionic liquid (a supporting electrolyte) can overcome this problem.[55] Aspects to take into consideration if using an ionic liquid to facilitate ESI performance: (1) it must be unreactive towards any of the reaction components, and (2) it should not overlap with any signals of interest.

The PSI approach works at temperatures up to the boiling point of the solvent. Temperatures higher than the boiling point will overpressurize the flask. PSI can operate at lower temperatures than ambient, however unless insulated tubing is used, the utility of this is limited by the fact that the tubing and ESI source will be at room and elevated temperature, respectively, and so the reaction will be briefly exposed to these raised temperatures. As such, temperatures below 0°C are not recommended unless the reaction of interest is relatively slow.

PSI is conducted at slightly above ambient pressure, by 2-5 psi (0.14-0.34 bar). More highly pressurized systems are not recommended without use of a pressure vessel with the appropriate safety features (and a narrower diameter tubing to decrease the flow rate to something compatible with ESI-MS). Regulated tanks of N_2 or Ar are commonly used to deliver the positive pressure to the flask, though other options are available. Using a balloon filled with gas, samples can be prepared on a Schlenk line and then safely transferred to the mass spectrometer for sample introduction.[56] This method also introduces more versatility to the PSI technique as any gas can be used to fill the balloon. A single balloon supplies about 1 psi; double-walled balloons can provide increased pressure if required.

PSI-ESI-MS is most useful for providing temporal intensity profiles for every charged component of the reaction.[57] These profiles correspond to reactant, product, pre-catalyst, catalyst and reaction impurities, intermediates, decomposition products, and resting states (Figure 1.8). Based on the behaviour of analytes over time, their role in the reaction can be defined. This sample introduction method becomes even more powerful when combined with computation, which can provide further structural information and bond dissociation energies.[58,59]

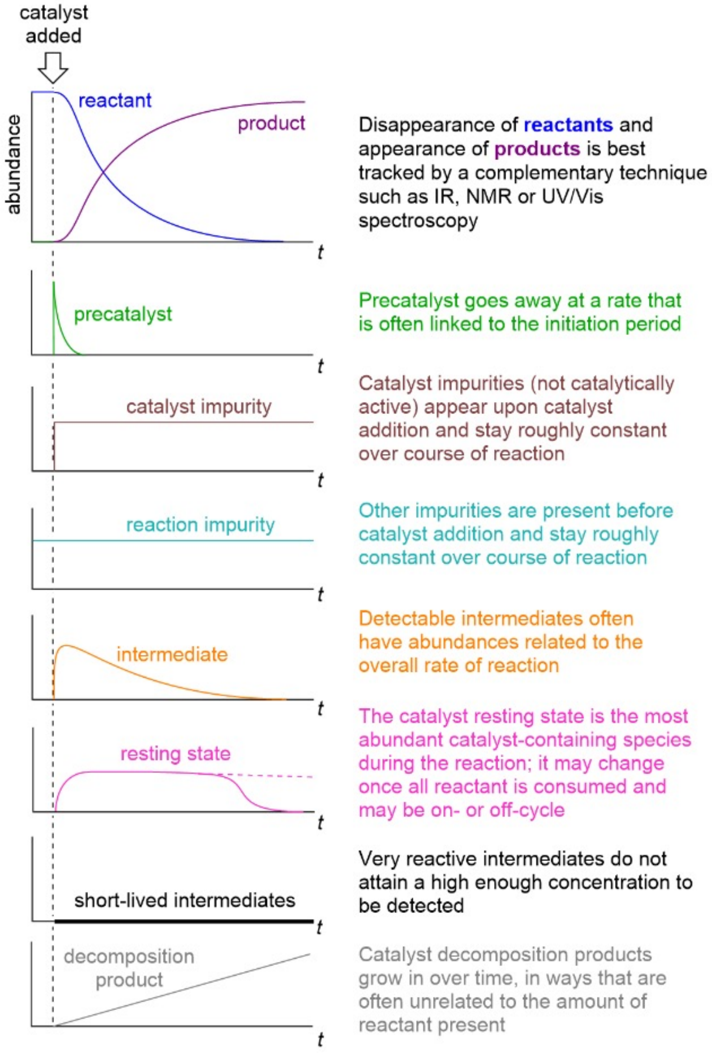

Disappearance of **reactants** and appearance of **products** is best tracked by a complementary technique such as IR, NMR or UV/Vis spectroscopy

Precatalyst goes away at a rate that is often linked to the initiation period

Catalyst impurities (not catalytically active) appear upon catalyst addition and stay roughly constant over course of reaction

Other impurities are present before catalyst addition and stay roughly constant over course of reaction

Detectable intermediates often have abundances related to the overall rate of reaction

The catalyst resting state is the most abundant catalyst-containing species during the reaction; it may change once all reactant is consumed and may be on- or off-cycle

Very reactive intermediates do not attain a high enough concentration to be detected

Catalyst decomposition products grow in over time, in ways that are often unrelated to the amount of reactant present

Figure 1.8: Idealized temporal profiles for different reaction components over the course of a reaction. These dynamics provide important clues as to which reaction role a given species is most likely playing. Adapted from Theron et al.[57]

The ability to acquire data on catalyst resting state and overall reaction progress simultaneously is a significant advantage of the technique and can be improved further via combination with orthogonal methods. Because MS is so sensitive, it is generally best suited to analyze reaction components at low concentration (e.g. species related to the catalyst) while the orthogonal method takes care of overall reaction progress by tracking the disappearance of reactant(s) and/or appearance of product(s). Flow infrared spectroscopy (IR) is an ideal candidate for this type of analysis (Figure 1.9).[57]

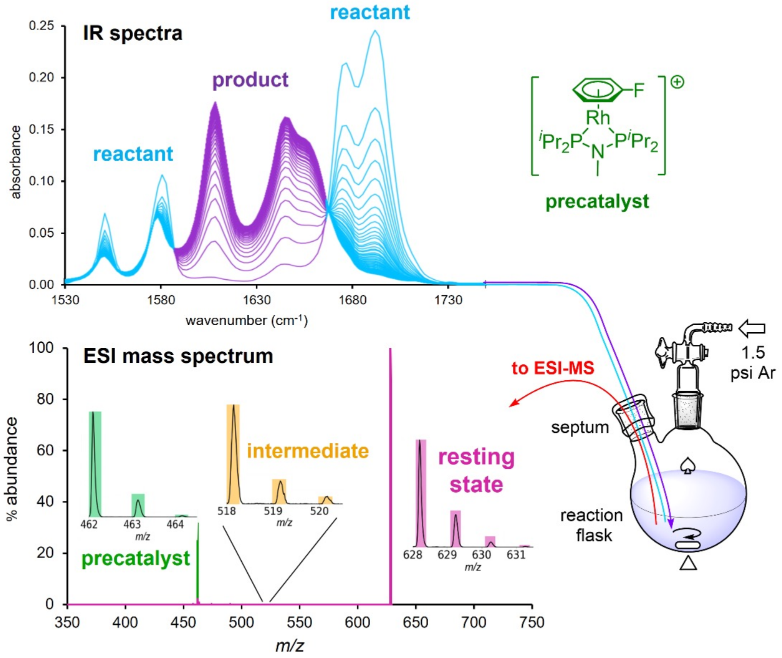

Figure 1.9: Combination of continuous monitoring methods[57] to obtain IR and MS data for a hydroacylation reaction. From the same flask, tubing circulates the reaction solution through a flow FTIR spectrometer (top), and PEEK tubing exits into the mass spectrometer (bottom).

There is some dead time between the solution leaving the flask and arriving in the mass spectrometer, in the order of 5-20 seconds. Variables here include the viscosity of the solvent, the inner diameter of the tubing, the length of the tubing and the applied pressure. An estimate of flow rate can be established using the Hagen-Poiselle equation.[60,61] This dead time sets a lower bound for establishing reaction rates to a $t_{1/2}$ of 20 seconds or more. The upper bound is set only by practical limitations such as the volume of solvent available (solvent is consumed at typical rates of 5-20 µL/min), the booking of instrument time, and the increased likelihood of clogging and instrumental contamination from an extended analytical run. In practice, optimal results are obtained by running experiments that last 5-30 minutes, and in order to work in this time frame, manipulation of reaction rate is recommended (most routinely by increasing temperature or catalyst loading).

The PSI-ESI-MS methodology can be combined with any type of mass analyzer. When using a quadrupole time-of-flight (Q-TOF) spectrometer precision to four decimal places is obtained, yielding accurate mass identification of analytes.[62–66] Triple quadrupole instruments provide a lower level of resolution, however analyte identification can be confirmed via collision induced dissociation whereby fragments are created via collisions with gas molecules. The resulting fragments can be used to create multiple reaction monitoring (MRM) transitions effectively eliminating structurally different isobaric species, and analytes of interest can be observed in real-time when coupled with PSI.[67] This method is demonstrated in Chapter 3.

Detailed Experimental Setup

A Schlenk flask is placed close to the ESI source and is equipped with a rubber septum over the ground glass joint, and a rubber hose on the arm. The rubber hose is connected to a regulated cylinder of N_2, or other inert gas. The rubber septum is punctured with PEEK tubing extending into the reaction mixture, and the other end of the tubing is attached to the ESI source with a PEEK fitting (fingertight). If the septum is tough to puncture with the PEEK tubing, first puncture the septum using a needle approximately the same width as the outer diameter of the tubing. After removing the needle, the PEEK tubing will fit through the hole in the septum. For heated reactions, a two-neck flask may be equipped with a condenser, or a specialized PSI flask with a built-in condenser may be used (Figure 1.10).[68] A stir bar may be placed into the flask with reactants to ensure homogenous mixing. If reagents are not added to the flask inside a glovebox or on a Schlenk line, they are added via syringe through the rubber septum. Beware the positive pressure in the flask will force the syringe plunger away from the flask; this is prevented by holding a finger over the plunger while the needle is inside the flask. It is strongly recommended that the charged component of the reaction is added to the flask first, and the reaction initiated by adding neutral reactants. This precaution allows for optimization of ESI-MS conditions (spray quality, ion current) before the reaction is underway.

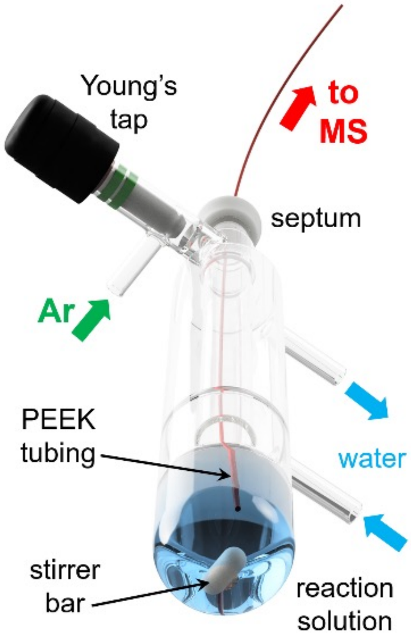

Figure 1.10: PSI flask equipped with condenser, adapted from McIndoe and coworkers.[68]

The reaction solution must flow through fittings with small internal diameters, so even though the PSI setup is simple it is nonetheless vulnerable to plumbing issues. The inner diameter of the tubing, union and stainless-steel capillary are extremely small and can be easily blocked, especially if the reaction mixture is heterogeneous. Blockages can be prevented by regular thorough cleaning/rinsing of these parts, and by using a homogeneous solution. If a blockage is present a distinct spray pattern will present itself. The instrument will abruptly sense little to no ions, and then all of a sudden resume normal activity. This spray pattern may happen frequently or periodically depending on the severity of the blockage. When this occurs simply disconnect the adapters and clean them before resuming the experiment as the data output will be inaccurate while a blockage is present. In severe cases where this mode of action does not rectify the issue, the capillary should be removed and sonicated in appropriate solvents.

As in a cannula transfer, solutions may be filtered by securing filter material on the end of the tubing in the reaction flask. In such cases, the end of the capillary can be protected with (a suitably cut) filter paper, cotton wool, glass wool or any other filter material, and secured by use of teflon tape. An example is illustrated in Figure 1.11. Here standard filter papers (Whatman, 55 mm) are used with standard density PTFE sealant tape to secure the filter paper to PEEK tubing. The general steps for attaching the filters are shown, with the filter paper first cut into a T shape (Figure 1.11, panel 2-3) and fit over the capillary opening. The stem of the paper is then folded over the capillary opening, with each arm then wrapping around the stem and capillary tube (Figure 1.11, panel 4-6). A strip of PTFE tape is then used to secure the filter and seal the capillary tubing, which can be inserted into the reaction flask (Figure 1.11, panel 7-9). It is important to avoid compromising flow rate or retention time, so using a minimal amount of filter material is desirable.

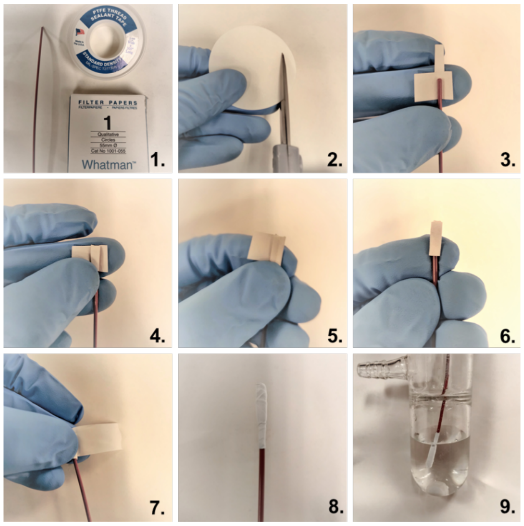

Figure 1.11: Preparation of paper filter for PSI PEEK tubing

The effects of filtration on the PSI flow rate were tested, with the results illustrated in Figure 1.12. A PSI flask was set up as described in Figure 1.10, however the end of the tubing that would be attached to the ESI source inlet was instead suspended above a flask that was placed on an analytical balance. The mass of solution flowing from the PEEK tubing was measured as a function of time, providing the PSI flow rate. A control trial with a homogeneous solution (THF) and no filtration (green) resulted in a consistent flow rate. In contrast, for a fine suspension (purple) (K_3PO_4 in THF), the flow rate is seen to drastically drop after a minute of monitoring, indicating presence of a blockage. By attaching the filter described in Figure 1.11, clogging is effectively prevented.

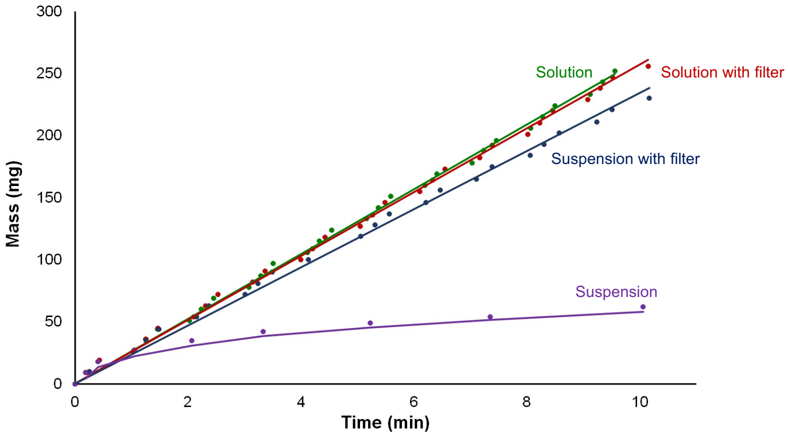

Figure 1.12: Mass of solution (mg) vs. time (min), illustrating the effect of attaching a filter to PEEK tubing in a heterogeneous reaction solution.

Positioning of the tubing in the stirred solution can also have an effect on clogging issues, so placing it away from and above any circulating solid material is advised. For example, if the solid material is floating near the top of the reaction solution, place the PEEK tubing at the bottom of the flask. Decomposition of reaction components can often lead to the generation of precipitated material, and this problem can be consequential in terms of creating blockages. Reactions that produce solids, gels or polymeric material should be similarly approached with caution.

Interpretation of Time Course Data

The resulting mass spectrum produced by PSI-ESI-MS is a reflection of how the ionic components of the reaction mixture changes over time. The total ion chromatogram (TIC) is a sum of the abundance of all ions detected by the instrument over time. Extracted ion chromatograms (XIC) of each analyte displaying the abundance of a single ion over time can also be produced. The TIC always contains a certain amount of noise, as does the intensity vs time traces of individual ions, but the ratio between various ions is much more consistent than the absolute intensity. As such, each point in the chromatogram can be normalized to report the relative abundance of relevant reaction species (Figure 1.13). This is done by dividing the XIC intensity by the TIC intensity, and multiplying this quotient by 100 to obtain a percentage. These experiments are data dense in that each point in a chromatogram corresponds to its own mass spectrum. Scan times usually run on the order of milliseconds, thus several spectra are being produced each second. After normalization, the calculated relative abundance of all species of interest can be plotted versus time. Spectra can be improved further by normalizing to the sum of all of the species of interest (thereby ignoring contributions from noise and background ions). A variety of software is available to facilitate this process, including but not limited to PythoMS,[69] Origin, and Microsoft Excel.

Note the improvement in data quality upon normalization. This particular reaction is prone to decomposition of the excess reagent $Co_2(CO)_8$, which produces the much less soluble $Co_4(CO)_{12}$ upon heating. It is this insoluble byproduct that causes the glitching in the TIC and the apparent decay in ion count. There are other reasons why the TIC may not be flat, including charge neutralization, generation of new charged species, large changes in response factor of product compared to reactant. Checking the other ion mode is advisable in cases when the TIC shows strange behavior, because clues to the origin of that behavior can often be found there.

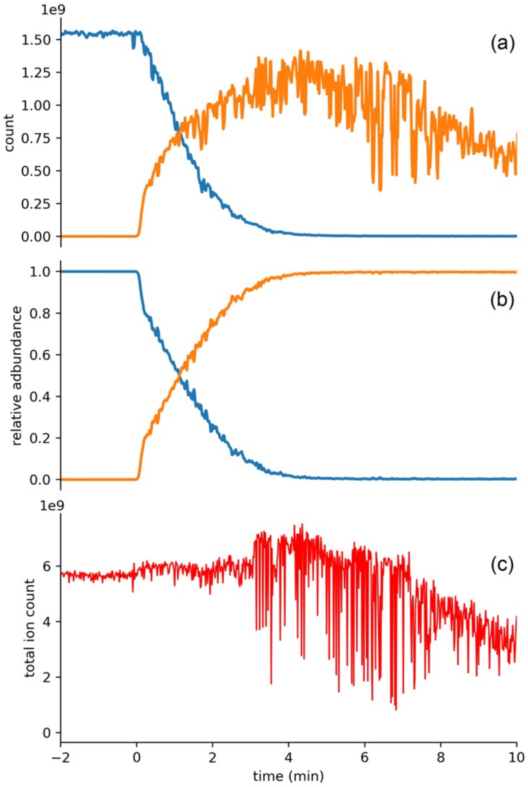

Figure 1.13: PSI-ESI-MS data depicting the effects of normalization. a) raw intensity vs. time data for a reaction between an alkyne and $Co_2(CO)_8$; b) normalization of the data in (a); c) total ion current (TIC).

Saturation

The sensitivity of ESI-MS can be a double-edged sword: it is fantastic for measuring low abundance species, but it is poorly suited to handle high or even moderate concentrations of molecules that easily ionize (or permanently charged ions). Saturation distorts spectra by reducing the apparent intensity of the most abundant ions, and there are a number of clues that saturation is occurring. Individual peak shapes are often distorted (square-topped peaks, broad peaks) and isotope patterns often provide poor matches to calculated patterns. The fact that saturation affects peaks of different intensities in different ways offers a quick check of whether saturation is occurring or not: simply generate a time course profile for one of the smaller peaks in the isotope pattern, and see if it changes shape (it will inevitably have a lower signal-to-noise ratio).[70] Figure 1.14 depicts a reaction profile whereby the reagent saturates the spectrum. It is clear that the M and M+1 traces differ from one another, and the M+2 is similar to the M+1 trace, though predictably it has a lower signal-to-noise ratio.

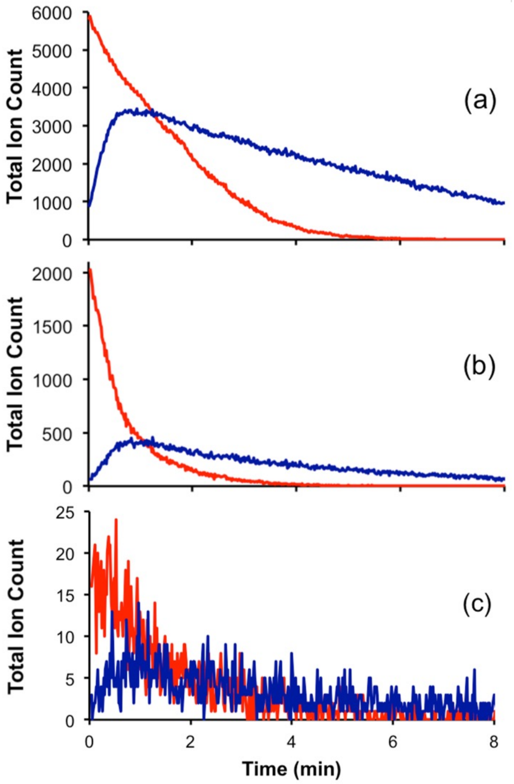

Figure 1.14: Representative saturation PSI-ESI-MS traces for (a) M, (b) M+1 and (c) M+2. The red trace is the reagent, and the blue trace is one of the products. Adapted from Wei et al.[71]

In terms of mitigating saturation, it is not always as easy as "make the solution more dilute". This precaution can slow the reaction down to the point where it is no longer examinable on a desirable time scale or even more problematically, increased decomposition at low concentration. There are also often limits to how much the reaction can be accelerated in compensation for lower concentration by heating and/or increasing catalyst loading. ESI-MS is sufficiently sensitive that it is relatively easy to detect analytes at concentration levels similar to the amount of residual oxygen and moisture present in even carefully dried solvent (approx. 5 ppm). Expecting good results when reactive contaminants are present at stoichiometric levels is not realistic, so high concentrations are often employed simply to reduce the proportion of decomposition observed. As such, saturation is a problem often encountered by the chemist working on air- and moisture-sensitive materials. Detuning instrument sensitivity by a variety of different methods (reducing capillary voltage to lower the amount of excess charge created, increasing the flow of cone gas to blow away ions from entering the mass spectrometer, increasing capillary to cone distance, damping the detector sensitivity) may be necessary.[71] This sort of trade-off (avoiding saturation vs. decomposition) has to be done carefully while checking that the relative response to different ions is not significantly perturbed.[42,72]

Applications in Organic Reaction Monitoring

A [3+2] cycloaddition/oxidation/aromatization reaction responsible for synthesis of bioactive pyrrolo[2,1-a]isoquinolines and indolizino[8,7-b] indoles was studied continuously for 6 h using the PSI-ESI-MS method to elucidate the mechanistic intermediates in the reaction where a green catalytic system (tetrabutylammonium iodide (TBAI)/tertbutyl hydroperoxide (TBHP)) was used in the reaction.[73] In this case a charged-tag was not needed as the zwitterionic intermediates were in equilibrium with their protonated form. The intermediates of the environmentally-friendly reaction were successfully monitored, and characterized using PSI-ESI-MS/MS.

A Ritter-type reaction involving menthol, $CuBr_2$, $Zn(OTf)_2$, Selectfluor©, and acetonitrile resulting in C–H amination of secondary and tertiary C–H bonds was reported in 2012 by Baran et al.,[74] and studied in real-time by Zare et al. in 2018.[75] The PSI-ESI-MS technique facilitated proposal of a more thorough mechanism via observation of several reaction intermediates, and exposed two mechanistic pathways whereby one pathway occurs in bulk solution and the other pathway occurs in microdroplets. The microdroplets created in ESI-MS allow for H^+ to accumulate on the surface of the droplet thereby promoting acid-catalyzed reactions despite the absence of acid, and such conditions are required to create the intermediate observed in the microdroplet mechanism. (Figure 1.15).

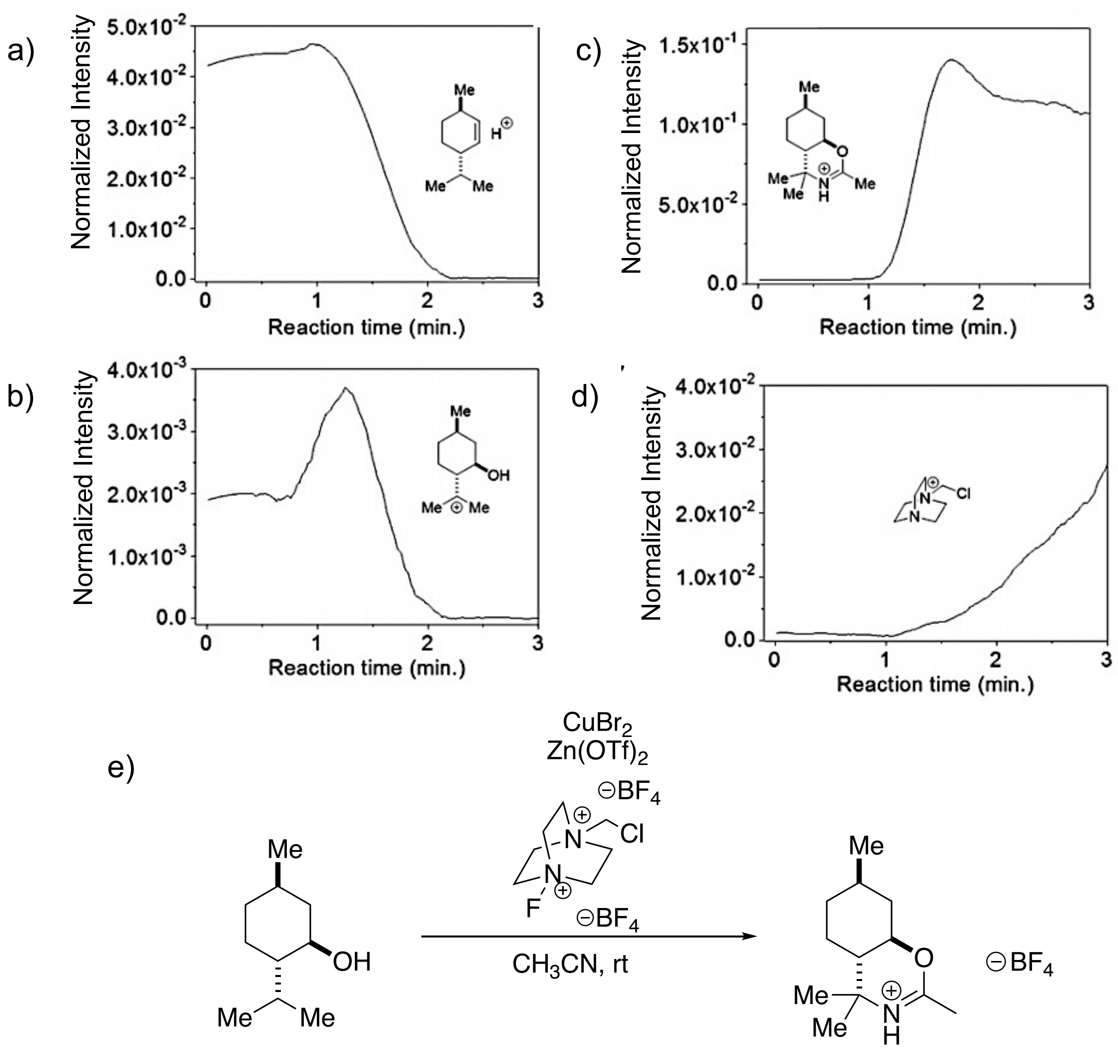

Figure 1.15: PSI-ESI-MS monitoring of a C–H amination reaction using $CuBr_2$, $Zn(OTf)_2$ and Selectfluor© in acetonitrile. a) Starting material; b) cationic intermediate; c) product; d) reduced Selectfluor© byproduct; e) C–H amination reaction conditions. Adapted from Zare and coworkers.[75]

Vicent and Gusev's 2016 study of acceptorless dehydrogenative coupling (ADC) of alcohols sings praise for the PSI technique stating that "[PSI] has proved to be ideal for in situ analysis of complex mixtures formed during catalysis".[76] Their research highlighted several intermediates in the reaction, and used CID to facilitate structure elucidation in combination with isotope patterns.

Applications in Catalysis

Mechanistic analyses has long been of significant interest in the community, and PSI-ESI-MS has been an extremely useful tool in uncovering reaction intermediates,[59,77–81] as well as kinetic profiles.[82–84] Several examples are described here.

Mack et al. discovered the degradation mechanism of their $[(\text{dtbpy})_2\text{Ru}(\text{CO}_3)]$ pre-catalyst using PSI-ESI-MS.[85] It was discovered that the catalyst activity can be inhibited by dimerization and ligand dissociation. Upon further PSI-ESI-MS probing it was determined that catalyst dimerization only played a minor role in inhibition, and that ligand dissociation was mostly responsible for limiting turnover. The authors were also able to elucidate the mechanism of this ligand dissociation process.

McIndoe and coworkers investigated the Suzuki-Miyaura reaction in positive and negative ion mode using charge-tags to ensure observation of each intermediate.[86] Their results indicate that at least two mechanisms are at work in the reaction. Further mechanistic work was done by the group on the Pauson-Khand reaction involving the $\text{Co}_2(\text{CO})_8$ catalyst as well as a charged alkene to track the progress of both intermolecular and intramolecular reactions.[87] The rate determining step in the reaction was revealed to be CO dissociation, and it was concluded that the nature of the alkene does not play a role in catalyst coordination.

The Newman group investigation of chemoselectivity in the Kumada-Corriu cross-coupling reaction employed PSI-ESI-MS to determine the mechanism of the reaction during slow addition of PhMgBr (Figure 1.16).[88] The catalytic cycle consists of oxidative addition, transmetalation of PhMgBr, and reductive elimination. If the Grignard reagent is added faster than the oxidative addition product (ArPdCl) is formed, the reactive PhMgBr will quench the excess aryl halide and create side products. During real-time analysis the concentration of side products was significantly decreased when the Grignard reagent was added slowly over the course of 1 h, versus a faster 5 min addition. It was concluded that the oxidative addition product must be present to prevent the PhMgBr from reacting with another species, and as a result the yield of desired product was increased.

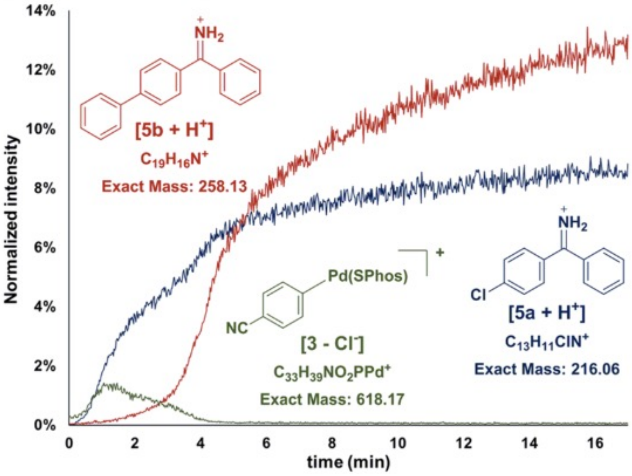

Figure 1.16: Real-time PSI-ESI-MS analysis of the Kumada-Corriu cross-coupling between PhMgBr and chlorobenzonitrile with fast addition of PhMgBr. Adapted from Newman et al.[88]

A mechanistic examination of the copper-mediated conversion of arylboronate esters into aryl fluorides was conducted by Hartwig and co-workers.[89] In this case, PSI-ESI-MS facilitated identification of a copper(III) fluoride product in solution as it was not isolatable.

An eco-friendly catalyst system of tetrabutylammonium iodide/tert-butyl hydroperoxide was explored in forming pyrrolo[2,1-a]isoquinolines and indolizino[8,7-b]indoles, both products holding pharmaceutical significance.[73] The intermediates involved in the [3+2] cycloaddition/oxidation/aromatization cascade reaction were identified for the first time using the PSI-ESI-MS technique. The identity of key intermediates was confirmed using ESI-MS/MS.

Alcohol oxidation, oxygen activation, and H_2O_2 disproportionation reactions were examined in real time using PSI by Waymouth and coworkers (Figure 1.17).[90] Combined with isotope-labeling and kinetic studies, key reaction intermediates were identified in reaction mechanisms occurring simultaneously – some multinuclear! The study opened up new avenues for exploration of oxygenation chemistry with palladium.

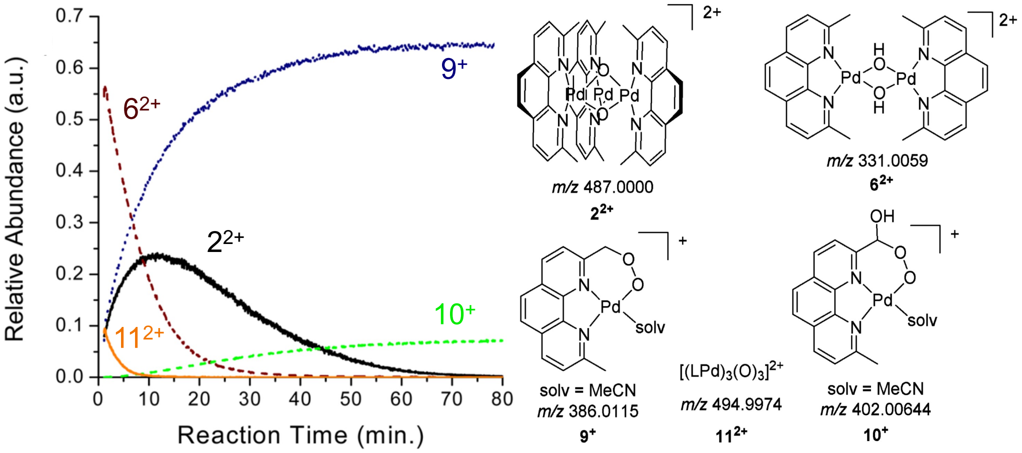

Figure 1.17: Left: PSI-ESI-MS monitoring of an H_2O_2 disproportionation reaction with $[(LPd(OAc)]_2(OTf)_2$ (L =2,9-dimethyl-1,10-phenanthroline. Right: proposed structures of speciation. Adapted from Waymouth and coworkers.[90]

A look into palladium/diene-catalyzed coupling of alkyl halides and Grignard reagents revealed that anionic Pd complexes are formed, and the mononuclear species are short-lived – mainly favouring formation of small Pd nanoclusters.[91] The real-time MS analysis afforded direct aggregation state information as well. Additionally, the study discovered that the transmetalation step in these reactions actually precedes the oxidative addition step in the catalytic cycle.

PSI-ESI-MS has also proven useful for Belli et al. in comparing the affinity of select secondary and tertiary phosphines for cationic ruthenium.[92] Competitive substitution reactions were analyzed in real time to assess the relative binding strength and measure the relative kinetics. A dissociative mechanism for substitution of NCPh with secondary phosphines on $[Ru(\eta^5\text{-indenyl})(NCPh)(PPh_3)_2]^+$ was revealed, as well as reaction kinetics. When comparing steric and electronic effects, the authors discovered that steric hinderance of the secondary phosphine plays a prominent role. In contrast, tertiary phosphines were found to produce multiple products as the Ru–PPh_3 bonds are weakened upon substitution of NCPh with $PBu^n{}_3$. Ramping the collision energy revealed the relative binding strength of three ligands: $PEt_2H > PPh_2H \sim PPh_3$. These experiments were conducted in tandem with ^{31}P NMR studies, which corroborated the ESI-MS results (Figure 1.18). These data also illustrate nicely the difference in typical concentration range between the two techniques, with the NMR studies being conducted at three million times higher concentration than the ESI-MS.

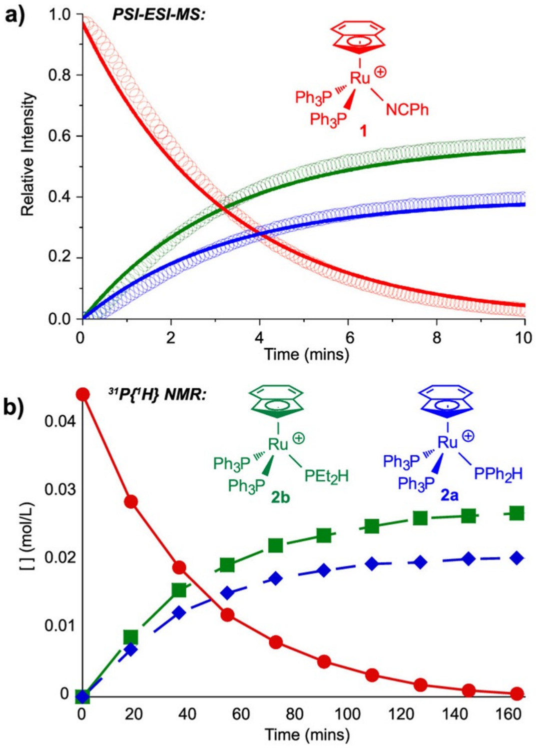

Figure 1.18: a) Competitive reactions of $[Ru(\eta_5\text{-indenyl})(NCPh)(PPh_3)_2]^+$ with a 10:10 mixture of PPh_2H/PEt_2H at 45°C in fluorobenzene, as monitored by PSI-ESI-MS. Circles are normalized experimental data; lines are simulated using parameter estimation with COPASI. (b) 145.85 MHz $^{31}P^1$ H NMR data for the same experiment in 2:1 CH_2Cl_2/C_6D_6 at RT. Adapted from Belli et al.[92]

The capabilities of PSI-ESI-MS can shed light on ‘simple’ reaction systems as well. For example, titanocene has been used as an indicator of oxidation and the presence of O_2. In what was previously known as a straightforward reaction, $Cp_2Ti(IV)X_2$ was reduced to Ti(III) followed by oxidation back to Ti(IV). In acetonitrile the oxidized species is yellow in colour, $[Cp_2Ti(NCMe)_2]^{2+}$. Real-time analysis has revealed that the oxidation is not as simple as it seems. In fact, a variety of oxygen-containing products were generated, and $[Cp_2Ti(NCMe)_2]^{2+}$ was found to be quite reactive toward protic solvents.[93] When the reaction was tested in the presence of water it was found that the oxidation proceeded slowly and required a significant amount of water, making this system non-ideal for detection of trace amounts of water in reactions and gloveboxes alike.

The PSI technique is also capable of handling extremely air- and moisture-sensitive systems, such as olefin polymerization catalysts (Figure 1.19).[94] The reaction shown is that between $[Cp_2ZrMe_2AlMe_2][B(C_6F_5)_4]$ and (a) 100 and (b) 1000 equivalents of hexene, a reaction that results in polymerization of the hexene and a range of decomposition pathways for the catalyst precursor. Note the ability of the technique to provide reaction rates and identification of the various catalyst deactivation products.

Summary and Outlook

PSI-ESI-MS has strong capabilities in reaction monitoring and observation of reaction intermediates under air- and moisture-free conditions. The method has been described as a “breakthrough strategy” in terms of online acquisition of high-quality data.[95] The low pressure system driving solution through a small diameter capillary can lead to obstruction of the flow path, a phenomenon less prominent in high pressure systems. This issue can be problematic at times due to the influence on the resulting kinetic profile, especially in heterogeneous systems which are more prone to clogging. Despite this challenge, the speed, ability to cope with complex mixtures, and extremely high sensitivity of mass spectrometry is superior to several other analytical techniques, and a robust sample delivery system is a critical tool to build and extend its applications.

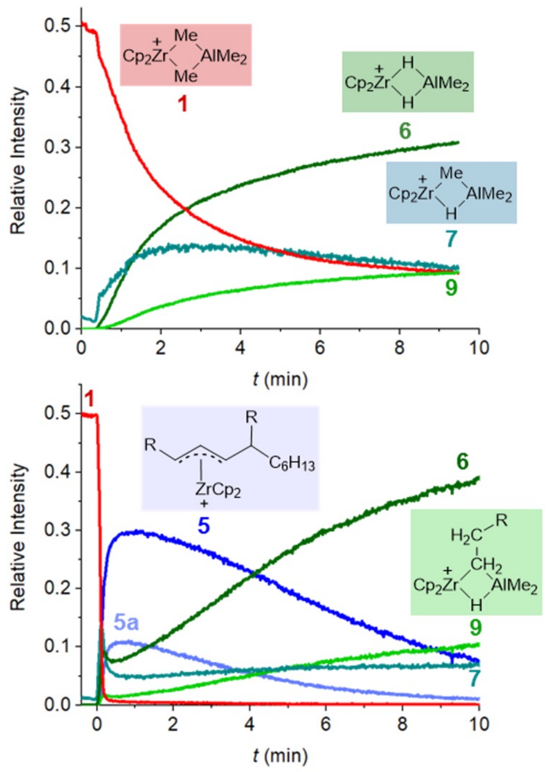

Figure 1.19: Normalized ion intensities vs time for addition of (a) 10 equivalents, and (b) 1000 equivalents of hexene to $[Cp_2ZrMe_2AlMe_2][B(C_6F_5)_4]$ in difluorobenzene solution with $[Zr] = 0.28$ mM; R = n-Bu. Adapted from Joshi et al.[94]

1.4.2 Stopped-flow NMR Reaction Monitoring

Originally developed in the 1970s,[96–98] stopped-flow NMR systems typically mix two reagents in a mixing chamber immediately prior to NMR analysis (Figure 1.20). These systems consist of a shared drive plate pushing two large reagent-containing syringes into the mixing chamber where the reagents react with one another. The reaction solution then continues through the measuring area of the NMR in a specialized NMR probe and into a smaller syringe, when this syringe is full its plunger makes contact with a stopping plate. Electronic sensors then trigger release of the rf pulse to initiate a measurement.

Several innovations to stopped-flow NMR systems have since been reported.[99–103] Most relevant to this dissertation, the Lloyd-Jones group at the University of Ed-

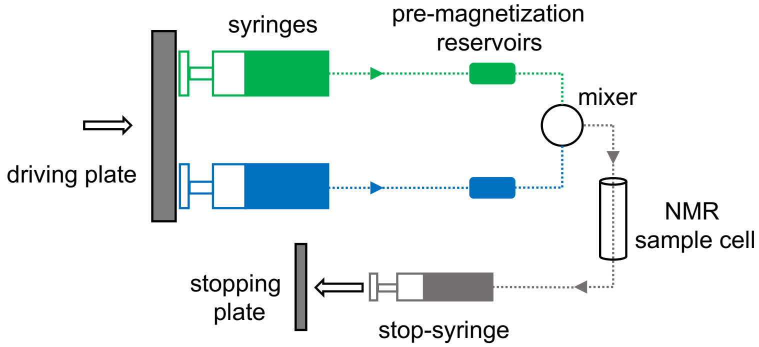

Figure 1.20: Schematic of typical stopped-flow NMR systems requiring a customized NMR probe.

inburgh have developed a three-component variable-ratio stopped-flow NMR system (Figure 1.21).[104] By modifying the system to accommodate three individually-pumped syringes, only a single set of stock solutions is required to do several user-defined variable-ratio experiments. These pump reactants into a flow cell where the NMR analysis is performed. The previous contents of the flow cell is effectively removed to waste by the incoming reaction mixture. After the syringes are finished pumping, a rapid trigger signal (on the order of milliseconds) is sent from the drive unit to initiate the measurement, eliminating the need for a microswitch on a stop syringe. Rather than a specialized NMR probe, this system requires a customized stopped-flow insert designed to fit directly in the existing NMR probe, i.e. shaped like the turbine. The system has thus far been successfully used to study the mechanism of TMSCF$_3$, including trifluoromethylation,[104] difluorocarbene generation,[105] and C–H silylation[106] which will be detailed in Chapter 4.

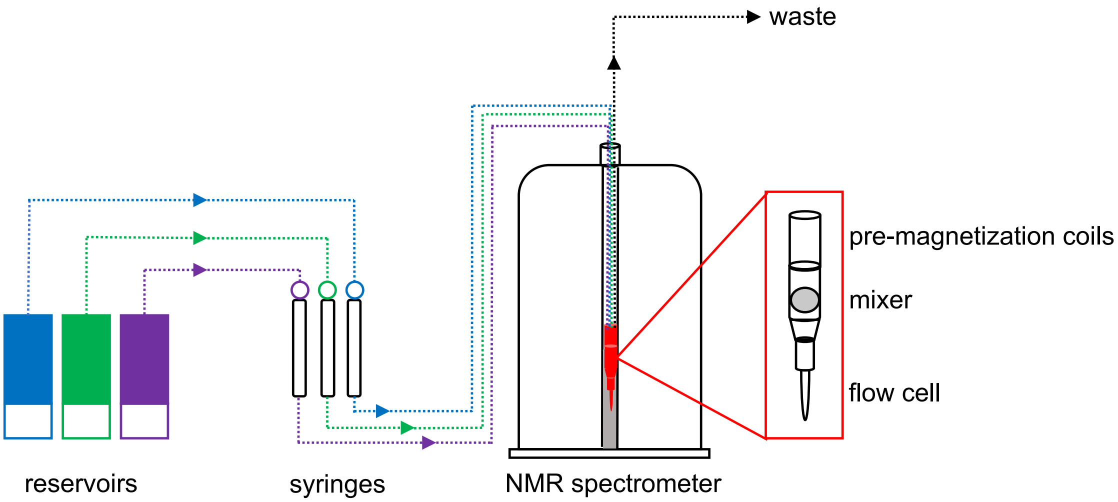

Figure 1.21: Schematic of the stopped-flow NMR system at the University of Edinburgh. Adapted from Johnston et al.[104]

1.5 Objectives

Overall, the main goal is to use ESI-MS, IMS-MS, PSI and NMR spectroscopy to uncover reaction features such as mechanistic information and speciation of intermediates. These analytical techniques will be demonstrated on their own, as well as orthogonally to provide complementary data sets thus further insight into reactivity. Shedding light on these details will ultimately enhance our understanding and lay the groundwork for improving efficiency of future reactions.

Chapter 2

Confounding Contaminants in Mass Spectrometric Reaction Monitoring

Portions of this chapter have been reproduced from G.T. Thomas, L. MacGillivray, N.L. Dean, R.L. Stoddard, L.P.E. Yunker and J.S. McIndoe, *International Journal of Mass Spectrometry*, **2019**, *441*, 14–18, and adapted with permission from Elsevier B.V.

2.1 Preface

Pressurized sample infusion (PSI) had been developed by the McIndoe group in recent years, and efforts were consistently made to improve the methodology. It was noted that the same *m/z* peaks were observed in various reactions. An investigation was undertaken to identify these unknown species, and devise a preventative measure.

All spectra acquisition and data analysis was performed by Gilian Thomas. Flask re-design was done by Prof. J. Scott McIndoe. Preliminary investigations were completed by R. Stoddard, N.L. Dean, and L. MacGillivray. Figure 2.2 was produced by Dr. L. Yunker. The manuscript was written collaboratively by Prof. J. Scott McIndoe and Gilian Thomas.

2.2 Abstract

Reactions carried out in the presence of rubber septa run the risk of additives being leached out by the solvent. Normally, such species are present at low enough levels that they do not interfere with the reaction significantly. However, when studying reactions using sensitive methods such as mass spectrometry, the appearance of even trace amounts of material can confuse dynamic analyses of reactions. A wide variety of additives are present in rubber along with the polymer: antioxidants, dyes, detergent, and vulcanization agents, and these are all especially problematic in negative ion mode. A redesigned Schlenk flask for pressurized sample infusion (PSI) is presented as a means of practically eliminating the presence of contaminants during reaction analyses.

2.3 Introduction

Pressurized sample infusion (PSI)[36,61] is an effective way to analyze chemical reactions in real time using ESI-MS as it allows for monitoring the behaviour of low-intensity catalytic species as they are produced. We (and others) have used PSI to study a wide range of catalytic reactions in both positive[76,78–80,83,88,90,95,107–111] and negative ion mode.[56,112,113] In these experiments, impurities are not uncommon, but are generally present either from the start of the reaction or appear upon addition of a particular reaction component, and do not change significantly in intensity over the course of a reaction.[57] However, we have also observed a number of unexpected/unidentified ions have been observed growing more abundant over the length of an experiment in negative ion mode. The m/z values of these unexpected ions tend to be found in the lower mass region of the spectrum, and can overlap and/or obscure the low-intensity species of interest. Even at low levels, such contaminants can complicate mechanistic analyses because they do not align with the predicted species based on the chemicals present, and because their dynamics can match those expected of decomposition products. Such decomposition products are of interest because they can often suggest ways in which the catalyst is dying, and therefore knowing the source of a particular signal is important. Both low resolution[114] and high resolution[115] mass spectrometry can provide structural information needed to identify unknown species, but avoiding contaminants in the first place is always the best practice.

Previous mass spectrometric research has reported vulcanizing agents and antioxidants leaching into reaction mixtures.[116–119] The incidental contact of solvent to rubber septa results in the leaching of interfering ions into the reaction mixture, and this process is especially efficient when the reaction solvent is heated. Primary and secondary antioxidants are often used to prolong or inhibit the free radical chain mechanism of oxidative decomposition in rubber, plastics, and foods. Primary antioxidants can disrupt autoxidation by neutralizing free radicals active in the propagation step via donation of hydrogen atoms to these free radicals.[120] In phenolic antioxidants this occurs via hydrogen-atom transfer (HAT) when the bond dissociation enthalpy of the O–H bond is low.[121,122] Alternatively, these antioxidants can perform a single electron transfer (SET) to a free radical, and it is likely that both HAT and SET occur in parallel.[121,122] In comparison, secondary antioxidants react directly with the oxidizing agents and are regularly utilized in tandem with primary antioxidants.[123,124] Alkylated phenols have long been known to stabilize polymers and to prevent oxidation of natural rubber after vulcanization.[125–128] In order for a given phenol to act as an effective primary antioxidant, the alcohol group must be in a chemical environment in which the acidic hydrogen of the phenol is readily available for donation, allowing for free radical neutralization. Additionally, the reactivity of the phenoxy radical intermediate must be minimized to prevent decomposition of the antioxidant.[124] In most phenolic antioxidants, these requirements have been satisfied by the introduction of steric bulk in the ortho position relative to the alcohol group, which helps to stabilize the phenoxy radical intermediates and increases the antioxidation potency of the phenols.

Mercaptobenzothiazoles are used to accelerate the vulcanization of rubber,[129] inhibit corrosion,[130] as herbicides, as anti-tumor agents,[131] and are present in food storage containers with septa.[132,133] The sulfur component is able to facilitate cross-linking via various mechanisms,[134] which ultimately hardens the rubber. Rubber septa are widely known to be vulcanized, and as such vulcanizing agents may be observed in reactions where contact has occurred between the solvent and septum.

Herein we identify contaminants originating from vulcanization and antioxidant additives in rubber septa, and we present a simple redesign of the glassware used to monitor reactions at elevated temperature, which prevents these contaminants from entering a reaction.

2.4 Results and Discussion

Natural rubber septa are present in most lab environments, and are often marketed for facile chemical addition to an air-free environment. In this study, VWR natural rubber sleeve stoppers were used to demonstrate the increasing concentration of vulcanizing agents and antioxidants extracted from a rubber septum by hot solvent. As mass spectrometry is an extremely sensitive analytical technique, even low concentrations of these compounds can interfere with analysis.

We identified three unknown species observed in our mass spectra: 4,4'-methylenebis(2,6-di-tert-butylphenol) ($[M–H]^-$ at *m/z* 423, **1**) and 2,2'-methylenebis(4-methyl-6-tert-butylphenol) ($[M–H]^-$ at *m/z* 339, **2**) as antioxidants, and 2-mercaptobenzothiazole ($[M–H]^-$ at *m/z* 165, **3**) as a vulcanizing agent (Figure 2.1), all extracted from natural rubber septa. The growing presence of these compounds was observed using low-resolution mass spectrometry, and their identities were then confirmed with high-resolution accurate mass data (Table 2.1).[115]

Table 2.1: High resolution accurate mass data obtained for 1 (m/z 423), 2 (m/z 339), and 3 (m/z 165) in methanol.

Species	Calculated Exact Mass (Da)	Accurate Mass Data (Da)	ppm	mDa
$[C_{23}H_{31}O_2]^-$	339.232_{41}	339.232_{45}	0.1179	0.04
$[C_7H_4NS_2]^-$	165.978_{52}	165.978_{02}	3.012	-0.5
$[C_{29}H_{43}O_2]^-$	423.326_{31}	423.326_{84}	1.252	0.53

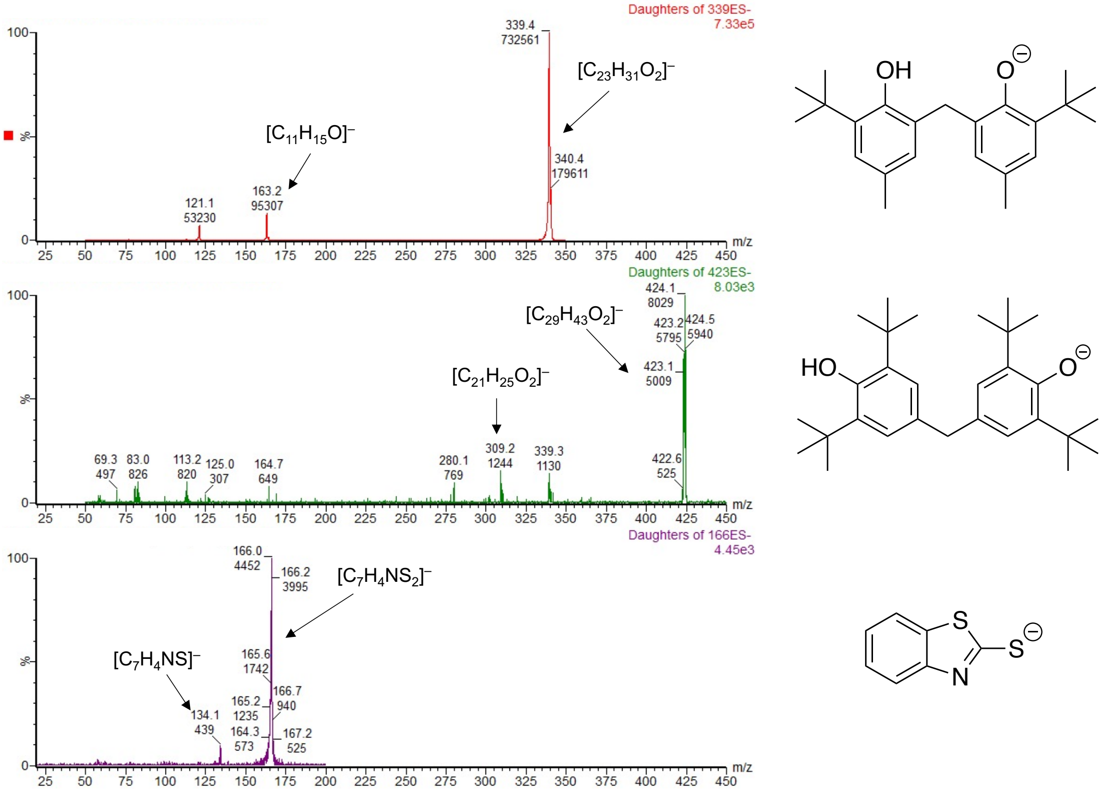

Figure 2.1: Product ion scans of identified antioxidants in acetonitrile, CE=15 V. Top: 2,2'-methylenebis(4-methyl-6-tert-butylphenol) ($[M–H]^-$ at m/z 339, **2**). Middle: 4,4'-methylenebis(2,6-di-tert-butylphenol ($[M–H]^-$ at m/z 423, **1**). Bottom: 2-mercaptobenzothiazole ($[M–H]^-$ at m/z 165, **3**).

The exact mass of m/z 339.23245 provided by the orbitrap mass spectrometer corresponded to only one CHNO ion to within 1 ppm: $C_{23}H_{31}O_2$.[135] As operation was in negative ion mode this species is assumed to be deprotonated, giving the formula

$C_{23}H_{32}O_2$. This formulation includes an acidic proton as well as unsaturation to the tune of eight double bond equivalents (DBE), thus pointed to an aromatic compound (two benzene rings is eight DBE). A phenol derivative was strongly indicated as it would account for high ionization efficiency in negative ion mode. A search revealed **2** (also known as antioxidant 2246) as the most likely candidate. This result guided our assignment of *m/z* 423.32631 as **1**, another structurally related antioxidant.[128,135]

A single result carrying the same isotopic pattern observed in the spectrum was obtained within 1 ppm for the observed *m/z* 165.97802: $C_7H_4NS_2$. As deprotonation was assumed in negative ion mode analysis, the molecular formula was determined to be $C_7H_5NS_2$. This formula also includes an acidic proton, and six degrees of unsaturation. **3** was found to meet these requirements, and is a known vulcanizing agent.[130] Product ion scans of these *m/z* supported our structural assignments, as shown in Figure 2.1.

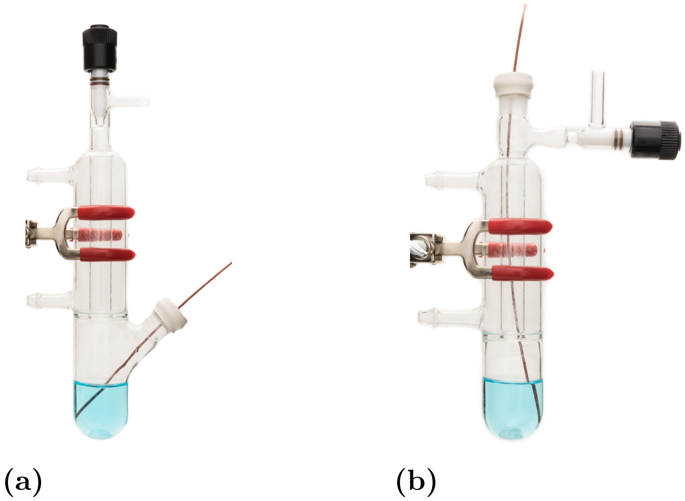
(a) (b)

Figure 2.2: (a) First generation PSI flask; (b) Re-designed second generation PSI flask with ground glass joint above the condenser, positioned adjacent to the gas inlet tap.

The additive compounds we identified were observed throughout various PSI experiments using a first generation PSI flask. This flask was designed with a tap above the condenser to control the inlet of inert gas, and a ground glass joint covered by a septum below the condenser (Figure 2.2a). As the joint was below the condenser, the septum was in close proximity to the reaction mixture and within reach of volatile solvent. The concentration of contaminants is proportional to the temperature of the reaction, however the quantity of each is dependent on the solvent. Dichloromethane was found to extract the highest concentration of **1**, **2** and **3** (Figure 2.3a). In comparison, the concentrations of these additives were significantly lower in acetonitrile (Figure 2.3c), and methanol was found to extract the lowest quantity (Figure 2.3e). Signal intensity for the observed contaminants would likely increase in the presence of a deprotonating agent as ionization would be improved.[136]

In order to prevent **1**, **2** and **3** from entering the reaction vessel, a second generation PSI flask was created. This model is equipped with a rubber septum above the condenser, adjacent to the gas inlet tap, to ensure that volatile solvent cannot make contact with the rubber. The only consequence of this design is the increased length of capillary tubing leading to the mass spectrometer (Figure 2.2b). However, the second generation flask design has been shown to successfully eliminate contamination from rubber septa in all three solvents (Figure 2.3b, 2.3d, 2.3f).

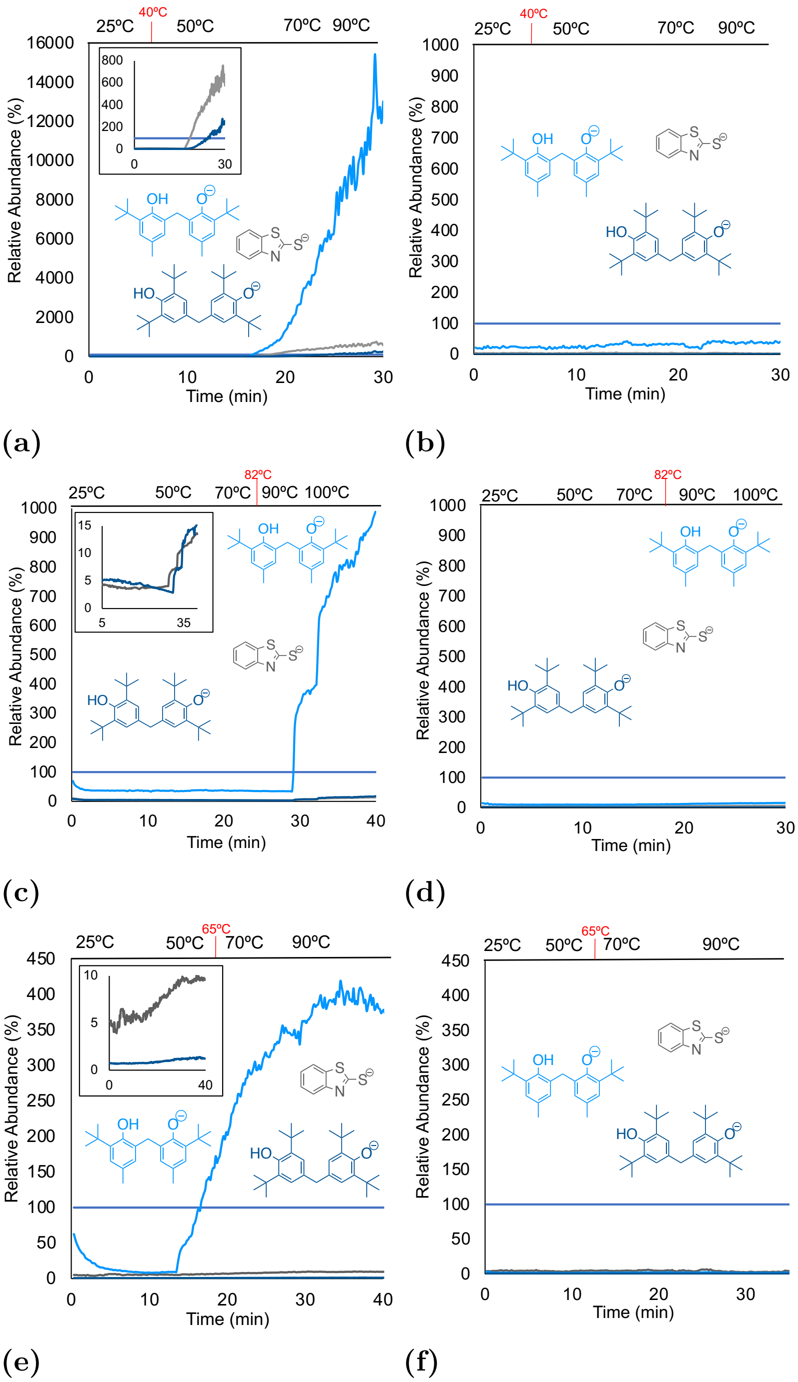

Figure 2.3: Monitoring the relative abundance of **1** (m/z 423), **2** (m/z 339), and **3** (m/z 165) at various temperatures (T reported is bath temperature, so values over the b.p. indicate more vigorous refluxing) over time. Benzoic acid was used as an internal standard and as such is observed at 100% relative abundance. (a) Dichloromethane solvent, septum placement below the condenser; (b) dichloromethane solvent, septum placement above the condenser; (c) acetonitrile solvent, septum placement below the condenser; (d) acetonitrile solvent, septum placement above the condenser; (e) methanol solvent, septum placement below the condenser; (f) methanol solvent, septum placement above the condenser.

2.5 Conclusion

Overall, three frequently observed unknown peaks were identified as 4,4'-methylenebis (2,6-di-tert-butylphenol), 2,2'-methylenebis(4-methyl-6-tert-butylphenol), and 2-mercaptobenzothiazole. As all have a known presence in rubber septa, the PSI flask used to study reactions in real-time was redesigned to prevent these contaminants from entering the reaction. By positioning the septum above the condenser and away from the main reaction vessel, hot solvent no longer has the ability to extract additives from the rubber. This design has proven to eliminate contamination, and results in spectra free of extraneous contributions from species unrelated to the reaction under study.

2.6 Materials and Methods

Reagent grade acetonitrile (Caledon Laboratories, Georgetown, ON, Canada) and methylene chloride (Fisher Chemical, Hampton, NH, USA), and HPLC-grade methanol (Fisher Chemical) solvents were purchased, and used without further purification. Natural rubber septa were purchased from VWR (Radner, PA, USA) (Cat No. 89097-554). Benzoic acid was purchased from Sigma-Aldrich (St. Louis, MO, USA) and dissolved in the solvent being tested (i.e. acetonitrile, methanol, or dichloromethane). All mass spectra were collected on a Waters Acquity Triple Quadrupole Detector (Waters Corporation, Milford, MA, USA) in negative ion mode, with the following electrospray ionization parameters: capillary voltage, 3000 V; cone voltage, 10 V; extraction voltage, 3 V; source temperature, 80°C; desolvation temperature, 210°C; cone gas flow, 100 L/hr; desolvation gas flow, 500 L/hr; collision voltage, 2 V.

Benzoic acid stock solutions (100 µM) were made in each of the three solvents. In each experiment 0.5 mL was injected into 10 mL of solvent, as an internal standard. A

PSI flask (Schlenk flask equipped with a built-in condenser) was equipped with a stir bar and a septum. PEEK tubing was inserted through the septum into the solution on one end with the other end attached to the ESI source of the mass spectrometer. Argon gas was introduced to the PSI flask at 3 psi whereby the positive pressure forced the solution out of the flask through the tubing to the mass spectrometer. The solution was gradually heated in an oil bath for up to 45 min, SRM spectra of each *m/z* value were recorded once per second.

High-resolution accurate mass analyses were then obtained on an LTQ Orbitrap VelosTM instrument (Thermo Scientific, Waltham, MA, USA) using a full scan in negative ion mode (*m/z* 100–1000). ESI-MS was carried out via direct infusion of 500 µL of the sample was facilitated at 30 µL/min in methanol using a syringe pump. The spray voltage was set to 2500 V, the capillary temperature was maintained at 250°C, the sheath gas flow rate was 15, the aux gas was set to 5, and the sweep gas was at 0.

Chapter 3

Step-by-Step Real Time Monitoring of a Catalytic Amination Reaction

Portions of this chapter have been reproduced from G.T. Thomas, E. Janusson, H.S. Zijlstra and J.S. McIndoe, *Chemical Communications*, **2019**, *55*, 11727–11730, and adapted with permission from the Royal Society of Chemistry.

3.1 Preface

The observation of reaction rates for each step in a catalytic cycle aids in diagnosis and improvement of the turnover limiting step, leading to increased efficiency. Using the PSI-ESI-MS method previously described in Section 1.4.1, a known amination reaction was studied online in real-time using MS Multiple Reaction Monitoring (MRM) scans to pinpoint specific species. This effectively reduces the signal-to-noise ratio, and increases sensitivity.

All spectra acquisition and data analysis was done by Gilian Thomas. Early stages of the project were developed by Dr. Eric Janusson and Dr. Harmen Zijlstra. The manuscript was written collaboratively by Gilian Thomas and Prof. J. Scott McIndoe.

3.2 Abstract

The multiple reaction monitoring mode of a triple quadrupole mass spectrometer is used to examine the Buchwald–Hartwig amination reaction at 0.1% catalyst loading in real-time using sequential addition of reagents to probe the individual steps in the cycle. This is a powerful new method for probing reactions under realistic conditions.

3.3 Introduction

One of the most common ways to form C–N bonds is the Buchwald-Hartwig amination.[137–140] This versatile palladium-catalyzed cross-coupling between amines and aryl or vinyl halides is widely used and new applications are reported frequently.[141–150] The reaction mechanism is thought to involve oxidative addition of the aryl halide to Pd(0), coordination of the aniline, deprotonation by base, and reductive elimination of the new C–N bond regenerating the Pd(0) catalyst.[151–153] Improved understanding of the reaction and observation of the intermediates during this reaction will aid the further development of catalysts and ligands, as well as provide a thorough understanding of substrate effects, allowing optimization of every reaction component.

To date the reaction has been studied by a variety of spectroscopic methods, and the catalytic cycle is fairly well established under certain conditions (Scheme 3.1),[153–160] however is not entirely understood due to the complexity of the reaction. For example, use of varying palladium catalysts revealed that the rate limiting step is the reductive elimination,[161] and an alternative study employed other substrates to determine that the rate limiting step is the transmetalation.[162] It has also been proven that the ligand selected has an effect on the overall yield of the reaction, and the same study found that solvent and base selection have an influence.[163]

Electrospray ionization mass spectrometry (ESI-MS) has previously been shown to be a valuable tool in studying catalytic reactions.[5,38] The high sensitivity of the

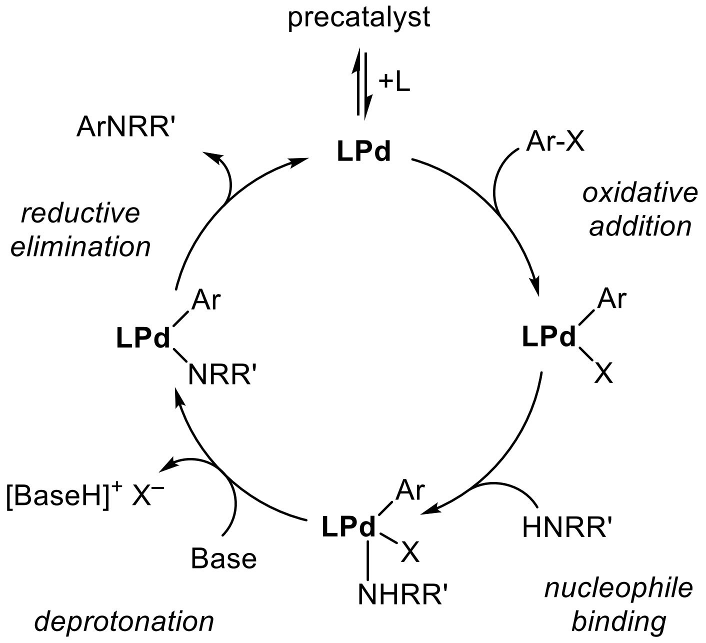

Scheme 3.1: Generally accepted mechanism for catalytic amination as mediated by palladium(0) complexes.

instrument facilitates detection of transient catalytic intermediates which are difficult to detect using other techniques. Additionally, pressurized sample injection (PSI) allows for simple continuous real-time monitoring of air or moisture sensitive reactions.[36]

We have recently investigated the activation of $Pd_2(dba)_3$, a popular catalyst precursor for the Buchwald–Hartwig amination.[112] We now extend this to monitoring the full Buchwald–Hartwig amination cycle using the commercially available, hydrophilic sulfonated Buchwald-type ligand $Na^+[sSPhos]^-$ (Figure 2 inset, from now on represented as L).[164] This ligand is advantageous for mechanistic studies involving ESI-MS, as it carries a charge that it can confer to any complex to which it is bound, enabling straightforward detection during analysis.[165,166] The Buchwald–Hartwig reaction is a challenging target for analysis under normal synthetic conditions, thanks to its high efficiency allowing catalyst loadings as low as 0.1%.[167]

3.4 Results and Discussion

Analysis of a catalytic reaction by PSI-ESI-MS requires all species of interest to be charged, and this can be achieved by using an inherently charged catalyst, by employing a charged substrate, or by modifying the ligand environment to include a charged ligand.[5] The last of these approaches was used here. A triple quadrupole mass spectrometer in multiple reaction monitoring (MRM) mode was used in order to detect the low concentrations of catalytically relevant species present in a typical amination reaction. MRM mode provides increased selectivity: the first quadrupole is fixed on a desired *m/z* value (in the case of the broad Pd-containing isotope patterns analyzed herein, the most abundant isotopomer), it is fragmented using collision-induced dissociation (CID) in the collision cell, while the third quadrupole is fixed on a characteristic product ion. Unlike full scan mode, this technique excludes noise and isobaric species (ions appearing at the same *m/z* that are structurally different), and the signal-to-noise ratio of the analysis is enhanced because the instrument does not spend time scanning the parts of the spectrum of no interest. MRM can be configured such that many different ions can be interrogated on a fast duty cycle, so the effective scan time (time between individual measurements) is of the order of seconds – very fast relative to most spectroscopic methods. In this context ‘‘multiple reactions’’ refers to the unimolecular decomposition reactions (fragmentations) that happen to the selected ions in the collision cell.

MRM has been used extensively to characterize complex biological processes, such as enzymatic catalysis, protein and proteome analysis, and biomarker detection.[168–171] However, very few applications in organometallic reaction chemistry and homogeneous catalysis have been reported.[172] Several reaction monitoring studies have been carried out offline using MRM,[173–176] and several online reaction monitoring studies have been carried out using full scan mode.[21,24,95]

In a simple amination reaction, we were able to monitor the formation of key species present in the proposed cycle using MRM mode on a triple quadrupole mass spectrometer (Figure 3.1). By adding reagents sequentially, high quality mass spectra of each component could be collected. Identity confirmation of each intermediate was done by comparison of their isotope patterns and exact *m*/*z* values compared against calculated values collected on a high resolution hybrid quadrupole-TOF instrument, as well as fragmentation as a result of product ion scans collected on the triple quadrupole instrument. Although each intermediate is observable in the q-TOF instrument, MRM mode on the triple quadrupole instrument holds many advantages over full scan mode as previously mentioned.

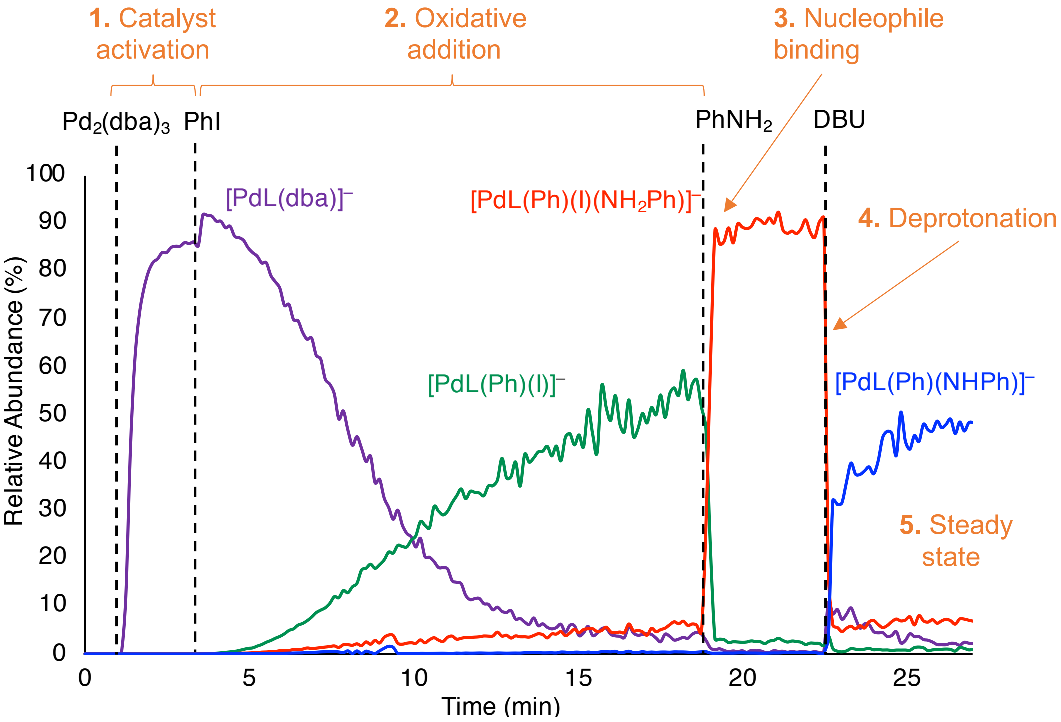

Figure 3.1: Sequential addition of reaction components to probe rates of reaction. This data was obtained using MRM scans on a triple-quadrupole mass spectrometer (see Table 3.1 for parameters).

The first step of the cycle is transforming the catalyst precursor, Pd$_2$(dba)$_3$, into the catalyst resting state. Our previous study of the reaction of Pd$_2$(dba)$_3$ with

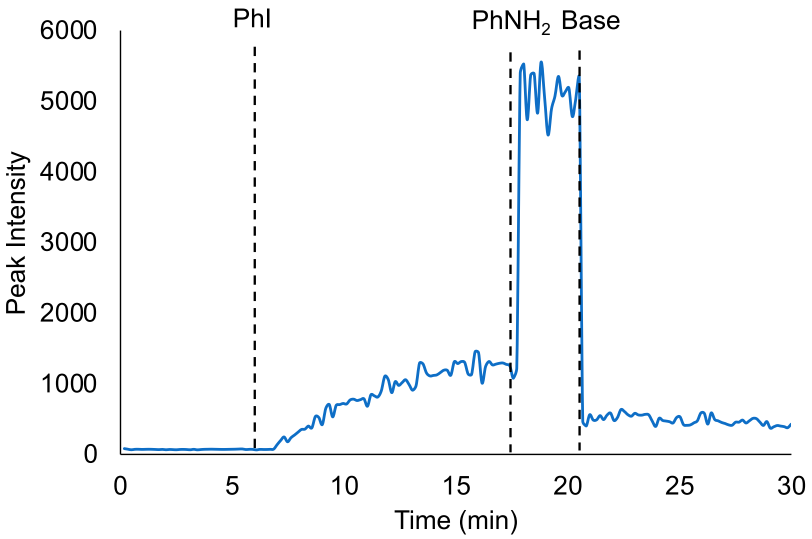

Figure 3.2: Single ion monitoring scan in positive ion mode, monitoring of the addition of PhI to a solution of Pd(SPhos)(dba), resulting in the formation of $[Pd(SPhos)(Ph)]^+$ (m/z 595).

sulfonated phosphines, $[PPh_2(C_6H_4SO_3)]^-$ and L, using ESI-MS and UV/Vis spectroscopy,[177] revealed that the only product of catalyst activation in the L case to be $[Pd(L)(dba)]^-$. This result was replicated here, with a fast and first-order reaction observed with a $t_{1/2} = 0.3$ minutes (Figure 3.1, 1–3 minutes).

Once catalyst activation was complete, an excess of iodobenzene was added, which resulted in the disappearance of $[Pd(L)(dba)]^-$ to be replaced predominantly with $[Pd(L)(Ph)(I)]^-$ (Figure 3.1, 3–19minutes). Small amounts of $[Pd(L)(Ph)(I)(PhNH_2)]^-$ were also observed, due to the trace levels of aniline present in commercial PhI.[178] The differences in rate of $[Pd(L)(dba)]^-$ consumed vs. $[Pd(L)(Ph)(I)]^-$ appearing indicated that some other unobserved intermediate was involved. The most obvious candidate for this was the zwitterionic Pd(L)(Ph), as cationic $[L_2Pd(Ar)]^+$ species are a feature of $L_2Pd(Ar)(X)$ complexes in polar solvents.[86] Accordingly, we performed the experiment with SPhos[179] instead of L (i.e. the same ligand, but unsulfonated), and saw the expected production of $[Pd(SPhos)(Ph)]^+$ in the positive ion mode (Figure 3.2).

The oxidative addition was not particularly rapid, presumably due to the necessity of dba decoordination prior to the reaction taking place.[180] The disappearance of [Pd(L)(dba)]$^-$ produced a linear plot of the natural log of the abundance of [Pd(L)(dba)]$^-$ vs. time for the last 10 minutes of the 15 minutes the reaction took to reach equilibrium (Figure 3.3), and during this period $t_{1/2}$ =1.3 minutes.

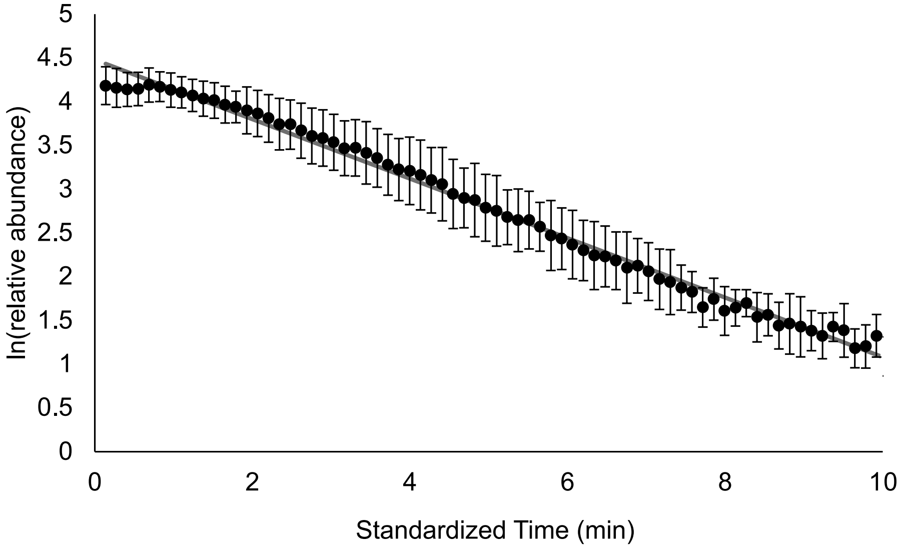

Figure 3.3: First order kinetic plot of ln(relative abundance) vs. standardized time, where relative abundance refers to the [Pd(sSPhos)(dba)]$^-$ species (n=3). Time has been standardized such that t=0 represents addition of $Pd_2(dba)_3$. Kinetic plots for [Pd(L)(Ph)(I)]$^-$ and [Pd(L)(Ph)(I)(NH_2Ph)]$^-$ were constructed in the same fashion

Addition of aniline to the reaction mixture caused immediate disappearance of the signal for [Pd(L)(Ph)(I)]$^-$, to be replaced by [Pd(L)(Ph)(I)(PhNH_2)]$^-$ (Figure 3.1, 19 minutes). This reaction was faster than the time resolution of the PSI-ESI-MS experiment, which takes approximately 20 seconds for the solution to move from the reaction flask to the mass spectrometer.[61] As such, all we can say is that $t_{1/2}$ <20 s. In the positive ion mode (L = SPhos), we did not see the aniline coordinate to the cationic [PdL(Ph)]$^+$, but we did see a sharp increase in the amount of [PdL(Ph)]$^+$, suggesting that the aniline does not strongly bind to the cation but does facilitate the displacement of the iodide ligand.

Deprotonation of the bound aniline was just as fast as association of the aniline to the palladium in the previous step, i.e. a $t_{1/2}$ of <20 seconds (Figure 3.1, 22.5 minutes). The product was $[PdL(Ph)(NHPh)]^-$, i.e. the deprotonation was concomitant with iodide loss. Note that the immediate product of deprotonation of $[PdL(Ph)(I)(NH_2Ph)]^-$ would be $[PdL(Ph)(I)(NHPh)]^{2-}$, however this species was not observed.

Selection of DBU as the base in this reaction prevents formation of NaI species which have been shown to have an inhibitory effect on the reaction.[163,181] Additionally, performing the reaction in a stepwise fashion rather than 'one-pot', prevents observation of base-bound intermediates previously reported, whereby the resting state was determined to be a DBU-bound species after the oxidative addition.[182] Thus the stepwise catalytic cycle has an alternate steady state, discernible in real-time by mass spectrometry.

After addition of base, the amount of $[PdL(Ph)(NHPh)]^-$ did not change significantly in the following 30 minutes or so (Figure 3.1, first few minutes of this process only shown from 23 minutes). A small amount of $[Pd(L)(dba)]^-$ was regenerated after addition of base, suggesting some turnover of the reaction was occurring, though $[PdL(Ph)(NHPh)]^-$ was the dominant catalytically-relevant species and is therefore assigned as the catalyst resting state. Because reductive elimination is a unimolecular decomposition, the transformation could be simulated in the gas phase using collision-induced dissociation (CID).[165] This reaction has the benefit of being able to be performed in isolation from any other solution components, and is therefore uncomplicated by further reactivity. Collisions with argon gas resulted exclusively in reductive elimination of Ph_2NH, with no ligand dissociation observed at all (Figure 3.4).

Using reaction calorimetry, this step was previously established to be rate-limiting in triarylamine formation via C–N coupling due to the low nucleophilicity of diarylamines.[183] However, it was found that the catalytic cycle is in a steady state at

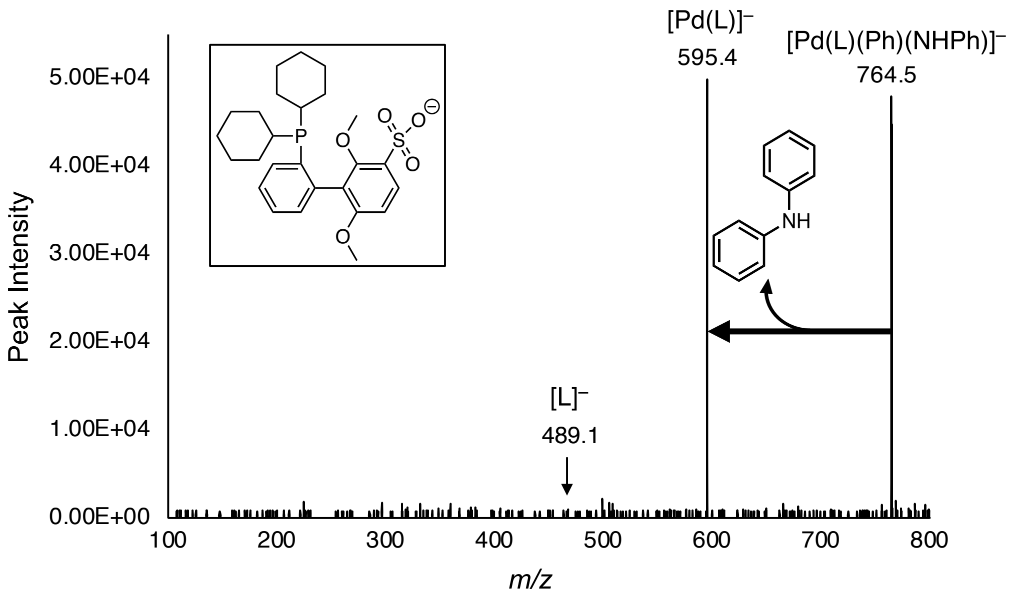

Figure 3.4: Product ion mass spectrum of $[Pd(L)(Ph)(NHPh)]^-$ obtained on a triple quadrupole mass spectrometer. Energetic gas-phase collisions between $[Pd(L)(Ph)(NHPh)]^-$ and argon atoms (CE = 5 V) results in the exclusive formation of $[Pd(L)]^-$ via loss of reductively eliminated $HNPh_2$. Left inset: Structure of $[L]^-$ ($[sSPhos]^-$).

$[Pd(L)(Ph)(NHPh)]^-$ in the formation of diarylamine due to the stepwise addition, as mentioned in the previous section.

Real-time analysis of the Buchwald–Hartwig amination reaction using a triple quadrupole ESI mass spectrometer in multiple reaction monitoring mode revealed rate information on each individual step of the cycle. These data can be summarized in a single set of traces (Figure 3.1), and as a catalytic cycle (Scheme 3.2)[184] whereby the weight of the arrows indicates the relative magnitude of the (pseudo) first order rate constant of each elementary step in the cycle.

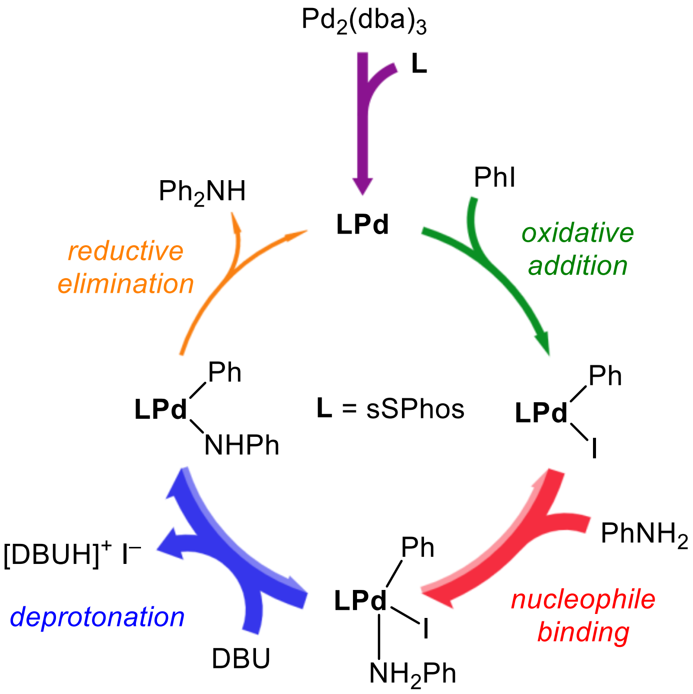

Scheme 3.2: Catalytic cycle with arrows weighted by relative rate constants of each reaction.[184]

3.5 Conclusion

Overall, online reaction monitoring using pressurized sample infusion electrospray ionization mass spectrometry (PSI-ESI-MS) is a viable and powerful method of catalytic mechanism analysis. This is the first reported instance of using multiple reaction monitoring (MRM) scans to observe and quantify catalytically relevant species in real-time. Relative rates of reaction were elucidated, and it was found that the resting state is the $[Pd(L)(Ph)(NHPh)]^-$ species in the formation of diphenylamine via coupling iodobenzene and aniline.

3.6 Materials and Methods

Tris(dibenzylideneacetone)dipalladium(0) ($Pd_2(dba)_3$), sodium 2 -dicyclohexylphosphino-2,6-dimethoxy-1,1 -biphenyl-3-sulfonate hydrate (sSPhos), aniline (99%), iodobenzene (98%), 1,8-diazabicyclo[5.4.0]undec-7-ene (DBU) (98%), and HPLC grade methanol were purchased from Sigma-Aldrich and used as is unless specified otherwise. UHP200 Argon and HP300 4.8 Nitrogen were purchased from Airgas (Calgary, Canada) and used without further purification.

All reagent stock solutions were prepared under an inert nitrogen atmosphere in a Schlenk flask or in a glovebox. $Pd_2(dba)_3$ stock solution was prepared using 0.0045 g $Pd_2(dba)_3$ dissolved in 4.0 mL tetrahydrofuran (dried/refluxed over CaH_2 and distilled under N_2) (1.2 mM Pd). sSPhos (sodium 2-dicyclohexylphosphino-2',6'-dimethoxybiphenyl-3'-sulfonate) stock was prepared by dissolving 0.0045 g of the salt in 4.0 mL HPLC-grade methanol previously dried over CaH_2 (2.1 mM). In a typical reaction, 20.0 mL of HPLC-grade methanol previously dried/refluxed over CaH_2 and freshly distilled under N_2, was transferred to a custom Schlenk flask fitted with a condenser,[68] sparged with nitrogen for 15 minutes, and connected to the mass spectrometer via PEEK tubing passed through a rubber septum. Heating was effected with an IKA C-MAG HS 7 stirring hotplate equipped with an ETS-D5 thermocouple and oil bath. The thermocouple was set to heat the oil bath to 80°C. All reagent stock solutions were prepared under an inert nitrogen atmosphere in a glovebox. An aliquot of sSPhos was injected into the flask, followed by $Pd_2(dba)_3$ to initiate the reaction. Iodobenzene was purified by washing 3 times with 10% HCl, followed by a freeze-pump-thaw cycle. The remaining reagents were freeze-pump-thawed, and added stepwise via syringe.[68]

All electrospray ionization mass spectra were recorded using a Waters Acquity Triple Quadrupole Detector equipped with a Z-Spray electrospray ionization source. The capillary voltage was held at 3.0 kV, cone voltage at 10.0 V, and extraction cone at 3.0 V. The MS cone voltage was optimized to eliminate in-source fragmentation of the catalyst. The desolvation gas flow rate was 500 L/hr, cone gas flow rate 100 L/hr, source temperature 80°C, desolvation temperature 210°C. The RF lens was set to an optimal voltage of 0.3 V. For full scan experiments, scan time was set to 10 s, with an inter-scan time of 0.1 s and a range of *m/z* 400-1000. Product ion scans of each intermediate were completed on the triple quadrupole instrument to optimize collision energy for each species such that the fragment ion was observed at its highest possible abundance, with the precursor ion simultaneously observed at a much lower abundance.

These optimized collision energies were then carried through to the MRM experiments, and these were performed with a collision energy between 5-35 V (species dependent) with an argon collision gas flow rate of 0.1 mL/hr. The full MRM parameter list is below in Table 3.1.

Table 3.1: MRM scan specifications for each intermediate.

Species	Precursor *m/z*	Product *m/z*	Product *m/z* Identity	Dwell Time	Collision Energy (V)
$[\mathrm{sSPhos}]^-$	489	375.4		0.2	35
$[\mathrm{Pd(L)(NHPh)(Ph)}]^-$	764.5	595.1	$[\mathrm{Pd(L)}]^-$	1.5	5
$[\mathrm{Pd(L)(Ph)(I)}]^-$	799	127	$[\mathrm{I}]^-$	1.5	20
$[\mathrm{Pd(L)(dba)}]^-$	829	595.3	$[\mathrm{Pd(L)}]^-$	1.5	25
$[\mathrm{Pd(L)(NH_2Ph)(Ph)(I)}]^-$	892	799.2	$[\mathrm{Pd(L)(Ph)(I)}]^-$	1.5	7

Chapter 4

Trimethylsilylation of Aromatic C–H Bonds Facilitated by $TMSCF_3$

Portions of this chapter have been reproduced from A. García-Domínguez, P.H. Helou De Oliveira, G.T. Thomas, A.R. Sugranyes and G.C. Lloyd-Jones, "Mechanism of Anion-Catalyzed C–H Silylation Using $TMSCF_3$: Kinetically-Controlled CF_3-Anionoid Partitioning As a Key Parameter", *ACS Catalysis*, **2021**, *11*, 3017–3025, and adapted with permission from the American Chemical Society.

4.1 Preface

Gilian Thomas completed all initial investigations and established the reaction conditions for the project at the University of Edinburgh. The project was supervised by A. García-Domínguez and Prof. G.C. Lloyd-Jones, and supplementary experimentation for the manuscript was conducted by P.H. Helou De Oliveira and A.R. Sugranyes. The manuscript was written collaboratively by A. García-Domínguez and Prof. G.C. Lloyd-Jones. All data presented in this chapter is original.

4.2 Abstract

A mechanistic investigation of Me_3SiCF_3 ($TMSCF_3$) with $[Ph_3SiF_2][Bu_4N]$ (TBAT) to achieve C–H silylation was undertaken using *in situ* and stopped-flow ^{19}F-NMR spectroscopy. 1,3-difluorobenzene was the primary substrate used to analyze the production of $ArSiMe_3$ and Me_3SiF. Using these techniques it was discovered that a CF_3-anionoid is the active intermediate during the reaction. $[(CF_3)_2SiMe_3]^-$ liberates the CF_3 reversibly, which then facilitates arene deprotonation to produce $ArSiMe_3$ along with CF_3H. This primary process is competing against F-anion transfer to $TMSCF_3$, resulting in CF_2 and perfluoroalkenes which can then inhibit catalysis.

4.3 Introduction

Arylsilanes are key intermediates in halogenation,[185,186] oxidation,[187,188] and Hiyama coupling reactions,[189,190] and can lead to biologically active compounds.[191] The traditional assembly method has a limited substrate scope as the reagents involved are highly nucleophilic or basic. Other methods have since emerged;[192–198] however a transition-metal-free, more direct procedure is desired. In 2017 Kondo[191] reported the use of trifluoromethyltrimethylsilane ($TMSCF_3$, Ruppert-Prakash reagent) and CsF as a fluoride source to generate a base *in situ* and achieve silylation in reasonable yields with good functional group tolerance.

The mechanism proposed by Kondo (Figure 4.1) involves the combination of $TMSCF_3$ and catalytic CsF to generate $[CF_3]^-$. This carbanion is capable of deprotonating acidic arene sites, which then acquires $SiMe_3$ to generate the Ar–TMS product via a second equivalent of $TMSCF_3$. This step also serves to regenerate the $[CF_3]^-$ species, initiating another turnover.

$TMSCF_3$ has mainly been involved in producing fluorine-containing molecules, and is receiving increasing amounts of attention due to its availability, stability, and

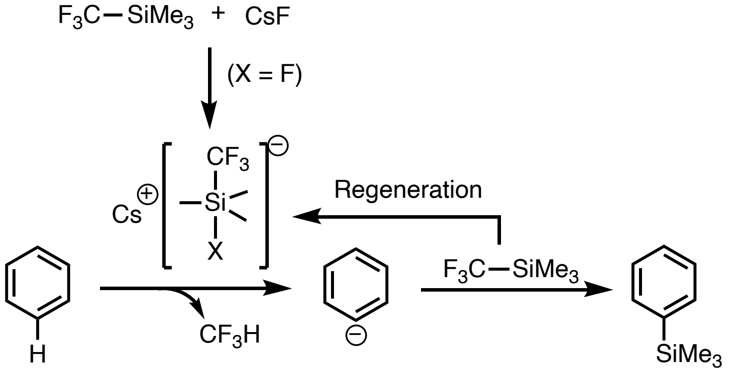

Figure 4.1: Mechanism proposed by Kondo et al.[191] for the addition of a trimethylsilyl group to an arene.

low cost. The Lloyd-Jones group recently studied the mechanism of $TMSCF_3$ in the presence of a catalytic amount of $[Ph_3SiF_2][Bu_4N]$ (TBAT) on both carbonyls[104] and alkenes,[105] producing trifluoromethylated ketones/aldehydes and difluorocyclopropanes, respectively (Figure 4.2).

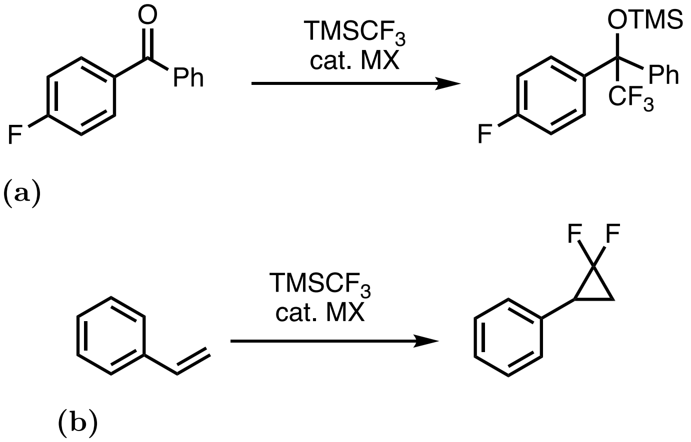

Figure 4.2: Anion-catalyzed reactions with $TMSCF_3$ with a) carbonyls,[104,199,200] and b) alkenes.[105,201–205]

TBAT is a well-known fluoride source commonly used in place of tetrabutylammonium fluoride (TBAF) due to its anhydrous nature, leading to increased experimental reproducibility. The combination of $TMSCF_3$ and TBAT in solution results in $[(CF_3)_2SiMe_3]^-$, $[CF_3]^-$, and $TMSCF_3$ generated in equilibrium (Figure 4.3), and the reaction conditions change this equilibrium such that it can be a source of either CF_2 or CF_3.

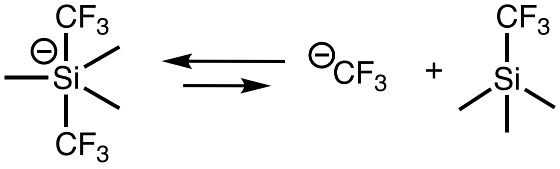

Figure 4.3: Equilibrium between $[(CF_3)_2SiMe_3]^-$, $[CF_3]^-$, and $TMSCF_3$.[104,105,206,207]

Extending from alkenes and carbonyls, this research set out to shed light on the mechanism of $TMSCF_3$ and catalytic TBAT on weak C–H acids, namely 1,3-difluorobenzenes. With a more complete understanding of the mechanism, the conditions can then be tailored to enhance product generation.

4.4 Results and Discussion

The heterogeneous reaction conditions previously established by Kondo were first explored,[191] employing CsF as a fluoride source in dimethoxyethane (DME) at 0°C. These conditions were compared to an alternative fluoride source as well as solvent and temperature (Figure 4.4b). Replacing CsF with TBAT increased generation of product, however the system remained heterogeneous in DME. Changing the solvent from DME to tetrahydrofuran (THF) resulted in a homogeneous reaction solution suitable for monitoring *in situ* by ^{19}F-NMR, and created an environment similar to other previously reported systems.[104,105] Comparing [TBAT] at RT, 5% TBAT generated more product than 2.5% and 1.25%, however 2% was selected for kinetic monitoring experiments.

Initial kinetic monitoring experiments revealed the fast speed of the reaction (Figure 4.5), resulting in a data gap for the first ~80 seconds of the reaction when conducting manual assembly ^{19}F-NMR monitoring (see Section 4.6 for more information).

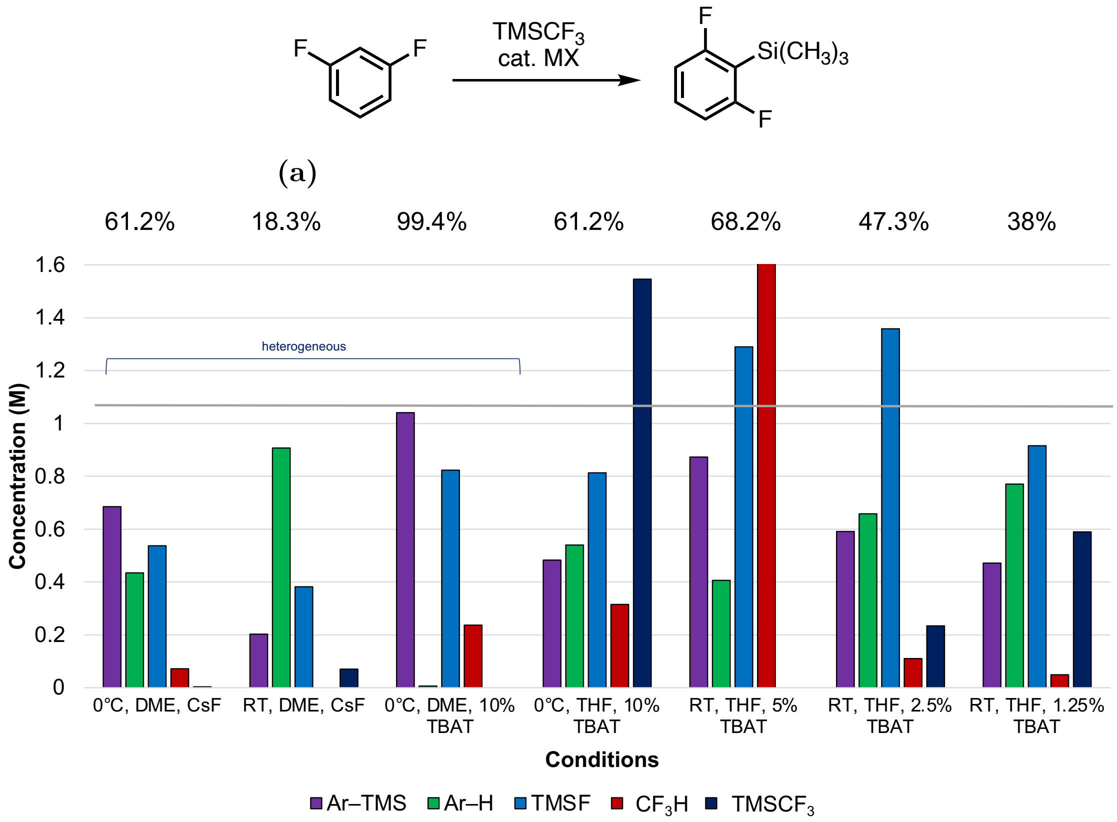

(a)

(b)

Figure 4.4: a) Generic anion-catalyzed reaction of TMSCF$_3$ with a weak C–H acid (Ar–H) to produce Ar–TMS. b) Comparison of reaction conditions for (a). The horizontal grey line represents the highest potential concentration of product. Percent yield of each reaction is displayed above.

The reaction produced CF$_3$H proportionally to the Ar–TMS, however a higher concentration of CF$_3$H was a result of trace amounts of water. The reaction stalled at ~500 seconds, before all of the TMSF$_3$ was consumed. Despite the stall in product generation, the [TMSCF$_3$] continued to decrease albeit at a slower rate. Based on previous research, this decline is attributed to irreversible production of TMSF, and perfluorocarbanion $[C_{11}F_{23}]^-$ from CF$_2$, TMSCF$_3$, and catalytic $[CF_3]^-$.[105]

Because the TMSCF$_3$ was not fully consumed before the reaction stalled, various ratios of TMSCF$_3$ and Ar–H were explored. It was hypothesized that a lower [TMSCF$_3$] would drive the active CF$_3$-anionoid primarily into the productive pathway, rather than towards inactive species. A ratio of 0.5:1 TMSCF$_3$/Ar–H signifi-

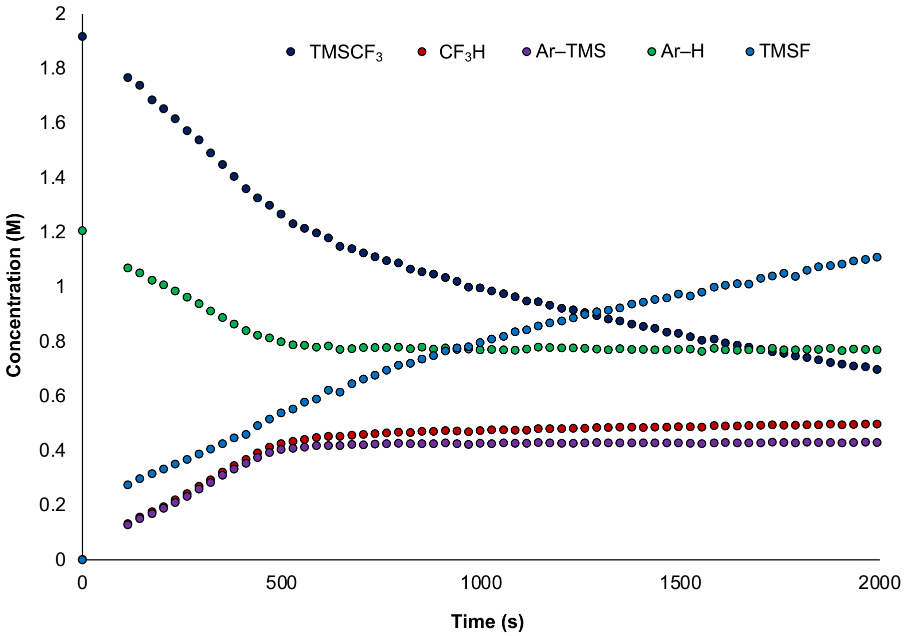

Figure 4.5: Initial ^{19}F-NMR kinetic monitoring of the TBAT-catalyzed reaction between Ar–H and $TMSCF_3$. Conditions: 1.2 M Ar–H, 2.5 M $TMSCF_3$, 0.0024 M TBAT (2%), THF, RT.

cantly sped up the reaction, making the initial kinetics unobservable (Figure 4.6a). With our original goal in mind, this increased speed of the reaction hampered our progress as it is impossible to tell if the reaction stalled prior to $TMSCF_3$ consumption. In comparison, 1:1 $TMSCF_3$ was slower and generated slightly less Ar–TMS (Figure 4.6b). Additionally, all $TMSCF_3$ was consumed within the time-frame of the experiment, although significantly later than the reaction stalled. Overall, 2:1 $TMSCF_3$/Ar–H had the slowest initial rate. This indicates that $TMSCF_3$ has an inhibitory effect on production of Ar–TMS, which could mean that the active intermediate is the $[CF_3]^-$ anion, rather than the $[(CF_3)_2SiMe_3]^-$ siliconate based on the previously established equilibrium (Figure 4.3).

During these initial experiments the production of gaseous CF_3H was much faster than the time allowed for complete dissolution. The volume of CF_3H inside the NMR tube was so high it caused the septum to be forcefully removed from the tube. If the lid was to land inside the NMR spectrometer it would cause significant issues for the

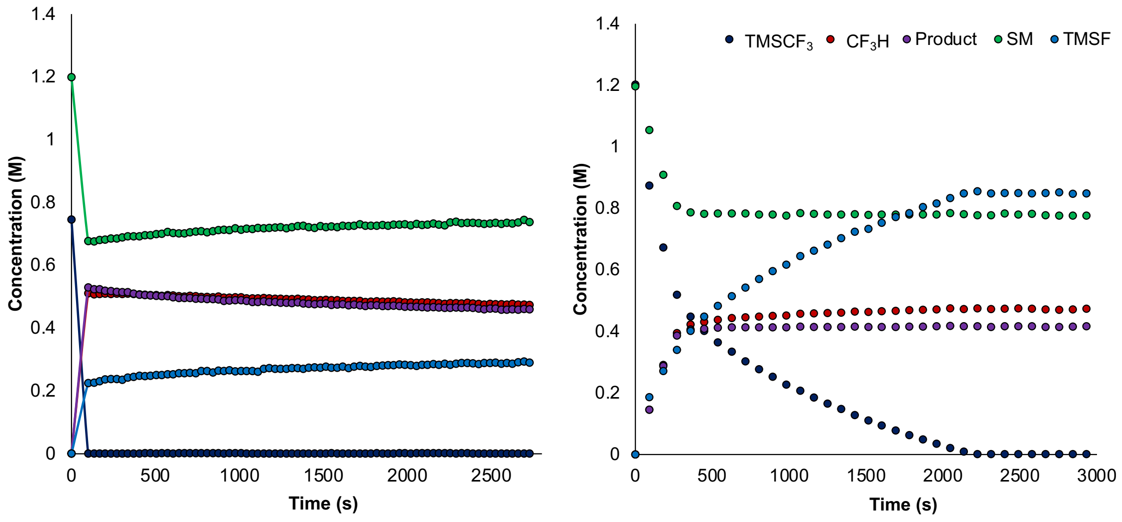

(a) **(b)**

Figure 4.6: ^{19}F-NMR reaction kinetics with 2% [Ph_3SiF_2][Bu_4N] and (a) 0.5:1 $TMSCF_3$/Ar–H (lines present to guide the eye only); b) 1:1 $TMSCF_3$/Ar–H.

instrument, thus lower concentrations were investigated. Varying amounts of TBAT were tested at 1:1 $TMSCF_3$/Ar–H (Figure 4.7). Although 2% TBAT was optimal in higher concentration reactions, it yielded less Ar–TMS than 5% and 10% TBAT at lower concentrations, and did not consume all $TMSCF_3$ in the allotted time. From these results 5% TBAT was selected to move forward in subsequent studies.

It was additionally noted that the concentration of CF_3H produced was far higher than the concentration of Ar–TMS when the reaction was done at lower concentrations of $TMSCF_3$ and Ar–H. Based on the proposed mechanism these species should be produced 1:1, however even small amounts of water in the system can cause the [CF_3H] to increase beyond this ratio. The small amount of water holds a more prominent role at lower reagent concentrations. When performed in *d$_8$*-THF only CF_3H was produced rather than CF_3D, confirming that all CF_3H production was due to arene deprotonation and adventitious water, rather than deprotonated solvent.[104] Additionally, conducting the reaction the presence of molecular sieves did not significantly improve the concentration of fluoroform. It was later revealed that the 'house'-nitrogen supply was noticeably wet, and was not rectified during my tenure

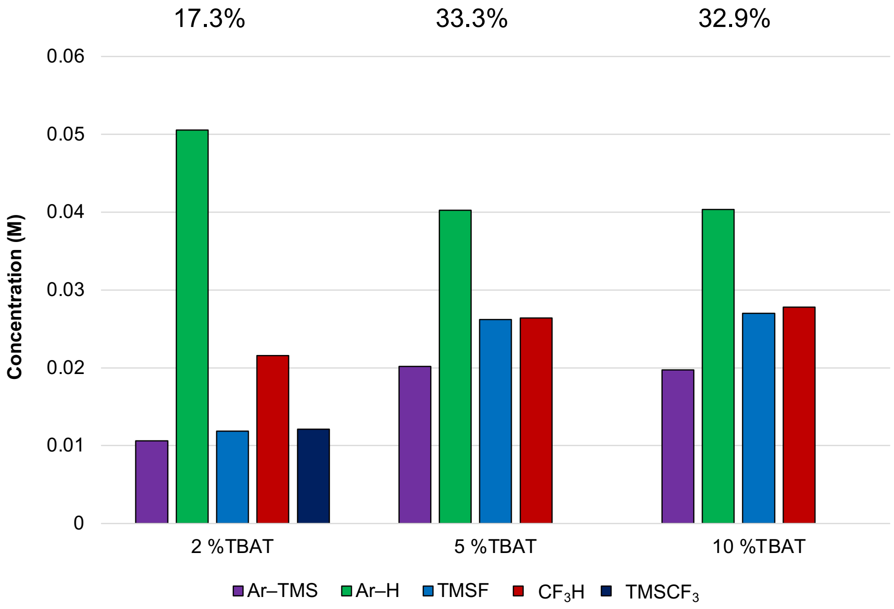

Figure 4.7: Influence of % TBAT at lower concentration starting conditions. Percent yield for each reaction is displayed above. Conditions: 0.06 M Ar–H, 0.06 M $TMSCF_3$, THF, RT.

at the University of Edinburgh.

We then moved on to investigating the effect of substrate para-substitution, whereby 1,3-difluorobenzene was exchanged for 1,3-difluoro-5-methoxybenzene and 1,3,5-trifluorobenzene ∼ 1:1 with $TMSCF_3$. In the case of 1,3-difluoro-5-methoxybenzene, the reaction stalled early on, and had less conversion of starting material to product (Figure 4.8). One could imagine that the protons in the 4- and 6-position on the aromatic ring may be acidic enough to participate in the reaction with $TMSCF_3$, though these products were not observed. Only a single TMS-containing product was present holding the TMS at the 2-position.

The reaction with 1,3,5-trifluorobenzene proceeded much faster, stalling in under 110 seconds making initial kinetic profile unobservable (Figure 4.9a). The overall conversion of starting material to product was approximately the same as 1,3-difluorobenzene, however three different products were generated. The addition of a fluoride in the 5-position creates two additional acidic protons on the aromatic ring at

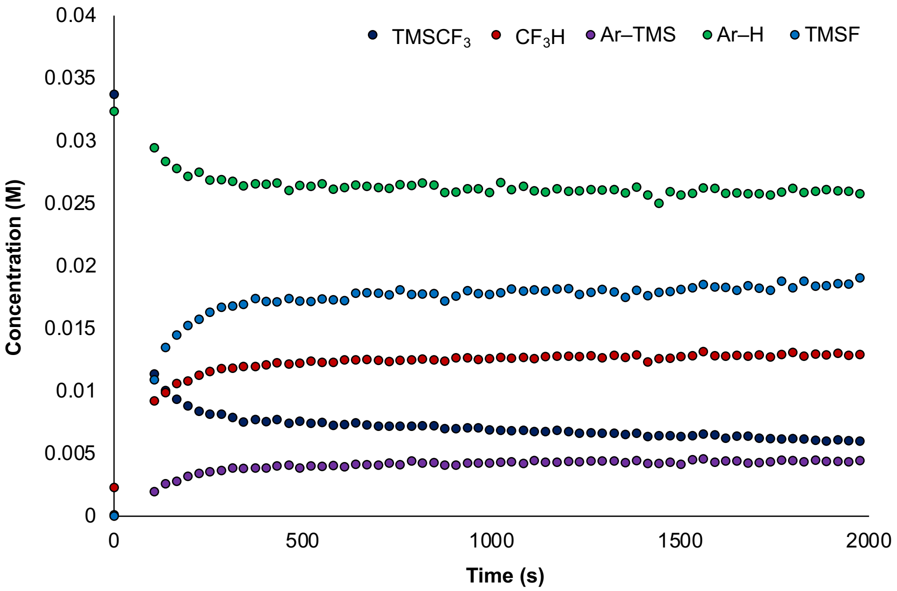

Figure 4.8: Kinetic profile of the reaction between TMSCF$_3$ and 1,3-difluoro-5-methoxybenzene. Conditions: 0.032 M Ar–H, 0.033 M TMSCF$_3$, 0.003 M TBAT (5%), THF, RT.

the 4- and 6-position. The acidity of these protons allows them to participate in the reaction with TMSCF$_3$, leading to production of ArTMS, Ar(TMS)$_2$, and Ar(TMS)$_3$. Each product was quantified separately and it was found that the Ar–TMS product was most prominent (Figure 4.9b). The conversion of substrate to product for 1,3,5-trifluorobenzene was notably higher than 1,3-difluorobenzene, and TMSF production was significantly lower. This means that substrates with highly acidic protons are more efficient, as less TMSCF$_3$ is funneled into the non-productive pathway.

To probe the reaction stall, several variations of reagent addition were tested after the [Ar–TMS] appeared to remain constant. As TBAT is the primary fluoride source and is only present in catalytic amounts, it was thought that further addition of TBAT after the reaction stalled may re-initiate turnover. This was tested in two ways: after depletion of TMSCF$_3$, and prior to depletion of TMSCF$_3$ present in the reaction. Unfortunately, neither scenario resulted in re-initiation of turnover. Further addition of TMSCF$_3$, as well as Ar–H also did not re-initiate turnover. However, a second

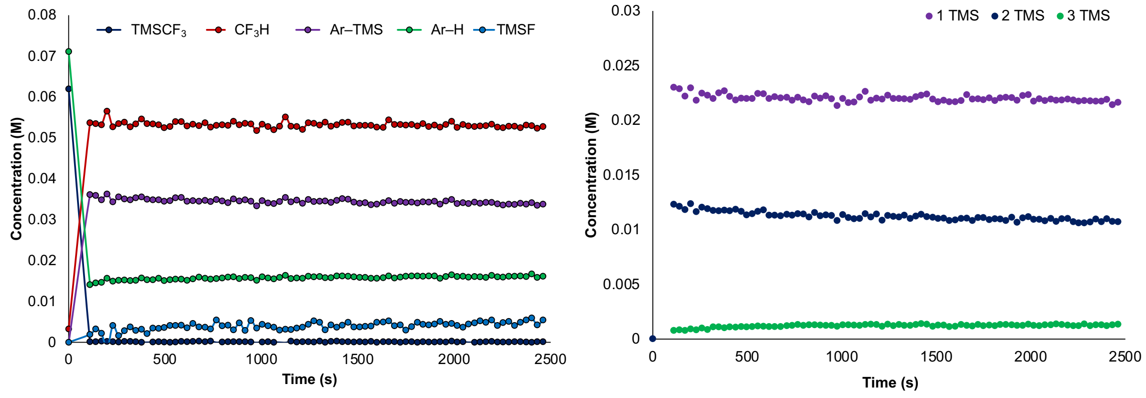

(a) **(b)**

Figure 4.9: a) Kinetic profile of the reaction between TMSCF$_3$ and 1,3,5-trifluorobenzene, Ar–TMS represents the sum of ArTMS, Ar(TMS)$_2$, and Ar(TMS)$_3$. b) Kinetic profile of ArTMS, Ar(TMS)$_2$, and Ar(TMS)$_3$ individually. Conditions: 0.07 M Ar–H, 0.062 M TMSCF$_3$, 0.003 M TBAT (5%), THF, RT.

addition of *both* TBAT and TMSCF$_3$ was successful in generating more Ar–TMS after the reaction stalled (Figure 4.10).

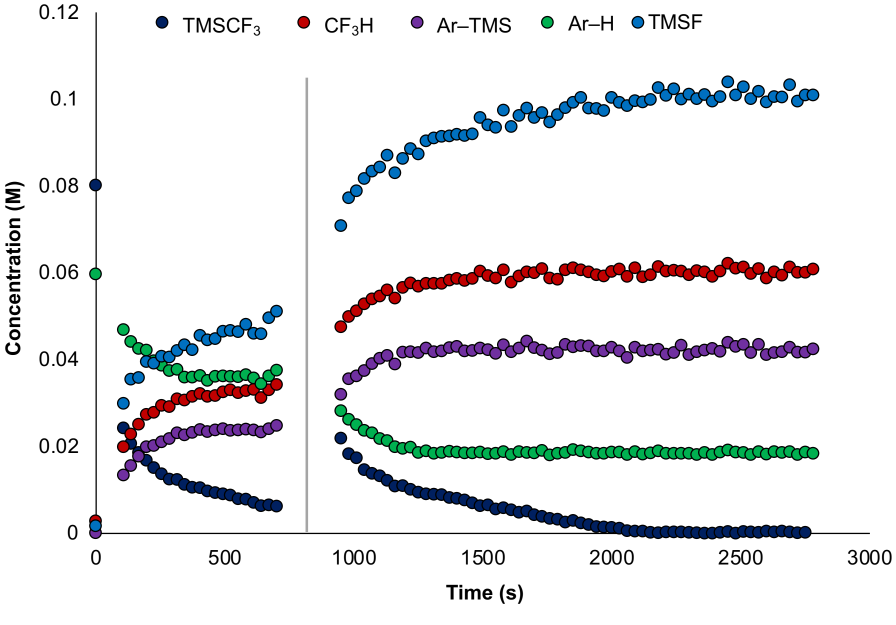

Figure 4.10: ^{19}F-NMR analysis with further addition of TBAT and TMSCF$_3$ (indicated by the grey line). Conditions: 0.06 M Ar–H, 0.08 M TMSCF$_3$, 5% TBAT, THF, RT.

The inhibition is caused by depletion of active anionoid [CF$_3$]$^-$, as it can be sequestered in species such as [C$_{11}$F$_{23}$]$^-$ via CF$_2$.[105] This process is irreversible as elimination of fluoride from this perfluorocarbanion is strongly disfavoured due to instability of the highly strained resulting perfluoroalkene.[105] In an attempt to trap the CF_2, triphenylphosphine (PPh_3) was tested as a nucleophile. PPh_3 has been shown to form an ylide with CF_2 and exist in equilibrium.[208] Addition of PPh_3 in offline experiments showed that 30% PPh_3 addition improved the production of Ar–TMS compared to 0%, 70%, and 150% (Figure 4.11). Ultimately other avenues were pursued for CF_2 trapping.[106]

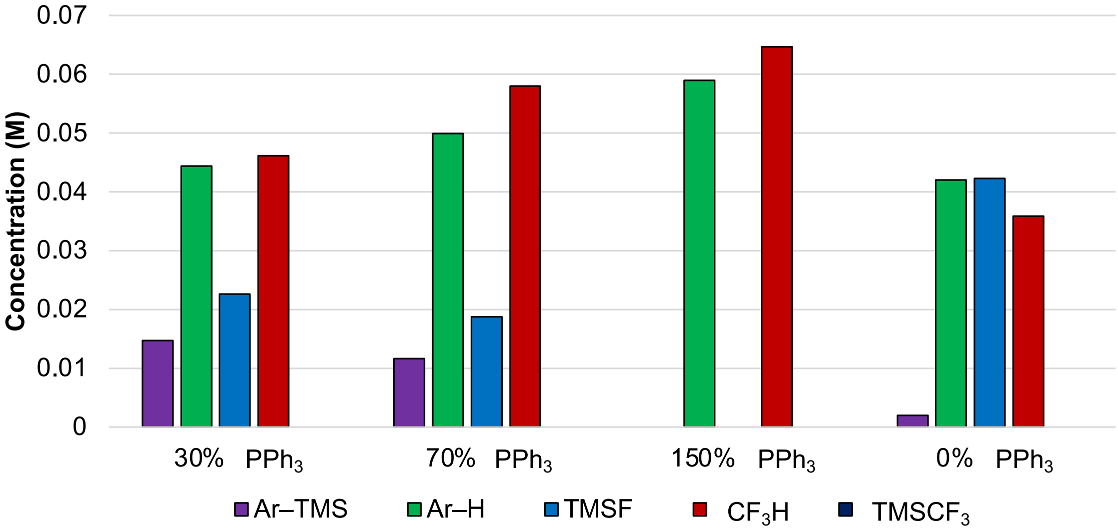

Figure 4.11: Endpoint concentration of active reaction species with triphenylphosphine (PPh_3) addition. Conditions: 0.06 M Ar–H, 0.09 M $TMSCF_3$, 5% TBAT, THF, RT.

Stopped-flow NMR experiments are capable of acquiring NMR spectra within 0.2 seconds of the reaction being initiated, which revealed what was happening during the approximate 80 second delay between t_0 and t_1.[104] From the data shown in Figure 4.12a, the concentration of TBAT plays a vital role in the rate of the reaction. At low levels of TBAT generation of product is very slow, and stalls at approximately 140 seconds. When higher levels of TBAT are present, the same concentration of product is generated in only 10 seconds. The rate of the reaction increases as the concentration of TBAT increases. The initial rates (up to 10 s) follow the same trend as in the published manuscript,[106] however the level of product generated does not. In Figure 4.12a, a mid-range concentration of TBAT yields the most product and the concentration of product then begins to decrease with increasing [TBAT], however the level of product should increase steadily as the concentration of TBAT is increased. This discrepancy is attributed to the increasing water content from the nitrogen supply over time. As previously mentioned, the nitrogen supply contained a significant amount of water, and as the stopped-flow system was run under N_2 the water content in the solutions increased over time. This would reduce the amount of CF_3 anion available to deprotonate Ar–H. The experiments depicted in Figure 4.12a were completed from lowest [TBAT] to highest [TBAT], explaining the plateau in product generation and its subsequent decline.

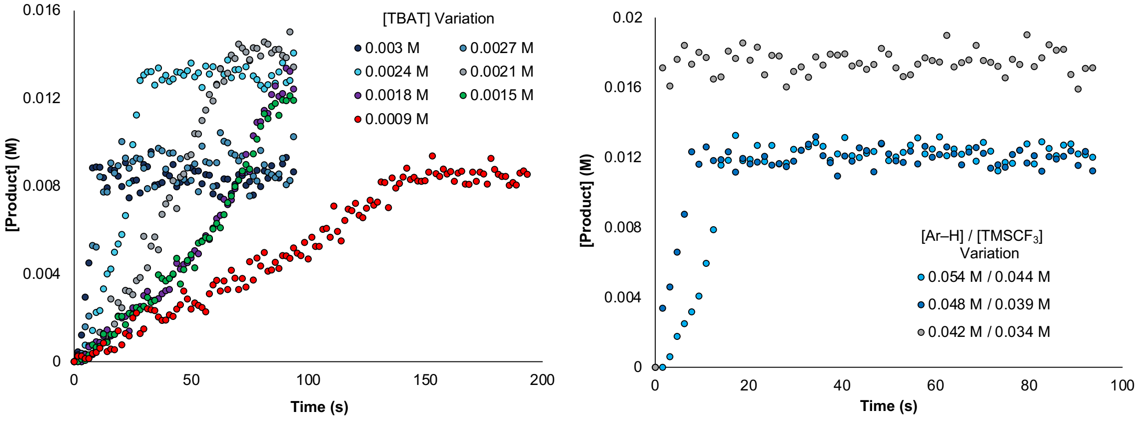

(a) **(b)**

Figure 4.12: ^{19}F-NMR stopped-flow analysis for the reaction between $TMSCF_3$ and 1,3-difluorobenzene, catalyzed by TBAT. Conditions: a) 0.06 M Ar–H, 0.05 M $TMSCF_3$, THF, RT, with [TBAT] varied from 0.0009 to 0.003 M. b) 0.003 M TBAT, THF, RT, with [Ar–H]/[$TMSCF_3$] varied from 0.042 M/0.034 M to 0.054 M/0.044 M.

Varying the [Ar–H/$TMSCF_3$] while maintaining the same [TBAT] in stopped-flow experiments showed that lower concentrations of Ar–H/$TMSCF_3$ proceeded faster and generated more product compared to higher concentrations (Figure 4.12b). Though the exact concentration of TBAT was unchanged, altering the amount of substrate in turn changes the percentage of TBAT present in the reaction. In terms of percentage, the amount of TBAT present was 5.5%, 6.25%, and 7.14% in these experiments. The amount of product generated from 0.054 M and 0.048 M substrate was approximately equal, although the reaction containing 0.048 M substrate proceeded faster.

Based on prior and current research, the mechanism of arylsilylation by $TMSCF_3$ has been proposed as below (Figure 4.13). The main features of this mechanism are: (i) release of $[CF_3]^-$ from $[(CF_3)_2Si(CH_3)_3]^-$; (ii) reaction of an acidic Ar–H substrate with $[CF_3]^-$, producing CF_3H (fluoroform) and $[Ar]^-$; (iii) $TMSCF_3$ silylation of $[Ar]^-$; (iv) regeneration of $[(CF_3)_2Si(CH_3)_3]^-$ via $[CF_3]^-$ complexation with $TMSCF_3$; (v) $[CF_3]^-$ fluoride-transfer to $TMSCF_3$, producing CF_2 and $[(CF_3)Si(F)(CH_3)_3]^-$;[206,207] (vi) $[CF_3]^-$-mediated production of perfluoroalkenes, specifically $[C_{11}F_{23}]^-$; and (vii) TMSF dissociation.

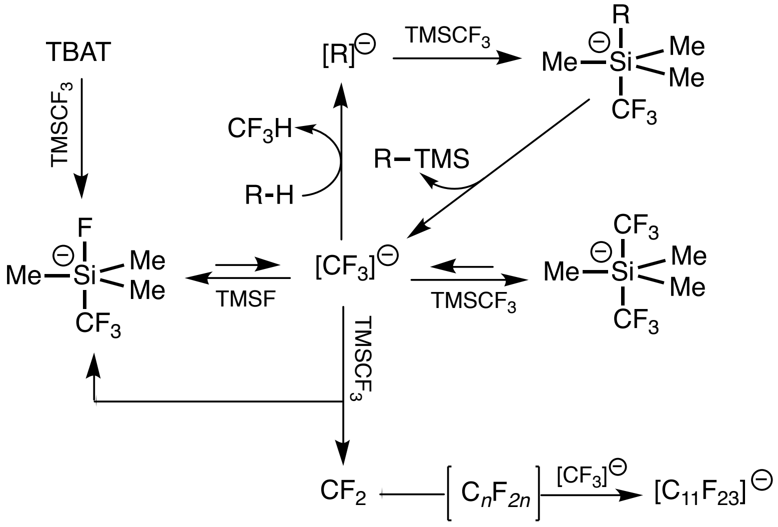

Figure 4.13: Proposed mechanism of anion-catalyzed trimethylsilylation of aromatic C–H bonds by $TMSCF_3$. Figure adapted from Lloyd-Jones and coworkers.[106]

4.5 Conclusion

Overall, these preliminary data, in combination with subsequent acquired data, point to a minimum requirement of [TBAT] in the system. This amount is dictated by the initial concentration of Ar–H and $TMSCF_3$, and reactions performed with [TBAT] below the minimum requirement will stall as a result of $[CF_3]^-$ sequestration. Substrates with highly acidic protons undergo silylation efficiently, and lead to the most productive consumption of $TMSCF_3$. The competing $TMSCF_3$ pathways bring about an inhibitory effect in the presence of excess $TMSCF_3$.

4.6 Materials and Methods

Mestrenova software, version 12.0.1 was used to process all NMR data acquired. All concentration values have been calculated using fluorobenzene as an internal standard.

Reaction monitoring in an NMR tube

All solutions were prepared in an N_2-filled glovebox. $TMSCF_3$ (Fluorochem) was distilled and underwent several freeze-pump-thaw cycles prior to use. Fluorobenzene (Aldrich), 1,3-difluorobenzene (Aldrich), and DME (inhibitor-free, Aldrich) were dried over CaH_2 and degassed. A glovebox solvent system (MBraun SPS-800) dispensed anhydrous THF (inhibitor-free, HPLC grade). Tetrabutylammonium difluorotriphenylsilicate (TBAT) was obtained from Sigma-Aldrich and used without further purification.

Stock solutions of $TMSCF_3$, 1,3-difluorobenzene, and fluorobenzene were prepared in THF by weighing into volumetric flasks, and subsequent storage at –40°C . TBAT stock solutions were prepared freshly in THF on the same day as the experiment. Gas-tight syringes were used to measure and transfer necessary volumes of $TMSCF_3$, 1,3-difluorobenzene, and fluorobenzene stock solutions into an NMR tube. The NMR tube was then equipped with a rubber septum, transferred out of the glovebox, and shaken. For reactions in DME the same procedure was followed, substituting THF for DME in all instances.

The NMR tube was then loaded into a Bruker Avance III 400 MHz spectrometer for ^{19}F-NMR acquisition at a probe temperature of 300 K. An initial 't_0' scan was recorded after shimming (^{1}H) and tuning (^{19}F) without a deuterium lock. The sample was then ejected, and the appropriate amount of TBAT stock solution was injected through the septum using a gas-tight syringe, making the total reaction volume 1 mL. The tube was then shaken vigorously for 30 seconds, and loaded back into the NMR spectrometer. The time between TBAT injection and the first NMR scan was measured. The reaction was monitored over 80 scans, with a 20 second delay time.

Offline reactions

Stock solutions were prepared as mentioned in the previous section. The reaction was set up in a test tube equipped with a septum and a stir bar inside the glovebox. The test tube was then transferred out of the glovebox and allowed to stir at the designated temperature for 1 hour. The reaction solution was then transferred directly into an NMR tube and analyzed.

Reaction monitoring by stopped-flow NMR

Solutions were freshly prepared in volumetric flasks and transferred to Schott bottles inside the glovebox. The stopped-flow NMR system[104] was operated at a total volume of 600 µL at a flow rate of 1 mL/second and a trigger delay of 0.04 seconds. Solution A = 0.1 M fluorobenzene, 0.12 M $TMSCF_3$, and 0.12 M difluorobenzene. Solution B = 0.006 M TBAT. Solution C = THF. The system was flushed with 3 mL of anhydrous THF prior to each run.

Chapter 5

A Mechanistic Investigation of the Pd-catalyzed Cross-Coupling Between *N*-Tosylhydrazones and Aryl Halides

Portions of this chapter have been reproduced from G.T. Thomas, K. Ronda and J.S. McIndoe, *Dalton Transactions*, **2021**, *50*, 15533-15537, and has been adapted with permission from the Royal Society of Chemistry.

5.1 Preface

Conceptualization, proposal, and experimentation was completed by Gilian Thomas. K. Ronda assisted with NMR experimentation. The manuscript was collaboratively written by Gilian Thomas and Prof. Scott McIndoe.

5.2 Abstract

The cross-coupling of *N*-tosylhydrazones and aryl halides forms carbon-carbon bonds, producing 1,1-disubstituted alkenes. Though it has proven extremely useful in several fields of chemistry, its mechanism remains experimentally unexplored. Combining benchtop NMR and real-time mass spectrometry afforded the ability to monitor the catalytic intermediates as well as the rate of product formation.

5.3 Introduction

The formation of carbon-carbon bonds is essential to many fields including, but not limited to, pharmaceutical synthesis,[209] medicinal chemistry,[210,211] natural products,[212–215] and materials.[216] Palladium catalysis is one of the most common and reliable methods of carbon-carbon bond formation, especially for late-stage assembly of two segments in a total synthesis,[217–225] and this area was recognized with the awarding of the 2010 Nobel Prize in Chemistry to Suzuki, Heck, and Negishi.[226]

The Barluenga cross-coupling reaction has emerged more recently as an efficient method of accessing carbon-carbon bonds.[227] A palladium catalyst is used to form a carbon-carbon bond between an *N*-tosylhydrazone and an aryl halide, mainly alkyl bromides.[227] The substrate scope has since been extended to provide access to a variety of products, including but not limited to benzyl halides,[228] aryl nonaflates,[229] and alkenyl halides.[230] *N*-tosylhydrazones as cross-coupling partners alleviate the need for stoichiometric amounts of organometallic reagents, and can easily be produced from the corresponding ketone or aldehyde *in situ*.[231,232] In contrast to the Mizoroki-Heck cross-coupling reaction, the Barluenga cross-coupling does not require an alkene as a coupling partner, and produces a geminal alkene rather than a *trans*-alkene. Due to its advantageous functional group tolerance, this cross-coupling reaction has vast potential in synthetic chemistry, and proven applications in cancer treatments,[233] natural product synthesis,[234,235] and polymer synthesis.[236]

Based on the fact that *N*-tosylhydrazones exhibit nucleophilic behaviour, in combination with previous palladium studies, Barluenga and coworkers[227] proposed the mechanism to begin with oxidative addition of the organic halide to the active palladium(0) complex (Figure 5.1). The *N*-tosylhydrazone undergoes base-mediated decomposition, and the product then binds to the palladium complex, resulting in a palladium-carbene complex. It is suggested that this complex would then undergo migratory insertion of the aryl group to produce an alkyl palladium complex. In the final step, β-hydrogen elimination generates the aryl olefin product, and regenerates the initial palladium(0) active catalyst species. The catalytic mechanism has been studied computationally,[237,238] however reaction intermediates for this catalytic cycle have yet to be observed experimentally.

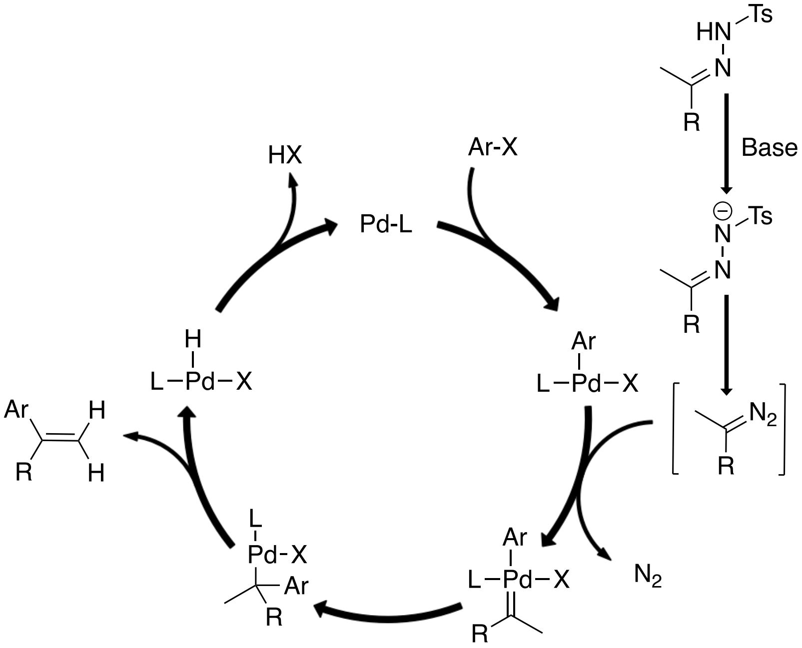

Figure 5.1: Proposed catalytic cycle of the reaction between N-tosylhydrazones and aryl halides.[227]

Herein, we report examination of the mechanism of the cross-coupling between *N*-tosylhydrazones and aryl bromides. Catalytic intermediates are studied in real-time by pressurized sample infusion-electrospray ionization-mass spectrometry (PSI-ESI-MS), and the overall reaction progress is monitored by benchtop NMR spectroscopy

5.4 Results and Discussion

In order to adapt the heterogeneous reaction conditions developed by Barluenga, a reaction screen was carried out in search of homogeneous conditions to facilitate accurate offline sampling, as well as online monitoring via PSI-ESI-MS.[36,68] Several bases, solvents and catalysts were analyzed in combination with the SPhos ligand, but only a few generated product, and only one generated product and was homogeneous (Figure 5.2). The lack of product generated while screening dioxane as a solvent was contradictory to the results of Barluenga,[227] however this is attributed to the use of stock solutions in this reaction screen as not all reagents were soluble in dioxane. A control reaction in dioxane with heterogeneous reaction components was successful outside of the reaction screen. Homogeneous reaction conditions were found in methanol, catalyzed by $Pd(OAc)_2$ with sodium *tert*-butoxide as a base. Further analysis led to a ternary solvent system composed of methanol, toluene, and tetrahydrofuran (1:1:1), as toluene allowed the reaction to be run at higher temperatures and THF improved the solubility of reagents. After the solvent system was finalized, the reaction was performed with the precatalyst $Pd_2(dba)_3$ and was found to increase the rate of the reaction compared to $Pd(OAc)_2$ under these conditions, and was carried forward for reaction monitoring.

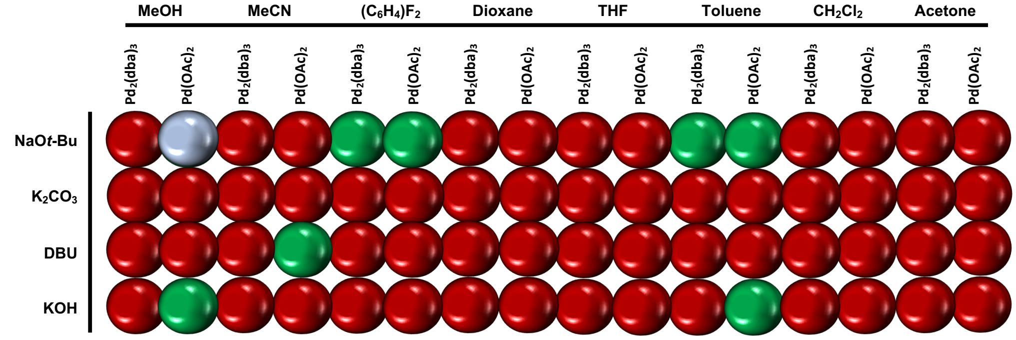

	MeOH		MeCN		$(C_6H_4)F_2$		Dioxane		THF		Toluene		CH_2Cl_2		Acetone	
	$Pd_2(dba)_3$	$Pd(OAc)_2$	$Pd_2(dba)_3$	$Pd(OAc)_2$	$Pd_2(dba)_3$	$Pd(OAc)_2$	$Pd_2(dba)_3$	$Pd(OAc)_2$	$Pd_2(dba)_3$	$Pd(OAc)_2$	$Pd_2(dba)_3$	$Pd(OAc)_2$	$Pd_2(dba)_3$	$Pd(OAc)_2$	$Pd_2(dba)_3$	$Pd(OAc)_2$
NaO*t*-Bu	🟥	🟦	🟥	🟥	🟩	🟩	🟥	🟥	🟥	🟥	🟩	🟩	🟥	🟥	🟥	🟥
K_2CO_3	🟥	🟥	🟥	🟥	🟥	🟥	🟥	🟥	🟥	🟥	🟥	🟥	🟥	🟥	🟥	🟥
DBU	🟥	🟥	🟥	🟩	🟥	🟥	🟥	🟥	🟥	🟥	🟥	🟥	🟥	🟥	🟥	🟥
KOH	🟥	🟩	🟥	🟥	🟥	🟥	🟥	🟥	🟥	🟥	🟥	🟩	🟥	🟥	🟥	🟥

Figure 5.2: Reaction screen results for the cross-coupling between acetophenone tosylhydrazone and bromotoluene, reaction shown above. Red = no product generation; green = product generation and heterogenous mixture; blue = product generation and homogeneous mixture. Conditions: bromotoluene, acetophenone tosylhydrazone, 1% [Pd], 2% SPhos, 70-110°C, 4 hrs. DBU = 1,8-diazabicyclo[5.4.0]undec-7-ene, $(C_6H_4)F_2$ = 1,2-difluorobenzene

The reaction was monitored using a Nanalysis 60 MHz NMR instrument[239] over 48 hours to determine the rate of product formation under homogeneous conditions

(Figure 5.3a). Rather than using a flow cell/flow system,[240] aliquots were withdrawn from the reaction vessel at regular intervals (Figure 5.3b). The reaction was observed to be complete after 24 hours as the concentration of product did not increase from 24 to 48 hours.

Benchtop NMR spectrometers do not require liquid helium nor liquid nitrogen to maintain the temperature of the magnet, and the permanent magnets used can be influenced by the local temperature.[241] To ensure reproducibility, the reaction was performed in triplicate using the now-established homogeneous reaction conditions (Figure 5.3b, inset).

Results from a 300 MHz NMR spectrometer mapped closely to that of the benchtop instrument (Figure 5.4). The 60 MHz spectrometer provided concentration values that were consistently 15% higher due to the difference in acquisition time between the two spectrometers. The 60 MHz spectrometer had a total acquisition time of 4.65 seconds per scan, compared to a 3 second acquisition time on the 300 MHz spectrometer. The shorter acquisition time on the 300 MHz spectrometer means the nuclei are not allowed as much time to relax, leading to varying quantitative results. In the 60 MHz spectrum the aromatic region is amalgamated into two signals, however several other signals are observed in this region on the 300 MHz spectrum. All reactions were quantified using the distinct alkene signal at 5.43 ppm as it occupies a region of the spectrum free from any other signals.

The rate of reaction is approximately constant for hours 1-10, following an induction period of approximately one hour. The overall reaction kinetics appear to be first order. Further interrogation of the rate of reaction (Figure 5.5) showed the reaction was not accelerated by doubling the bromobenzene concentration, but it approximately doubled upon addition of two equivalents of the tosylhydrazone.

Upon introducing para-substituents on the aryl bromide substrate, maximum rates were subjected to a Hammett analysis (Figure 5.6a). Five substituents with

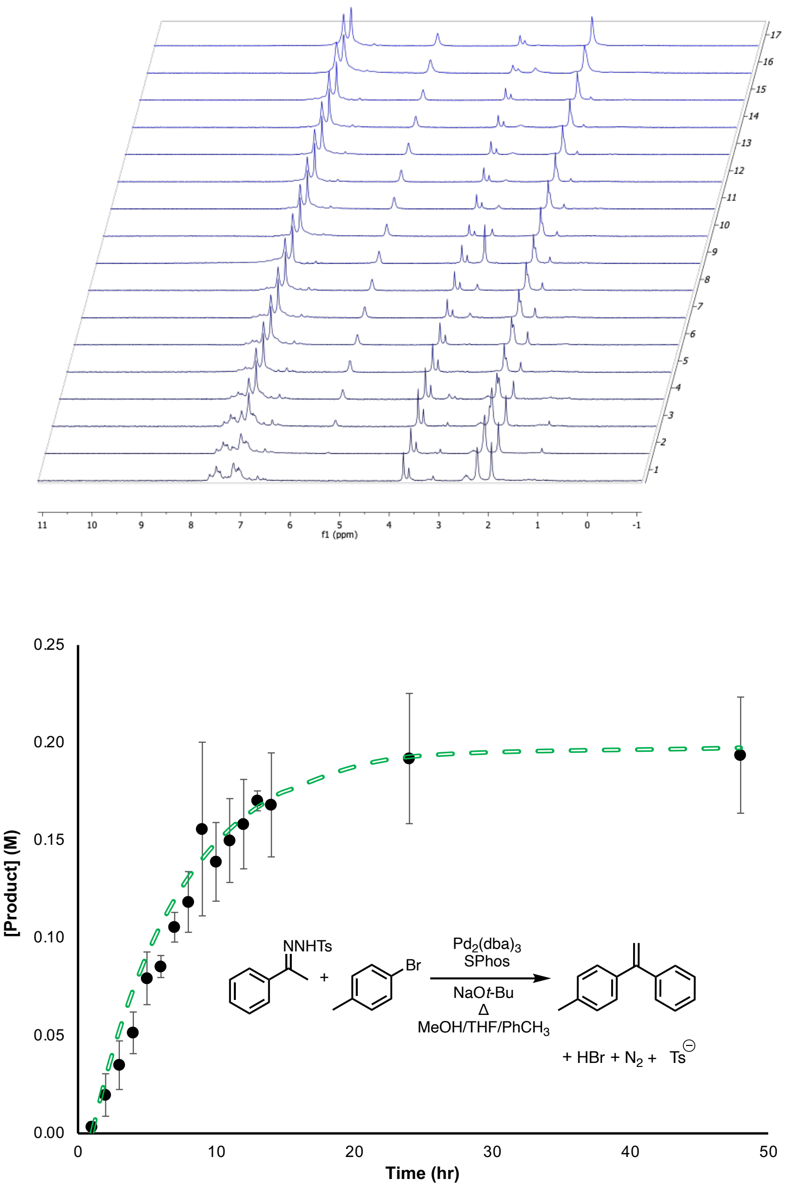

(a)

(b)

Figure 5.3: (a) Representative reaction monitoring spectra on the 60 MHz NMR spectrometer. Bottom = t$_{0hr}$, top = t$_{48hr}$. Product was quantified using the alkene peak at 5.40ppm and 1,2,3-trimethoxybenzene as internal standard. (b) ^{1}H-NMR reaction monitoring using final reaction conditions based on screen (inset) over 48 hours, error bars indicate triplicate experiments. Dashed green line represents first order fit. Conditions: 1% [Pd], 2% SPhos, 0.003 mol acetophenone tosylhydrazone, 0.003 mol bromotoluene, 0.0067 mol NaO*t*-Bu, 70°C.

varying electron-withdrawing and electron-donating capabilities were compared to the H reference substituent, however no clear differences in rate were observed, with

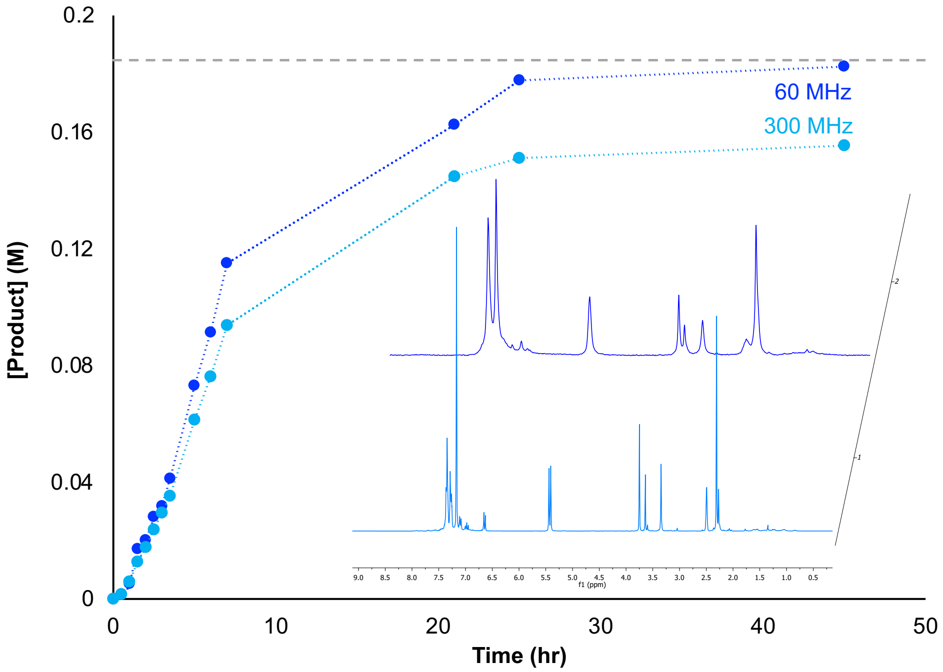

Figure 5.4: ^{1}H-NMR reaction monitoring trace over 48 hours on a 60 MHz NMR spectrometer, and a 300 MHz NMR spectrometer. Inset: representative spectrum after 14 hours on a 60 MHz NMR spectrometer (dark blue), and a 300 MHz NMR spectrometer (light blue). Dashed grey line indicates theoretical yield of product. Conditions: 1% [Pd], 2% SPhos, 0.003 mol acetophenone tosylhydrazone, 0.003 mol bromotoluene, 0.0067 mol NaO*t*-Bu, 70°C

all rates being well within the same order of magnitude. This insensitivity contrasts with data from a related oxidative addition reaction (trendline for which are shown on Figure 5.6a), many of which display the same sort of reactivity pattern as is observed for the oxidative addition step alone. Others have also found similar insensitivity of substitution patterns for bromoanilines in this reaction.[242]

Given the insensitivity to substituent effects, we compared the bromobenzene data to that of iodobenzene and chlorobenzene (Figure 5.7). The chlorobenzene reaction did prove to be much slower, with no product detected before the 3 hour mark in the reaction and a rate of 0.001 mol L^{-1} s^{-1}. Iodobenzene got off to a faster start but the reaction rate after the first hour (0.017 mol L^{-1} s^{-1}) was essentially identical to that of the bromobenzene (0.015 mol L^{-1} s^{-1}). This result suggested that oxidative addition is

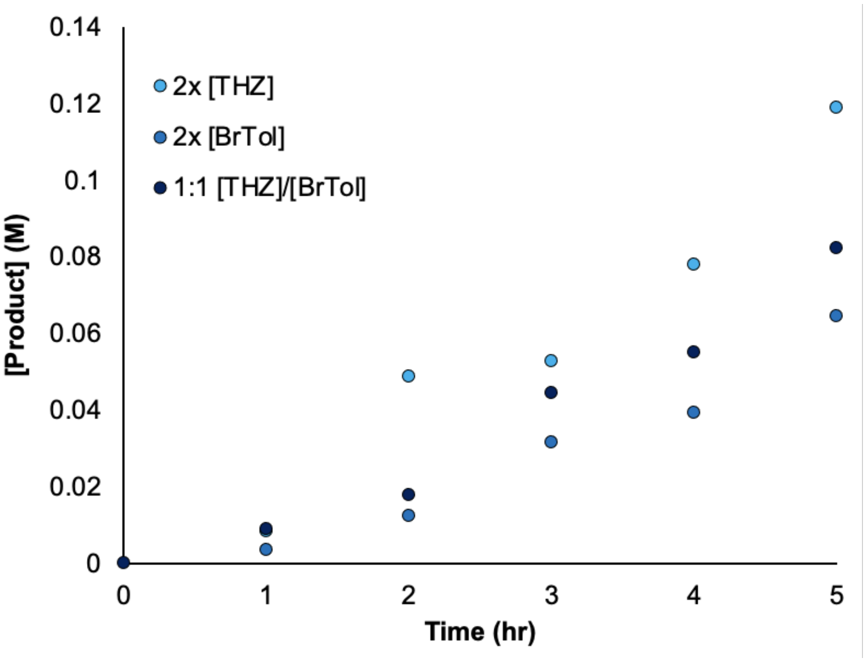

Figure 5.5: Comparison of concentration ratios – 2:1 bromotoluene/tosylhydrazone, vs 2:1 tosylhydrazone/bromotoluene vs 1:1.

not controlling the overall rate of reaction except in the case of the chlorobenzene. The higher initial rate for iodobenzene suggests that the oxidative addition reaction is fast enough that it does not limit the rate even at the start of the reaction. We concluded that the turnover limiting step lies off-cycle for aryl iodides and bromides, this being the transformation of the *N*-tosylhydrazone into the active dinitrogen intermediate. For the chlorobenzene, oxidative addition is most likely the turnover-limiting step.

For further insights into the reaction, we probed the system using electrospray ionization mass spectrometry. ESI-MS analysis requires charged species to accurately observe catalytic intermediates.[166] In this case, a sulfonated SPhos (sSPhos) ligand was an ideal candidate as it is very similar to SPhos, which was used throughout this study up to this point, and has an inherent negative charge. In a control reaction, sSPhos was found to have the same kinetic profile as SPhos, indicating that the presence of a sulfonate group does not significantly change the reaction.

Initial PSI-ESI-MS analysis (Figure 5.8) involved a solution of sSPhos (L, the

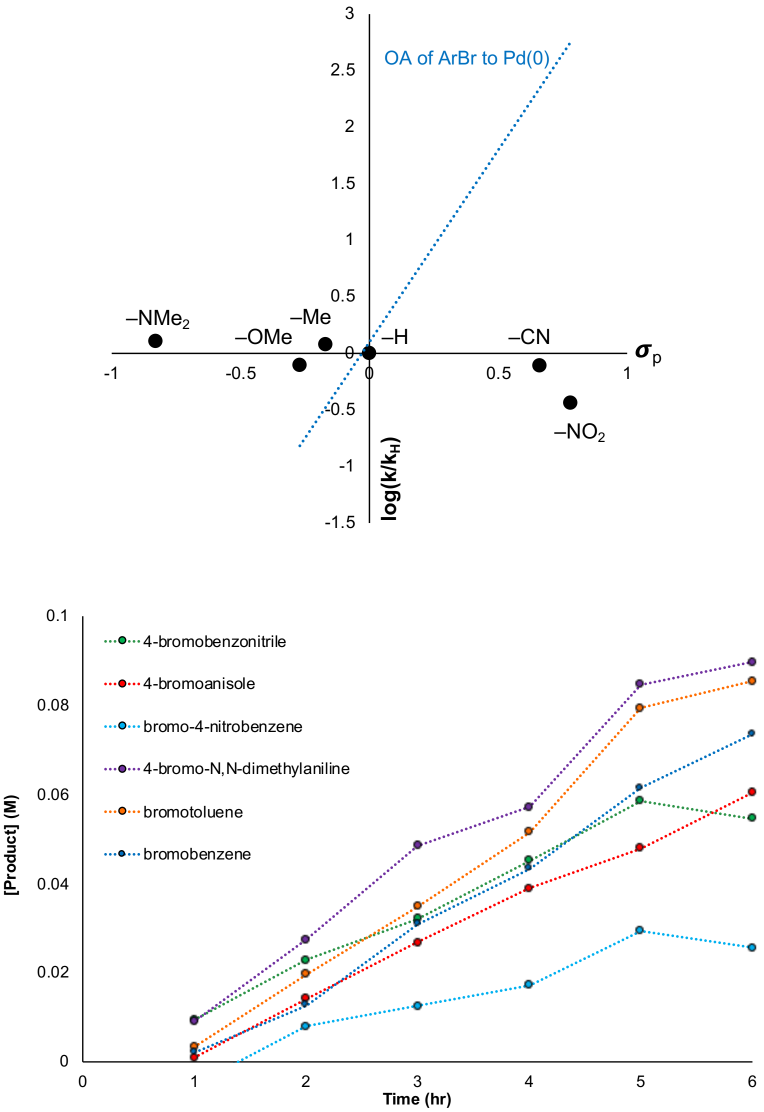

(a)

(b)

Figure 5.6: (a) Hammett plot of $\log(k/k_H)$ vs. Hammett parameter $(\sigma_p)^{243}$ for para-substituted aryl bromides as labelled. k represents the initial reaction rate of each substituent, and k_H represents the initial reaction rate of the H-substituted substrate. The trendline represents the oxidative addition of para-substituted aryl bromides to Pd(0) as reported by Lu et al.[244]; (b) Summary of aryl bromide substrate variation, initial rates from this plot were used in the Hammett analysis.

charge-tagged ligand) to which sequential addition of $Pd_2(dba)_3$, bromotoluene and a mixture of acetophenone tosylhydrazone and sodium *tert*-butoxide were added. Coordination of L to palladium occurred rapidly, with the production of $[LPd(dba)]^-$ proceeding to completion with a half-life of approximately 0.9 minutes. Oxidative

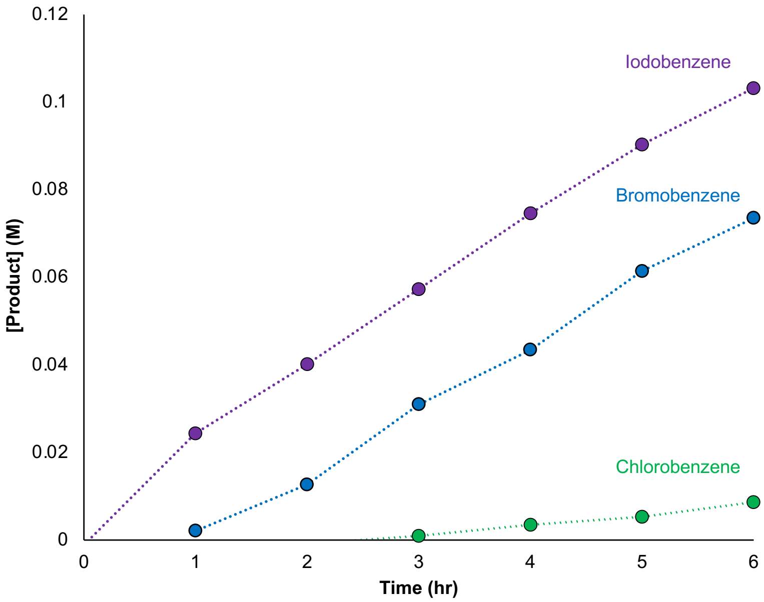

Figure 5.7: Effect of aryl halide on the initial rate of product formation. Conditions: 1% [Pd], 2% SPhos, 0.003 mol acetophenone tosylhydrazone, 0.003 mol ArX, 0.0067 mol NaO*t*-Bu, 70°C.

addition of bromotoluene to $[LPd(dba)]^-$ to form $[LPd(Tol)Br]^-$ was slower, with the disappearance of the $[LPd(dba)]^-$ following pseudo first order kinetics with a half-life of 7.6 minutes.

However, the appearance of product $[Pd(L)(Ar)(Br)]^-$ did not remotely match the amount of reactant being consumed, suggesting that the difference in peak heights was something other than a discrepancy in ion response factor. As there were no other anions appearing during this process, it seemed likely that the "missing" ion intensity was the result of charge neutralization via formation of a zwitterion (not visible in either ion mode). To test this assumption, we looked at the same reaction but with neutral SPhos, so that any species with a positive charge would instead be cationic rather than zwitterionic, and be detectable in the positive ion mode.

$[Pd(SPhos)(Ar)]^+$ was observed to form after the addition of bromotoluene in positive ion mode, suggesting that the zwitterion was indeed Pd(L)Ar (i.e. the positive charge of the complex is cancelled out by the negative charge on the ligand).

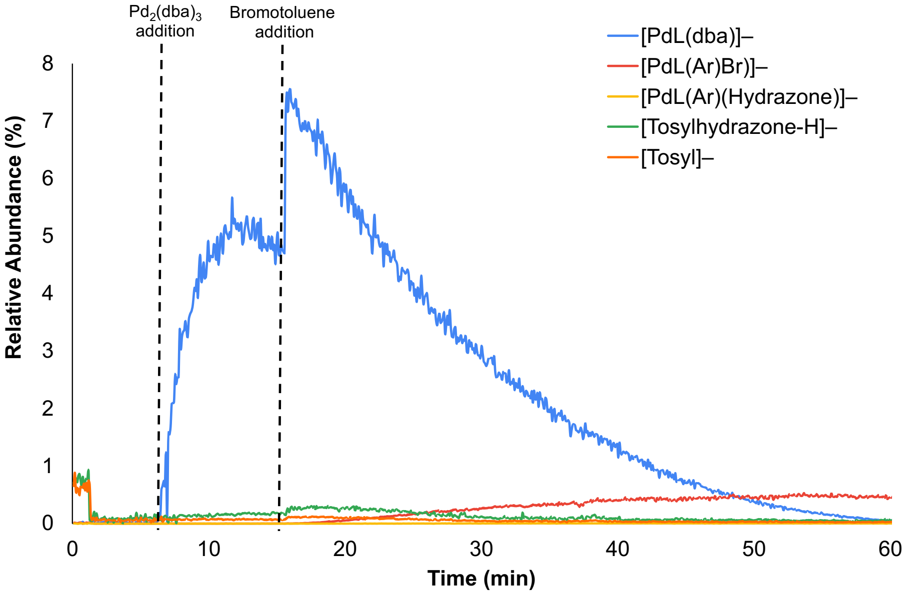

Figure 5.8: PSI-ESI-MS monitoring of the oxidative addition of bromotoluene to Pd(sSPhos)(dba).

To confirm that the missing $[Pd(L)(Ar)(Br)]^-$ is sequestered as Pd(L)(Ar), the mass spectrometer was operated in positive ion mode and negative ion mode simultaneously, monitoring both reactions under identical conditions (Figure 5.9). $Pd_2(dba)_3$ was combined with both SPhos and sSPhos in a flask and allowed to stir at 70°C. The catalyst activation step was deemed complete upon the establishment of a stable signal of $[Pd(L)(dba)]^-$. Bromotoluene was added to the reaction vessel to initiate the oxidative addition step. In negative ion mode, $[Pd(sSPhos)(dba)]^-$ (Figure 5.9, red trace) began decreasing in intensity as expected, and hardly any $[Pd(L)(Ar)(Br)]^-$ formed, as previously observed (Figure 5.9, blue trace). In positive ion mode, an immediate increase in $[Pd(L)(Ar)]^+$ was observed (Figure 5.9, green trace), demonstrating a dissociative equilibrium between [Pd(L)(Ar)(Br)] and Pd(L)(Ar) that lies towards Pd(L)(Ar).

Upon addition of acetophenone tosylhydrazone and sodium *tert*-butoxide the spectrum became completely dominated by deprotonated acetophenone tosylhydrazone and the tosyl anion, indicating that the excess charged base effectively suppressed ions

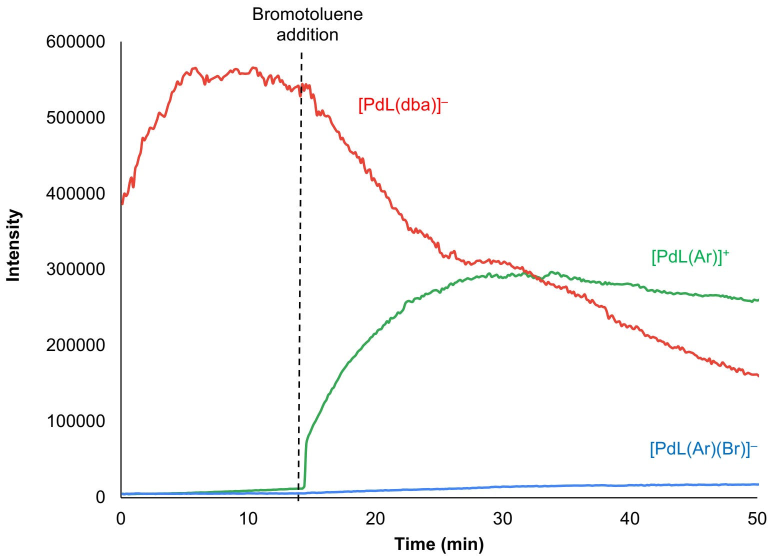

Figure 5.9: Negative ion mode monitoring of $[\mathrm{Pd(sSPhos)(dba)}]^-$ and $[\mathrm{Pd(sSPhos)(Ar)(Br)}]^-$ overlaid with positive ion mode monitoring of $[\mathrm{Pd(SPhos)(Ar)}]^+$.

from any other source, and the spectrum became bereft of any palladium-containing ions (Figure 5.10).

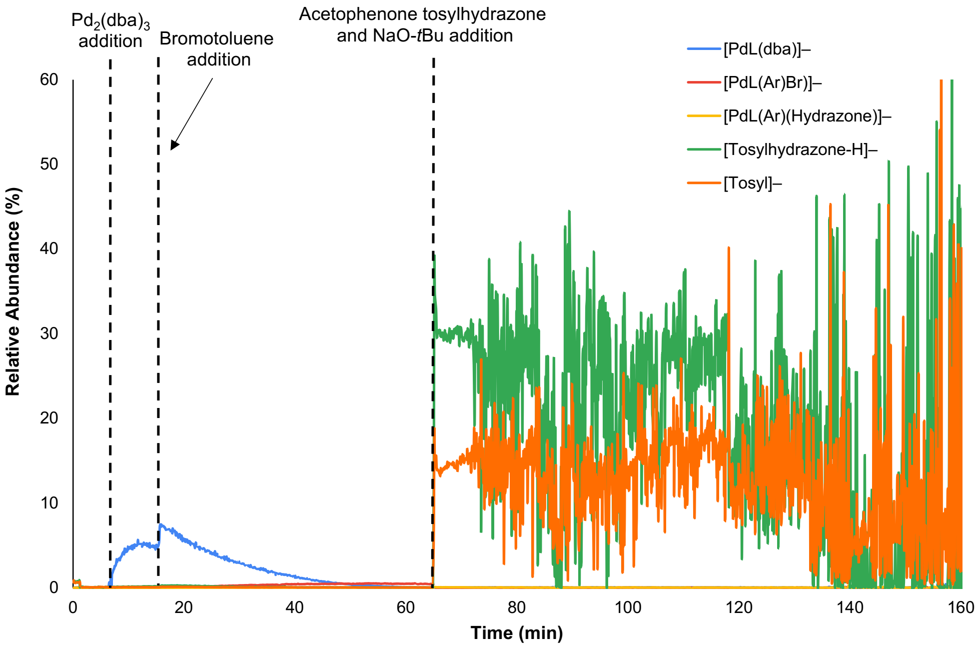

Figure 5.10: Complete PSI-ESI-MS monitoring trace of the Pd-catalyzed reaction between acetophenone tosylhydrazone and bromotoluene in negative ion mode.

5.5 Conclusions

The combination of PSI-ESI-MS and NMR provides complementary information on the mechanism. The ESI-MS results show that the catalyst activation and oxidative addition steps are both fast enough to not affect reaction turnover, but the oxidative addition step is slow enough for aryl bromides that it can account for an induction period not observed for aryl iodides. PSI-ESI-MS also shows that after oxidative addition, the reaction is partitioned primarily as the cationic $[(\text{phosphine})\text{Pd}(\text{Ar})]^+$, although this species is in equilibrium with the neutral (phosphine)Pd(Ar)(X). Addition of tosylhydrazone and base showed that the deprotonation and tosyl dissociation steps are both very fast. We do not see any further palladium-containing intermediates due to ion suppression effects from the added base, but NMR evidence provides pointers as to why we may well not have seen anything even if this effect was not operational. Doubling the bromotoluene concentration had no effect on rate, nor did changing substituents on the aryl ring, but doubling the tosylhydrazone concentration doubled the rate of reaction. Putting all this information together, the evidence points towards a reaction whose palladium-containing resting state is the cationic oxidative addition product in all cases except for chlorobenzenes, and whose overall rate is controlled by its reaction with the diazo derivative derived from the tosylhydrazone decomposition. As such, efforts to improve the reaction should seriously consider focusing on the acceleration of this step.

5.6 Materials and Methods

General Information

Acetophenone tosylhydrazone was synthesized from acetophenone and *p*-toluenesulfonyl hydrazide according to literature procedure.[245,246] SPhos, sSPhos, $Pd_2(dba)_3$, and $Pd(OAc)_2$ were weighed in a N_2-filled glovebox. NMR spectra were analyzed using Mestrenova (12.0.0) software. All substrates were used without purification and purchased from Sigma-Aldrich. All solvents were used without purification and purchased from Fischer Chemical.

Reaction Screen

Stock solutions of acetophenone tosylhydrazone, NaO-tBu, KOH, $Pd_2(dba)_3$, $Pd(OAc)_2$, K_2CO_3, and SPhos were prepared in solvent being screened (i.e. methanol, THF, dioxane, acetonitrile, 1,2-difluorobenzene, toluene, dichloromethane, acetone). These reactions were conducted at 0.167 M with respect to acetophenone tosylhydrazone (1 mL solvent), with 2.2 equivalents of base, 1% [Pd], 2% SPhos. The reaction was heated at 50°C-110°C for 4 hours, and subsequently taken up into pentanes and filtered through celite. After drying in vacuo, the contents were dissolved in DMSO-d_6 and transferred to an NMR tube. Each reaction was analyzed on a Nanalysis NMReady 60PRO spectrometer, 64 ^{1}H scans.

NMR Reaction Monitoring

A Schlenk flask was equipped with 0.0172 g of $Pd_2(dba)_3$ and 0.0283 g SPhos inside the glovebox. Acetophenone tosylhydrazone (0.883 g) and NaO-*t*Bu (0.633 g) were weighed on the bench and added to the flask on a Schlenk line in the fumehood. 1,3,5-trimethoxybenzene was used as the internal standard (0.084 g). THF, toluene and methanol (6 mL each) were then added to the flask and the contents were allowed to stir at 70°C for approximately 1 minute prior to the addition of bromotoluene (369 µL).

Every hour a 1 mL aliquot was taken into 2 mL of pentane. This solution was then filtered through celite, and dried down. The contents were then re-suspended in DMSO-d_6 and analyzed on a Nanalysis NMReady 60PRO spectrometer, 64 ^{1}H scans and/or a Bruker AV III 300 MHz NMR spectrometer.

MS Reaction Monitoring

A PSI flask[68] was equipped with SPhos (0.0019 g)/sSPhos (0.0023 g), and

$Pd_2(dba)_3$ (0.0011 g) in 18 mL of 1:1:1 methanol/THF/toluene and stirred at 70°C. A pressure of 6 psi was applied to the flask to initiate pressurized sample infusion[36] into a Waters Acquity triple quadrupole mass spectrometer. Bromotoluene (21 µL) was added upon completion of catalyst activation. After the oxidative addition was complete, acetophenone tosylhydrazone (0.059 g) and NaO-*t*Bu (0.043 g) were added to the reaction flask. THF was dried over CaH_2 and distilled prior to use for MS analysis to remove BHT additives.

Chapter 6

Trichloro(Dinitrogen)Platinate(II)

Portions of this chapter have been reproduced from G.T. Thomas, S. Donnecke, I. Paci and J.S. McIndoe, *Chemistry – A European Journal*, **2020**, *26*, 12359–12362. and adapted with permission from Wiley-VCH GmbH.

6.1 Preface

All experimental data was acquired by Gilian Thomas. Computational analysis was completed by Sofia Donnecke under the supervision of Prof. Irina Paci. The manuscript was written collaboratively by Gilian Thomas, Sofia Donnecke, and Prof. Scott McIndoe.

6.2 Abstract

Zeise's salt, $[PtCl_3(H_2C{=}CH_2)]^-$ is the oldest known organometallic complex, featuring ethylene strongly bound to a platinum salt. Many derivatives are known, but none involving dinitrogen, and indeed dinitrogen complexes are unknown for both platinum and palladium. Electrospray ionization mass spectrometry of $K_2[PtCl_4]$ solutions generate strong ions corresponding to $[PtCl_3(N_2)]^-$, the identity of which was confirmed through ion-mobility spectrometry and MS/MS experiments that proved it

to be distinct from its isobaric counterparts $[PtCl_3(C_2H_4)]^-$ and $[PtCl_3(CO)]^-$. Computational analysis established a gas-phase platinum–dinitrogen bond strength of 116 $kJmol^{-1}$, substantially weaker than the ethylene and carbon monoxide analogues but stronger than for polar solvents such as water, methanol and dimethylformamide, and strong enough that the calculated N–N bond length of 1.119 Å represents weakening to a degree typical of isolated dinitrogen complexes.

6.3 Introduction

Zeise's salt, $[PtCl_3(H_2C{=}CH_2)]^-$, is the oldest known organometallic complex and was originally met with some criticism.[247] It was made by Zeise in 1830 by boiling platinum tetrachloride in ethanol and isolating a salt he called "entzündliches Kali-Platin-Salz" (flammable potassium platinum salt), noting that it had a long-lasting metallic flavor.[248] Zeise's salt was later prepared by Birbaum using ethylene,[249] and eventually its structure was determined crystallographically.[250,251] The ethylene binds side-on, in a bonding mode described by the Dewar–Chatt–Duncanson model.[252–256] Zeise's salt inspired generations of research into organometallic chemistry, and numerous derivatives have been prepared with a variety of 2-electron ligands replacing ethylene.[257–261]

Because the ethylene ligand binds tenaciously to the platinum, we were interested to see if it would remain bound even during the desolvation process during electrospray ionization mass spectrometry (ESI-MS). Monodentate alkenes tend to bind weakly to metal centers, and it is generally difficult to preserve their coordination even under the mildest of ESI-MS conditions.[262,263] Zeise's salt can be readily prepared via $SnCl_2$ catalyzed ligand substitution of $[PtCl_4]^{2-}$ with ethylene,[264] and substitution of Cl for heavier halides has been explored.[265,266] When we examined a $[PtCl_4]^{2-}$ solution in water a relatively minor peak at the correct *m/z* and with the expected isotope pattern for $[PtCl_3(C_2H_4)]^-$ was observed, despite the absence of ethylene. That ion could be subjected to collision-induced dissociation (CID) in a conventional product ion MS/MS experiment, and it readily lost a neutral species of 28 Da. Nitrogen, like ethylene, also has a molecular weight of 28 Da, and is present in abundance during the ESI-MS experiment thanks to its use as a desolvation gas, and was a possible explanation for this ion. While many dinitrogen complexes have been reported for metal centers in Groups 3–9, some simple,[267–271] some with carefully constructed coordination environments,[272–280] and others evolved for nitrogen fixation,[281–285] such complexes are less common in Groups 10 and 11. Isolated dinitrogen complexes involving platinum are unknown. $Pt–N_2$ bonds have been studied under specialized conditions using infrared spectroscopy, laser ablation, and matrix isolation.[286–289] A few ions observed mass spectrometrically have been tentatively assigned to platinum dinitrogen species, including $[Pt(NH_3)_2(N_2)Cl]^+$[290] and $[Pt(NH_3)_2(N_2)OH]^+$.[291] Schwarz and co-workers reported phenanthroline complexes of several transition metals, including Pt, forming an adduct with N_2 buffer gas inside the spectrometer.[292] $[PtCl_3N_2]^-$ ions were assigned in the experimental section of a study on bicyclic antitumor platinum(IV) complexes,[293] but escaped without comment in the manuscript. Interest in dinitrogen complexes has been long-standing due to the inherent difficulty of activating the very strong dinitrogen bond, a prerequisite for involving the molecule in catalytic processes.[294]

We provide detailed evidence for the robustness of gas-phase $[PtCl_3(N_2)]^-$ using a multifaceted approach: accurate mass analysis, MS/MS studies, ion-mobility spectrometry (IMS), and computational chemistry. We compared all molecules of mass 28 Da that can act as a ligand for the $[PtCl_3]^-$ fragment: ethylene, dinitrogen, and carbon monoxide. The resulting $[PtCl_3(L)]^-$ complexes are numbered **1** ($L=C_2H_4$), **2** ($L=N_2$) and **3** (L=CO).

6.4 Results and Discussion

$NEt_4[PtCl_3(CO)]$ and $K[PtCl_3(C_2H_4)]$ complexes were synthesized for direct comparison to the suspected $[PtCl_3(N_2)]^-$ complex. Accurate mass data were collected on a Synapt G2-Si instrument for all species. As shown in Figure 6.1, $[PtCl_3(C_2H_4)]^-$, $[PtCl_3(N_2)]^-$ and $[PtCl_3(CO)]^-$ all produce very similar isotope patterns (black), but the exact positions of the individual peaks are different (coloured traces). These data clearly depict the distinct differences in exact mass for each of these complexes, and provide strong evidence of the authenticity of the N_2 complex **2**.

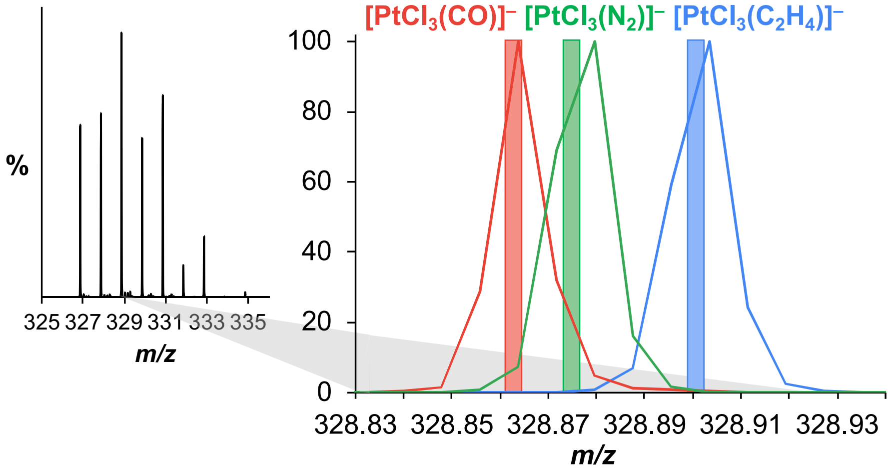

Figure 6.1: An overlaid spectrum of all three Pt complexes (left) shows the high resolution needed to distinguish these species. Individual peaks were identified (right) in experimental data for $[PtCl_3(C_2H_4)]^-$ (**1**, blue), $[PtCl_3(N_2)]^-$ (**2**, green), and $[PtCl_3(CO)]^-$ (**3**, red).

Modern mass spectrometers are capable of collecting corroborating data on the identity of ions that have the same nominal mass. Fragmentation via collision-induced dissociation produces diagnostic product ions based on the strength of the bonds.[295–298] In the case of organometallic compounds, weakly bound ligands will dissociate at a lower collision energy compared to more strongly bound ligands. The product ion scans reveal a loss of m/z 28, meaning that the Cl^- ligands remain bound while the L ligand dissociates; for Zeise's salt this is the ethylene ligand.

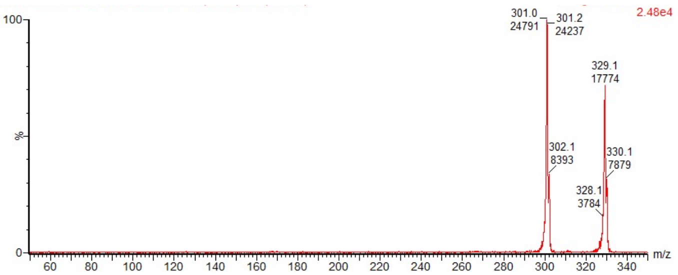

Figure 6.2: Analysis of K_2PtCl_4 in water, product ion scan (CE = 5 V) of *m/z* 328.8 on Waters Acquity triple quadrupole detector.

MS/MS experiments on each of **1**, **2** and **3** showed clear differences in terms of how difficult it is to remove each ligand (Figure 6.3). The N_2 ligand is the most weakly bound as its relative intensity was reduced to 50% of its initial intensity at a collision energy of just 2.7 V. The CO ligand is strongly bound to the Pt centre, and requires a much higher collision energy to dissociate; 13.1 V was required to reduce this complex to 50% of its initial intensity. The binding strength of the ethylene ligand of Zeise's salt falls in between that of N_2 and CO, requiring a collision energy of 10.3 V to produce the same degree of dissociation.

Ion-mobility data for each of the three complexes was collected on a Waters Synapt G2-Si instrument (Figure 6.4). Two peaks for **1** arise because the source and flight tube are filled with N_2 and some displacement of ethylene by dinitrogen occurs, thus resulting in ion mobility signals for a mixture of **1** and the dinitrogen complex **2**. The singular peak for **3** suggests little or no displacement of the carbonyl ligand by N_2, in keeping with its greater tenaciousness as a ligand. The difference in drift time for **3** and **1** is somewhat surprising, given the similarities in size of the two complexes (same nominal mass and number of atoms), but drift times are dependent on factors including ion-neutral interactions,[299] drift gas polarizability,[300,301] shape,[302] and charge state.[303] Additionally, ions with a more delocalized charge are less prone to forming short-lived heterodimers with the drift gas molecules.[292,304,305] Because CO is more highly polarized than N_2 (see Figure 6.4 insets of electrostatic potentials

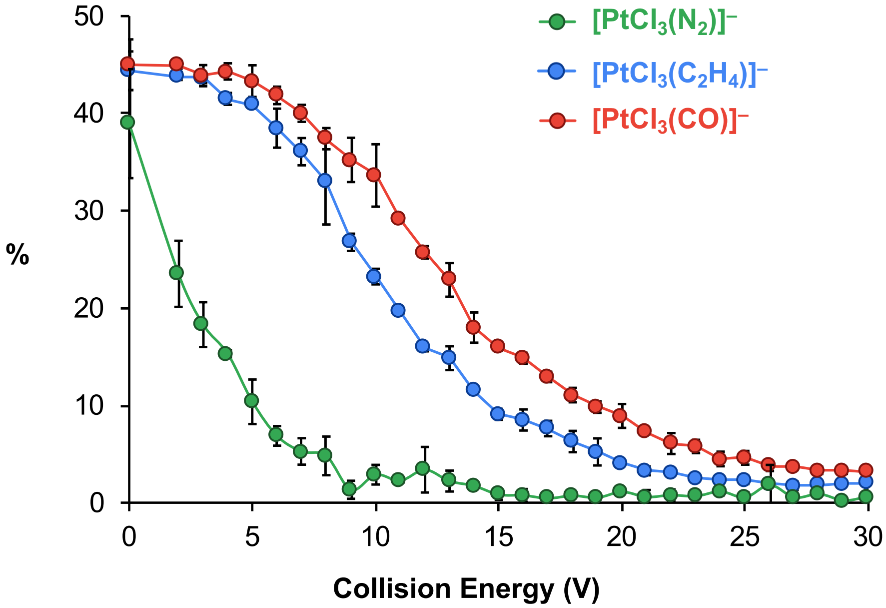

Figure 6.3: MS/MS data obtained for $[PtCl_3(C_2H_4)]^-$ (blue), $[PtCl_3(N_2)]^-$ (green) and $[PtCl_3(CO)]^-$ (red) showing loss of $[PtCl_3(L)]^-$ as L is removed. Collision energy at 50% of initial relative abundance: $[PtCl_3(N_2)]^-$ = 2.7 V, $[PtCl_3(C_2H_4)]^-$ = 10.3 V, $[PtCl_3(CO)]^-$ = 13.1V.

mapped on to the electron density iso-surface) it exhibits a longer drift time despite their similarity in collisional cross-section.

Computational analysis of the three ions allows us to assess the strength of binding of the ligands in the gas phase, and in keeping with the tandem mass spectrometric results, the calculations showed the order of binding strength was $CO>C_2H_4>N_2$. Because of the low number of atoms, calculations could be performed at a high level. Binding energies of N_2, CO, and C_2H_4 to $[PtCl3]^-$ were calculated using density functional theory (DFT) at the RI-UB2PLYP/def2-TZVPP level of theory,[307] with D3 dispersion corrections[308] using ORCA 4.0 software.[309] The results predict the strongest bond energies for CO, then ethylene, then dinitrogen, fully supporting the MS/MS (Figure 6.3) and ion-mobility results (Figure 6.4).

The ligand dissociation energies for L ligands in complexes **1**, **2**, and **3** were compared to solvent molecules and O_2 for context (Figure 6.5 and 6.6). N_2 was found

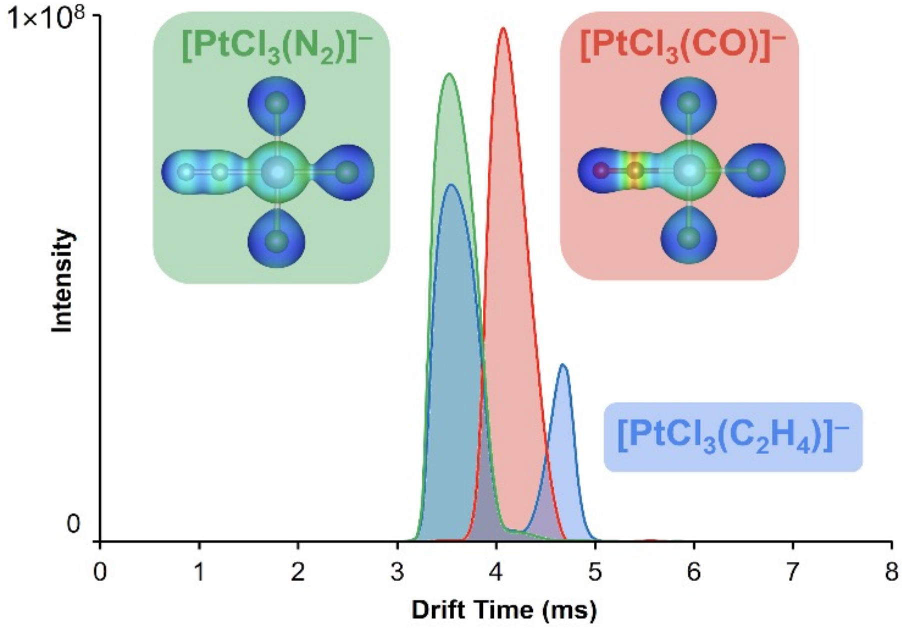

Figure 6.4: Ion-mobility spectrum for $[PtCl_3(C_2H_4)]^-$ (blue), $[PtCl_3(N_2)]^-$ (green) and $[PtCl_3(CO)]^-$ (red); the area of each trace has been normalized to the same value. Structures of $[PtCl_3(N_2)]^-$ (left) and $[PtCl_3(CO)]^-$ (right) show the electrostatic potential (red=0.8, blue=0.1) calculated with the orca_vpot keyword and plotted as a cube file[306] mapped onto the electron density iso-surface (0.1e Å^3)

to be a slightly better ligand than methanol and slightly worse than acetonitrile. Other polar ligands examined were water and dimethylformamide (DMF), and these both have markedly lower binding energies than N_2. Dioxygen was the weakest binder of all, with less than half the binding strength of N_2 (unlike N_2, the strongest binding mode for O_2 was side-on rather than end-on).

Comparing the calculated N_2 bond length of 1.112 Å in **2** to established bond lengths in structurally characterized dinitrogen complexes is instructive. Examination of iridium (the closest analogue to Pt) complexes of dinitrogen in the Cambridge Structural Database (36 unique bond lengths are known), we find the N_2 distance falls in the range 0.982 Å[310] to 1.183 Å,[311] with an average of 1.117 Å, strikingly close to that calculated for **2**. The bond length in **2** is most similar to that in an iridium pincer complex prepared by Brookhart and co-workers in which the dinitrogen ligand (N–N distance 1.119 Å) is bound to two iridium centers.[312]

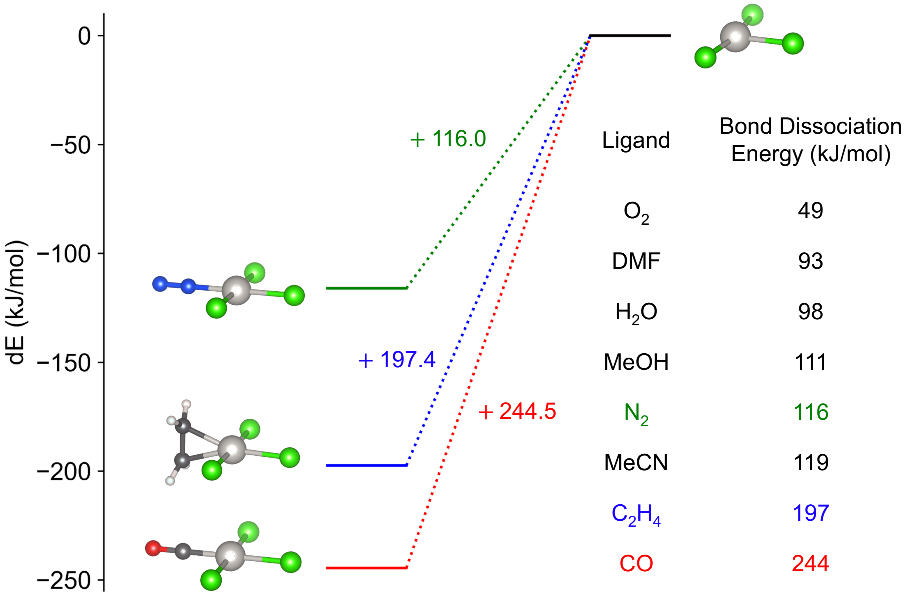

Ligand	Bond Dissociation Energy (kJ/mol)
O_2	49
DMF	93
H_2O	98
MeOH	111
N_2	116
MeCN	119
C_2H_4	197
CO	244

Figure 6.5: Ligand dissociation energies(LDE) calculated as reaction enthalpies for the dissociation reaction $PtCl_3–L \longrightarrow PtCl_3 + L$. Comparison of C_2H_4, N_2 and CO (diagram) to that of common readily available compounds (see the table).

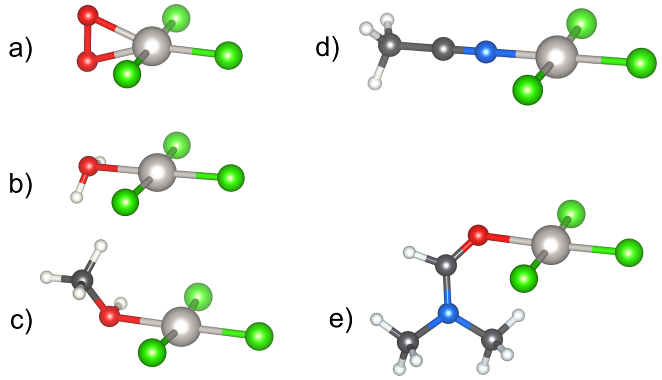

Figure 6.6: Structures of common compounds whose binding energies were calculated. a) O_2; b) H_2O; c) MeOH; d) MeCN; e) Me_2NCHO

6.5 Conclusion

Given the surprisingly high gas-phase and calculated stability of this platinum dinitrogen complex, **2** makes for a feasible synthetic target. The relatively high strength of binding may provide exploitable levels of activation of the dinitrogen molecule in water, leading to new opportunities in functionalization and catalysis.

6.6 Materials and Methods

Potassium tetrachloroplatinate(II) ($K_2(PtCl_4)$), tin(II) chloride dihydrate, and sodium tetraphenylborate ($NaB(Ph)_4$) were purchased from Millipore Sigma (Oakville, Canada). Concentrated hydrochloric acid and acetone were purchased from Fisher Scientific (Ottawa, Canada). HP300 4.8 nitrogen and EY CP80 ethylene were purchased from Airgas (Radnor, USA). A Waters (Milford, USA) Synapt G2-Si ion mobility quadrupole time-of-flight mass spectrometer, and a Waters Acquity triple quadrupole mass spectrometer were used for analysis.

Potassium Trichloro(ethene)platinate(II) Synthesis

Procedure adapted from Chock et al.[264] A 500 µL solution of hydrochloric acid (5 M) was prepared in a test tube, 0.052 g of potassium tetrachloroplatinate(II) was added and the tube was sealed with a rubber septum and parafilm. A stream of gaseous ethylene was bubbled through the solution via PEEK tubing (ID 0.5 cm), with a needle functioning as a gas outlet, for 30 minutes. Tin(II) chloride dihydrate (0.0002 g) was placed into an Eppendorf tube, sealed with a septum, and flushed with nitrogen. After 30 minutes, 220 µL of deoxygenated distilled water was added to the Eppendorf tube, and 100 µL of the $SnCl_2$ solution was added to the test tube containing K_2PtCl_4. The solution was stirred under a constant stream of gaseous ethylene for 4 hours. The ethylene line was removed, and the yellow solution was warmed to 40-45°C, followed by cooling in an ice bath. Upon precipitation of yellow needle crystals, the remaining liquid was removed and refrigerated. The $K[PtCl_3(C_2H_4)]$ crystals were dried *in vacuo* and stored at 4°C.

Tetraethylammonium Trichlorocarbonylplatinate(II) Synthesis

Procedure adapted from Spaulding et al.[313] Carbon monoxide was bubbled through an acetone solution of Zeise's salt for 10 minutes, followed by addition of tetraethylammonium chloride. This solution was stirred for 1 hour, and then its volume was reduced *in vacuo*. The complex was precipitated via hexane addition.

Mass Spectrometry

All solutions were made in dimethylformamide, and injected via syringe pump at 20 µL/min. The Waters Synapt G2-Si was operated in negative ion mode at a capillary voltage of -1.95 kV, a sampling cone voltage of 20 V, and a source offset voltage of 40 V. The source temperature was 120°C, and the desolvation temperature 350°C. The desolvation and cone gas flow rates were 100 L/hr, and the nebuliser was set to 5 bar. The triple quadrupole detector was operated in negative ion mode at a capillary voltage of -2.95 kV, a cone voltage of 10 V, and extraction cone voltage of 3 V. The desolvation and cone gas flow rates were 100 L/hr, the source temperature was 120°C and the desolvation temperature 350°C. Accurate mass data and drift times were collected on the Waters Synapt G2-Si, $[BPh_4]^-$ was used as an internal standard. Collisional ramping experiments were conducted on the triple quadrupole detector in the range of 2-45 V, the collision energy was increased by 1 V every 10 seconds.

Computational Analysis

$[PtCl_3(L)]^-$ dissociation energies were calculated using density functional theory (DFT) at the RIUB2PLYP/def2-TZVPP level of theory,[307] with D3 dispersion corrections,[308] using ORCA 4.0 software.[309]

Chapter 7

Summary and Outlook

Catalytic reaction monitoring can be accomplished using a variety of methods, including MS and NMR. The two techniques have proven to be complementary to one another whereby MS monitors the catalytic intermediates, while NMR monitors the formation of product. When used to analyze the Barluenga cross-coupling reaction, it was found that the turnover-limiting step is not held within the catalytic cycle, rather is an off-cycle transformation from the *N*-tosylhydrazone into the active species. Future research efforts should be focused on optimizing this transformation to decrease overall reaction time. For example, pre-forming this active intermediate in solution would likely lead to faster product generation upon addition to the aryl halide substrate. However, the active intermediate is prone to decomposition in both protic and aprotic solvent, so immediate addition is required. Additional mechanistic information may be discovered using a positively charged ligand to monitor the reaction in positive ion mode. This would effectively prevent convolution of the spectrum as a result of the substrate and base addition, and present only catalytic species. Although, positively charged palladium complexes are more prone to oxidation.

To facilitate online real-time MS monitoring, a specialized Schlenk flask was designed in such a way that vulcanized rubber contaminants are prevented from entering the reaction mixture during pressurized sample infusion. PSI-ESI-MS has since been used to investigate other catalytic reactions,[314] and is the technique of choice in the

McIndoe group. The impact of this work is several-fold – one, it highlights the problematic nature of antioxidant leaching; two, it provides assignments to negatively-charged ions that may have proved puzzling for other experimentalists; and three, it provides a simple solution to avoid the contaminants getting into the solution in the first place.

PSI-ESI-MS was used to study the Buchwald-Hartwig amination reaction using MRM scans to improve sensitivity, and quantify catalytic intermediates. Relative reaction rates for each step in the catalytic cycle were observed, and it was found that the reductive elimination is the turnover limiting step. The use of a commercially available Buchwald-type ligand with an inherent negative charge, sulfonated SPhos (sSPhos), has since lead the Buchwald group to create alternative sulfonated ligands on a large scale, such as sulfonated BrettPhos.[315] Additionally, this mode of analysis can be applied to any reaction in which order of addition is important, or to investigate order of addition. It has since been used to study the Suzuki polycondensation reaction.[316] It was noted that compared to other scan modes, MRM is the most advantageous due to the significant improvement in signal-to-noise ratios, however this method is only suitable for known species of interest. It is recommended that a full scan be performed in both positive and negative ion mode for potential observation of unknown/unexpected active species.

When used in combination with IMS, MS may also be used for metal complex discovery, as in the case of $[PtCl_3(N_2)]^-$. Separation of metal complexes based on shape can now be used to differentiate between isobaric catalytic transformations, such as a palladatropic rearrangement or migratory insertion. This technique may also be applied to complex reaction monitoring in real-time of reactions containing isobaric species. A current application in the McIndoe group involves monitoring a ring-closing metathesis reaction of various ring sizes. Without IMS, only certain ring sizes may be monitored simultaneously as some of the products overlap with other substrates. IMS allows all ring sizes to be monitored simultaneously due to the separation based on shape, a ring-closed species will have a shorter drift time than a ring-open species of the same *m/z* as it experiences less friction in the drift tube. Because the isobaric species can now be separated, each substrate and product can be accurately quantified. However, resolution comes into question when examining isomerization of large isobaric complexes possessing ancillary ligands, as these isomers may be indistinguishable due to their subtle change in shape.

In the case of NMR, ^{19}F-NMR was used to study the mechanism of CF_3 liberation from $TMSCF_3$ in a C–H silylation reaction. ^{19}F-NMR provided the ideal platform for this reaction as the protonated solvent peak did not obstruct the spectrum, and all active species were functionalized with fluoride, and the 1,3-difluorobenzene substrate yielded an acidic proton at the 2-position. Alternative non-fluorinated aryl substrates would present challenges in observation of the active $[CF_3]^-$ species if ^{1}H-NMR is the method of choice. The original stopped-flow NMR system and parameters used provided a stepping stone to the newest stopped-flow NMR system developed by the Lloyd-Jones group which facilitates analysis in under one second.[317] The ability to analyze complex reactions on a short timescale opens up possibilities for elucidation of rapid reactions, such as the protodeboronation of 2,3,4,5,6-pentafluorophenyl boronate.

References

[1] Gross, J. H. *Mass Spectrometry*, 3rd ed.; Springer International Publishing: Cham, 2017.

[2] Griffiths, I. *Rapid Commun. Mass Spectrom.* **1997**, *11*, 2–16.

[3] De Hoffmann, E.; Charette, J.; Stroobant, V. *Mass Spectrometry Principles and Applications*; John Wiley & Sons, Ltd.: Paris, France, 1996.

[4] Glish, G. L.; Vachet, R. W. *Nat. Rev.* **2003**, *2*, 141–150.

[5] Yunker, L. P.; Stoddard, R. L.; McIndoe, J. S. *J. Mass Spectrom.* **2014**, *49*, 1–8.

[6] Vikse, K. L.; McIndoe, J. *J. Mass Spectrom.* **2018**, *53*, 1026–1034.

[7] Dole, M.; Mack, L.; Hines, R.; Mobley, R.; Ferguson, L.; Alice, M. *J. Chem. Phys.* **1968**, *49*, 2240.

[8] Fenn, J. B.; Mann, M.; Meng, C.; Wong, S.; Whitehouse, C. *Science (80-.).* **1989**, *246*, 4926.

[9] Dawson, P. H. *Quadrupole Mass Spectrometry and its Applications*; Elsevier Scientific Publishing Company: New York, 1976.

[10] Harris, D. *Quantitative Chemical Analysis*, 7th ed.; W.H. Freeman and Company: New York, 2007.

[11] Hill, H. H.; Siems, W. F.; St Louis, R. H.; McMinn, D. G. *Anal. Chem.* **1990**, *62*, 1201–1209.

[12] Lanucara, F.; Holman, S. W.; Gray, C. J.; Eyers, C. E. *Nat. Chem.* **2014**, *6*, 281–294.

[13] Campuzano, I. D.; Lippens, J. L. *Curr. Opin. Chem. Biol.* **2018**, *42*, 147–159.

[14] May, J. C.; Mclean, J. A. *Anal. Chem.* **2015**, *87*, 1422–1436.

[15] D'Atri, V.; Porrini, M.; Rosu, F.; Gabelica, V. *J. Mass Spectrom.* **2015**, *50*, 711–726.

[16] Giles, K.; Pringle, S.; Worthington, K.; Little, D.; Wildgoose, J.; Bateman, R. *Rapid Commun. Mass Spectrom.* **2004**, *18*, 2401–2414.

[17] Manard, M. J.; Kemper, P. R. *Int. J. Mass Spectrom.* **2016**, *402*, 1–11.

[18] Günther, H. *NMR Spectrosc. Basic Princ. Concepts Appl. Chem.*, 3rd ed.; Wiley-VCH: Weinheim, 2013.

[19] Pavia, D.; Lampman, G.; Kriz, G.; Vyvyan, J. *Introduction to Spectroscopy*, 5th ed.; Brooks Cole: Belmont, 2015.

[20] Termopoli, V.; Torrisi, E.; Famiglini, G.; Palma, P.; Zappia, G.; Cappiello, A.; Vandergrift, G. W.; Zvekic, M.; Krogh, E. T.; Gill, C. G. *Anal. Chem.* **2019**, *91*, 11916–11922.

[21] Yan, X.; Sokol, E.; Li, X.; Li, G.; Xu, S.; Cooks, R. G. *Angew. Chem.* **2014**, *53*, 5931–5935.

[22] Foley, D. A.; Wang, J.; Maranzano, B.; Zell, M. T.; Marquez, B. L.; Xiang, Y.; Reid, G. L. *Anal. Chem.* **2013**, *85*, 8928–8932.

[23] Daponte, J. A.; Guo, Y.; Ruck, R. T.; Hein, J. E. *ACS Catal.* **2019**, *9*, 11484–11491.

[24] Ray, A.; Bristow, T.; Whitmore, C.; Mosely, J. *Mass Spectrom. Rev.* **2018**, *37*, 565–579.

[25] McMaster, M. *LC/MS: A Practical User's Guide*; John Wiley & Sons: Hoboken, 2005.

[26] Boyd, B.; Boyd, R.; Basic, C.; Bethem, R. *Trace Quantitative Analysis by Mass Spectrometry*; John Wiley & Sons: Chichester, 2008.

[27] Santos, L. S. *European J. Org. Chem.* **2008**, *2008*, 235–253.

[28] Santos, L. S. *Reactive Intermediates: MS Investigations in Solution*; Wiley-VCH: Weinheim, 2010.

[29] Johnson, K. L.; Veenstra, T. D.; Londowski, J. M.; Tomlinson, A. J.; Kumar, R.; Naylor, S. *Biomed. Chromatogr.* **1999**, *13*, 37–45.

[30] Orton, D. J.; Tfaily, M. M.; Moore, R. J.; LaMarche, B. L.; Zheng, X.; Fillmore, T. L.; Chu, R. K.; Weitz, K. K.; Monroe, M. E.; Kelly, R. T.; Smith, R. D.; Baker, E. S. *Anal. Chem.* **2018**, *90*, 737–744.

[31] Bjarnason, A.; Desenfants, R. E.; Barr, M. E.; Dahl ', L. F. *Organometallics* **1990**, *9*, 657–661.

[32] Stoddard, R. L.; Collins, S.; Mcindoe, J. S. In *PATAI's Chem. Funct. Groups*; Rappoport, Z., Ed.; 2016; pp 1–15.

[33] Penafiel, J.; Hesketh, A. V.; Granot, O.; McIndoe, J. S. *Dalt. Trans.* **2016**, *45*.

[34] Eelman, M.; Blacquiere, J.; Moriarty, M.; Fogg, D. *Angew. Chemie Int. Ed.* **2008**, *47*, 303–306.

[35] Lubben, A. T.; McIndoe, J.; Weller, A. *Organometallics* **2008**, *27*, 3303–3306.

[36] Vikse, K. L.; Woods, M. P.; McIndoe, J. S. *Organometallics* **2010**, *29*, 6615.

[37] Errington, R. J. *Advanced practical inorganic and metalorganic chemistry*; Chapman & Hall: London, 1997.

[38] Vikse, K. L.; Ahmadi, Z.; McIndoe, J. *Coord. Chem. Rev.* **2014**, *279*, 96–114.

[39] Vikse, K. L.; Ahmadi, Z.; Manning, C. C.; Harrington, D. A.; McIndoe, J. S. *Angew. Chemie* **2011**, *123*, 8454–8456.

[40] Zhu, H.; Janusson, E.; Luo, J.; Piers, J.; Islam, F.; Mcgarvey, G. B.; Oliver, A. G.; Granot, O.; McIndoe, J. S. *Analyst* **2017**, *142*, 3728–3284.

[41] Gellrich, U.; Meißner, A.; Steffani, A.; Kähny, M.; Drexler, H. J.; Heller, D.; Plattner, D. A.; Breit, B. *J. Am. Chem. Soc.* **2014**, *136*, 1097–1104.

[42] Omari, I.; Randhawa, P.; Randhawa, J.; Yu, J.; McIndoe, J. S. *J. Am. Soc. Mass Spectrom.* **2019**, *30*, 1750–1757.

[43] Henderson, W.; Evans, C. *Inorganica Chim. Acta* **1999**, *294*, 183–192.

[44] Santos, L. S.; Rosso, G. B.; Pilli, R. A.; Eberlin, M. N. *J. Org. Chem.* **2007**, *72*, 5809–5812.

[45] Farrer, N. J.; McDonald, R.; McIndoe, J. S. *Dalt. Trans.* **2006**, 4570–4579.

[46] Farrer, N. J.; McDonald, R.; Piga, T.; McIndoe, J. S. *Polyhedron* **2010**, *29*, 254–261.

[47] Henderson, W.; Nicholson, B. K. *J. Chem. Soc. Chem. Commun.* **1995**, 2531–2532.

[48] Decker, C.; Henderson, W.; Nicholson, B. K. *J. Chem. Soc., Dalt. Trans.,* **1999**, 3507–3513.

[49] Hinderling, C.; Adlhart, C.; Chen, P. *Angew. Chemie Int. Ed.* **1998**, *37*, 2685–2689.

[50] Chisholm, D. M.; Oliver, A. G.; McIndoe, J. S. *Dalt. Trans.* **2010**, *39*, 364–373.

[51] Adlhart, C.; Chen, P. *Helv. Chim. Acta* **2000**, *83*, 2192–2196.

[52] Crawford, E.; Lohr, T.; Leitao, E. M.; Kwok, S.; McIndoe, J. S. *Dalt. Trans.* **2009**, 9110–9112.

[53] Mesias-Salazar, A.; Trofymchuk, O. S.; Daniliuc, C. G.; Antiñolo, A.; Carrillo-Hermosilla, F.; Nachtigall, F. M.; Santos, L. S.; Rojas, R. S. *J. Catal.* **2020**, *382*, 150–154.

[54] Kumar, M.; Verma, S.; Kumar, A.; Mishra, P. K.; Ramabhadran, R. O.; Banerjee, S.; Verma, A. K. *Chem. Commun.* **2019**, *55*, 9359–9362.

[55] Henderson, M. A.; McIndoe, J. S. *Chem. Commun.* **2006**, 2872–2874.

[56] Hesketh, A. V.; Nowicki, S.; Baxter, K.; Stoddard, R. L.; McIndoe, J. S. *Organometallics* **2015**, *34*, 3816–3819.

[57] Theron, R.; Wu, Y.; Yunker, L. P. E.; Hesketh, A. V.; Pernik, I.; Weller, A. S.; McIndoe, J. **2016**,

[58] Cheng, G.-J.; Zhong, X.-M.; Wu, Y.-D.; Zhang, X. *Chem. Commun.* **2019**, *55*, 12749–12764.

[59] Kostyukovich, A. Y.; Tsedilin, A. M.; Sushchenko, E. D.; Eremin, D. B.; Kashin, A. S.; Topchiy, M. A.; Asachenko, A. F.; Nechaev, M. S.; Ananikov, V. P. *Inorg. Chem. Front.* **2019**, *6*, 482–492.

[60] Sutera, S. P.; Skalak, R. *Annu. Rev. Fluid Mech.* **1993**, *25*, 1–20.

[61] Vikse, K. L.; Ahmadi, Z.; Luo, J.; Van Der Wal, N.; Daze, K.; Taylor, N.; McIndoe, J. S. *Int. J. Mass Spectrom.* **2012**, *323*, 8–13.

[62] Gross, J. *Mass Spectrometry*, 3rd ed.; Springer International Publishing: Cham, 2017.

[63] McLuckey, S. A.; Wells, J. M. *Chem. Rev.* **2001**, *101*, 571–606.

[64] Guilhaus, M.; Selby, D.; Mlynski, V. *Mass Spectrom. Rev.* **2000**, *19*, 65–107.

[65] Chernushevich, I. V.; Loboda, A. V.; Thomson, B. A. *J. Mass Spectrom.* **2001**, *36*, 849–865.

[66] Burlingame, A. L.; Boyd, R. K.; Gaskell, S. J. *Anal. Chem.* **1994**, *66*, 634–683.

[67] Thomas, G. T.; Janusson, E.; Zijlstra, H. S.; McIndoe, J. S. *Chem. Commun.* **2019**, *55*, 11727–11730.

[68] Thomas, G. T.; MacGillivray, L.; Dean, N. L.; Stoddard, R. L.; Yunker, L. P.; McIndoe, J. S. *Int. J. Mass Spectrom.* **2019**, *441*, 14–18.

[69] Yunker, L. P.; Donnecke, S.; Ting, M.; Yeung, D.; McIndoe, J. S. *J. Chem. Inf. Model.* **2019**, *59*, 1295–1300.

[70] Bilbao, A.; Gibbons, B. C.; Slysz, G. W.; Crowell, K. L.; Monroe, M. E.; Ibrahim, Y. M.; Smith, R. D.; Payne, S. H.; Baker, E. S. *Int. J. Mass Spectrom.* **2018**, *427*, 91–99.

[71] Wei, A. A. J.; Joshi, A.; Chen, Y.; McIndoe, J. S. *Int. J. Mass Spectrom.* **2020**, *450*, 116306.

[72] Janusson, E.; Hesketh, A. V.; Bamford, K. L.; Hatlelid, K.; Higgins, R.; McIndoe, J. S. *Int. J. Mass Spectrom.* **2015**, *388*, 1–8.

[73] Nekkanti, S.; Kumar, N. P.; Sharma, P.; Kamal, A.; Nachtigall, F. M.; Forero-Doria, O.; Santos, L. S.; Shankaraiah, N. *RSC Adv.* **2016**, *6*, 2671–2677.

[74] Michaudel, Q.; Thevenet, D.; Baran, P. S. *J. Am. Chem. Soc.* **2012**, *134*, 2547–2550.

[75] Sathyamoorthi, S.; Lai, Y. H.; Bain, R. M.; Zare, R. N. *J. Org. Chem.* **2018**, *83*, 5681–5687.

[76] Vicent, C.; Gusev, D. G. *ACS Catal.* **2016**, *6*, 3301–3309.

[77] Pedrajas, E.; Sorribes, I.; Junge, K.; Beller, M.; Llusar, R. *ChemCatChem* **2015**, *7*, 2675–2681.

[78] Ahmadi, Z.; Yunker, L. P. E.; Oliver, A. G.; McIndoe, J. S. *Dalt. Trans.* **2015**, *44*, 20367–20375.

[79] Johnson, H. C.; Torry-Harris, R.; Ortega, L.; Theron, R.; McIndoe, J. S.; Weller, A. S. *Catal. Sci. Technol.* **2014**, *4*, 3486–3494.

[80] Ahmadi, Z.; Oliver, A. G.; McIndoe, J. S. *Chempluschem* **2013**, *78*, 632–635.

[81] Sorribes, I.; Wienhöfer, G.; Vicent, C.; Junge, K.; Llusar, R.; Beller, M. *Angew. Chemie* **2012**, *124*, 7914–7918.

[82] Ringger, D. H.; Kobylianskii, I. J.; Serra, D.; Chen, P. **2014**, *20*, 14270–14281.

[83] Luo, J.; Oliver, A. G.; McIndoe, J. *Dalt. Trans.* **2013**, *42*, 11312.

[84] Ahmadi, Z.; McIndoe, J. S. *Chem. Commun.* **2013**, *49*, 11488.

[85] Mack, J. B.; Walker, K. L.; Robinson, S. G.; Zare, R. N.; Sigman, M. S.; Waymouth, R. M.; Du Bois, J. *J. Am. Chem. Soc.* **2019**, *141*, 972–980.

[86] Yunker, L. P. E.; Ahmadi, Z.; Logan, J. R.; Wu, W.; Li, T.; Martindale, A.; Oliver, A. G.; McIndoe, J. S. *Organometallics* **2018**, *37*, 4297–4308.

[87] Henderson, M.; Luo, J.; Oliver, A.; Mcindoe, J. S. *Organometallics* **2011**, *30*, 5471–5479.

[88] Hua, X.; Masson-Makdissi, J.; Sullivan, R. J.; Newman, S. G. *Org. Lett.* **2016**, *18*, 5312–5315.

[89] Fier, P. S.; Luo, J.; Hartwig, J. F. *J. Am. Chem. Soc.* **2013**, *135*, 2552–2559.

[90] Ingram, A. J.; Walker, K. L.; Zare, R. N.; Waymouth, R. M. *J. Am. Chem. Soc.* **2015**, *137*, 13632–13646.

[91] Kolter, M.; Koszinowski, K. *Chem. – A Eur. J.* **2019**, *25*, 13376–13384.

[92] Belli, R. G.; Wu, Y.; Ji, H.; Joshi, A.; Yunker, L. P.; McIndoe, J. S.; Rosenberg, L. *Inorg. Chem.* **2019**, *58*, 747–755.

[93] Yeung, D.; Penafiel, J.; Zijlstra, H. S.; McIndoe, J. S. *Inorg. Chem.* **2018**, *57*, 457–461.

[94] Joshi, A.; Zijlstra, H. S.; Collins, S.; McIndoe, J. S. *ACS Catal.* **2020**, *10*, 7195–7206.

[95] Iacobucci, C.; Reale, S.; De Angelis, F. *Angew. Chemie Int. Ed.* **2016**, *55*, 2980–2993.

[96] Grimaldi, J.; Baldo, J.; McMurray, C.; Sykes, B. D. *J. Am. Chem. Soc.* **1972**, *94*, 7641–7645.

[97] Grimaldi, J. J.; Sykes, B. D. *Rev. Sci. Instrum.* **1975**, *46*, 1201.

[98] Kühne, R. O.; Schaffhauser, T.; Wokaun, A.; Ernst, R. R. *J. Magn. Reson.* **1979**, *35*, 39–67.

[99] Funahashi, S.; Ishihara, K.; Aizawa, S.; Sugata, T.; Ishii, M.; Inada, Y.; Tanaka, M. *Rev. Sci. Instrum.* **1998**, *64*, 130.

[100] Yushmanov, P. V.; Furó, I. *J. Magn. Reson.* **2005**, *175*, 264–270.

[101] Dunn, A. L.; Landis, C. R. *Magn. Reson. Chem.* **2017**, *55*, 329–336.

[102] von Harbou, E.; Behrens, R.; Berje, J.; Brächer, A.; Hasse, H. *Chemie Ing. Tech.* **2017**, *89*, 369–378.

[103] Scheithauer, A.; Brächer, A.; Grützner, T.; Zollinger, D.; Thiel, W. R.; von Harbou, E.; Hasse, H. *Ind. Eng. Chem. Res.* **2014**, *53*, 17589–17596.

[104] Johnston, C. P.; West, T. H.; Dooley, R. E.; Reid, M.; Jones, A. B.; King, E. J.; Leach, A. G.; Lloyd-Jones, G. C. *J. Am. Chem. Soc.* **2018**, *140*, 11112–11124.

[105] García-Domínguez, A.; West, T. H.; Primozic, J. J.; Grant, K. M.; Johnston, C. P.; Cumming, G. G.; Leach, A. G.; Lloyd-Jones, G. C. *J. Am. Chem. Soc.* **2020**, *142*, 14649–14663.

[106] García-Domínguez, A.; Helou De Oliveira, P. H.; Thomas, G. T.; Sugranyes, A. R.; Lloyd-Jones, G. C. *ACS Catal.* **2021**, *11*, 3017–3025.

[107] Kashin, A. S.; Degtyareva, E. S.; Eremin, D. B.; Ananikov, V. P. *Nat. Commun.* **2018**, *9*, 2936.

[108] Banerjee, S.; Sathyamoorthi, S.; Du Bois, J.; Zare, R. N. *Chem. Sci.* **2017**, *8*, 7003–7008.

[109] Ahmadi, Z.; McIndoe, J. S. *Chem. Commun.* **2013**, *49*, 11488–11490.

[110] Stoddard, R. L.; Luo, J.; van der Wal, N.; O'Rourke, N. F.; Wulff, J. E.; McIndoe, J. S. *New J. Chem.* **2014**, *38*, 5382–5390.

[111] Pike, S. D.; Pernik, I.; Theron, R.; McIndoe, J. S.; Weller, A. S. *J. Organomet. Chem.* **2015**, *784*, 75–83.

[112] Janusson, E.; Zijlstra, H. S.; Nguyen, P. P. T.; Macgillivray, L.; Martelino, J.; Mcindoe, J. S. *Chem. Commun* **2017**, *854*, 854–856.

[113] Dean, N. L.; McIndoe, J. S. *Can. J. Chem.* **2018**, *96*, 587–590.

[114] Nnaji, C. N.; Mach, P. M.; Acheampong, J. S.; Falconer, T. M.; Verbeck, G. F. *Anal. Methods* **2016**, *8*, 4798–4807.

[115] March, R. E.; Stairs, R. A.; Stock, N. L. *Int. J. Mass Spectrom.* **2017**, *415*, 18–28.

[116] Kapp, T.; Vetter, W. *Anal. Chem.* **2006**, *78*, 8156–8161.

[117] Ulanowska, A.; Ligor, T.; Amann, A.; Buszewski, B. *J. Chromatogr. Sci.* **2012**, *50*, 10–4.

[118] Zhang, X. K.; Dutky, R. C.; Fales, H. M. *Anal. Chem.* **1996**, *68*, 3288–3289.

[119] Ende, M.; Spiteller, G. *Mass Spectrom. Rev.* **1982**, *1*, 29–62.

[120] Wanasundara, P.; Shahidi, F. In *Bailey's Ind. Oil Fat Prod.*, 6th ed.; Shahidi, F., Ed.; John Wiley & Sons: New York, 2005; pp 436–447.

[121] Craft, B. D.; Kerrihard, A. L.; Amarowicz, R.; Pegg, R. B. *Compr. Rev. Food Sci. Food Saf.* **2012**, *11*, 148–173.

[122] Wright, J.; Johnson, E.; DiLabio, G. A. *J. Am. Chem. Soc.* **2001**, *123*, 1173–1183.

[123] Klein, E.; Lukes, V.; Cibulkova, Z. *Pet. Coal* **2005**, *47*, 33–39.

[124] Kriston, I. Some aspects of the degradation and stabilization of Phillips type polyethylene. Ph.D. thesis, Budapest University of Technology and Economics, 2010.

[125] Spacht, R. B.; Wadelin, C. W.; Hollingshead, W. S.; Wills, D. C. *Ind. Eng. Chem. Prod. Res. Dev.* **1962**, *1*, 202–205.

[126] Hollingshead, W. Butylated, α-methyl styrenated phenolic antioxidants for polymers. 1975; https://patents.google.com/patent/US3989665.

[127] Lutz, J. T. *Thermoplastic polymer additives: Theory and Practice*; M. Dekker, 1989.

[128] Ash, M.; Ash, I. *Handbook of Preservatives*; Synapse Information Resources: Endicott, 2009.

[129] Sadequl, A.; Ishiaku, U.; Ismail, H.; Poh, B. *Eur. Polym. J.* **1998**, *34*, 51–57.

[130] Naccarato, A.; Gionfriddo, E.; Sindona, G.; Tagarelli, A. *J. Chromatogr. A* **2014**, *1338*, 164–173.

[131] Kloepfer, A.; Jekel, M.; Reemtsma, T. *Environ. Sci. Technol.* **2005**, *39*, 3792–3798.

[132] Linssen, J. P. H.; Rijnen, L.; Legger-Huiysman, A.; Roozen, J. P. *Food Addit. Contam.* **1998**, *15*, 79–83.

[133] Bellavia, V.; Natangelo, M.; Fanelli, R.; Rotilio, D. *J. Agric. Food Chem.* **2000**, *48*, 1239–1242.

[134] Akiba, M.; Hashim, A. *Prog. Polym. Sci.* **1997**, *22*, 475–521.

[135] Patiny, L.; Borel, A. *J. Chem. Inf. Model.* **2013**, *53*, 1223–1228.

[136] Honarvar, E.; Venter, A. R. *J. Am. Soc. Mass Spectrom.* **2018**, *29*, 2443–2455.

[137] Surry, D. S.; Buchwald, S. L. *Chem. Sci.* **2011**, *2*, 27–50.

[138] Christensen, H.; Kiil, S.; Dam-Johansen, K.; Nielsen, O.; Sommer, M. B. *Org. Process Res. Dev.* **2006**, *10*, 762–769.

[139] Fairlamb, I. J. S.; Kapdi, A. R.; Lee, A. F.; McGlacken, G. P.; Weissburger, F.; de Vries, A. H. M.; Schmieder-van de Vondervoort, L. *Chem. Eur. J.* **2006**, *12*, 8750–8761.

[140] Ingoglia, B. T.; Wagen, C. C.; Buchwald, S. L. *Tetrahedron* **2019**, In Press.

[141] Ruiz-Castillo, P.; Buchwald, S. L. *Chem. Rev.* **2016**, *116*, 12564–12649.

[142] Gangjee, A.; Namjoshi, O. A.; Raghavan, S.; Queener, S. F.; Kisliuk, R. L.; Cody, V. *J. Med. Chem.* **2013**, *56*, 4422–41.

[143] Wang, L.; Neumann, H.; Spannenberg, A.; Beller, M. *Chem. Eur. J.* **2018**, *24*, 2164–2172.

[144] Guram, A. S. *Org. Process Res. Dev.* **2016**, *20*, 1754–1764.

[145] Valente, C.; Pompeo, M.; Sayah, M.; Organ, M. G. *Org. Process Res. Dev.* **2014**, *18*, 180–190.

[146] Wiethan, C.; Rosa, W. C.; Bonacorso, H. G.; Stradiotto, M. *Org. Biomol. Chem.* **2016**, *14*, 2352–2359.

[147] MacLean, M. A.; Diez-Cecilia, E.; Lavery, C. B.; Reed, M. A.; Wang, Y.; Weaver, D. F.; Stradiotto, M. *Bioorg. Med. Chem. Lett.* **2016**, *26*, 100–104.

[148] Nandi, D.; Islam, R. U.; Devi, N.; Siwal, S.; Mallick, K. *New J. Chem.* **2018**, *42*, 812–816.

[149] Lombardi, C.; Day, J.; Chandrasoma, N.; Mitchell, D.; Rodriguez, M. J.; Farmer, J. L.; Organ, M. G. *Organometallics* **2017**, *36*, 251–254.

[150] Gildner, P. G.; DeAngelis, A.; Colacot, T. J. *Org. Lett.* **2016**, *18*, 1442–1445.

[151] Hoi, K. H.; Çalimsiz, S.; Froese, R. D. J.; Hopkinson, A. C.; Organ, M. G. *Chem. Eur. J.* **2012**, *18*, 145–151.

[152] Sunesson, Y.; Limé, E.; Nilsson Lill, S. O.; Meadows, R. E.; Norrby, P.-O. *J. Org. Chem.* **2014**, *79*, 11961–11969.

[153] Driver, M. S.; Hartwig, J. F. *J. Am. Chem. Soc.* **1997**, *119*, 8232–8245.

[154] Widenhoefer, R.; Buchwald, S. *Organometallics* **1996**, *15*, 2755–2763.

[155] Driver, M. S.; Hartwig, J. F. *J. Am. Chem. Soc.* **1995**, *117*, 4708–4709.

[156] Hartwig, J.; Richards, S.; Barañano, D.; Frédéric, P. *J. Am. Chem. Soc.* **1996**, *118*, 3626–3633.

[157] Guram, A. S.; Rennels, R. A.; Buchwald, S. L. *Angew. Chemie* **1995**, *34*, 1348–1350.

[158] Louie, J.; Hartwig, J. F. *Tetrahedron Lett.* **1995**, *36*, 3609–3612.

[159] Guram, A. S.; Buchwald, S. L. *J. Am. Chem. Soc.* **1994**, *116*, 7901–7902.

[160] Paul, F.; Patt, J.; Hartwig, J. F. *J. Am. Chem. Soc.* **1994**, *116*, 5969–5970.

[161] Louie, J.; Frédéric, P.; Hartwig, J. *Organometallics* **1996**, *15*, 2794–2805.

[162] Vinogradova, E. V.; Fors, B. P.; Buchwald, S. L. *J. Am. Chem. Soc* **2012**, *134*, 11132–11135.

[163] Fors, B. P.; Davis, N. R.; Buchwald, S. L. *J. Am. Chem. Soc.* **2009**, *131*, 5766–5768.

[164] Anderson, K. W.; Buchwald, S. L. *Angew. Chem.* **2005**, *44*, 6173–6177.

[165] Vikse, K. L.; Henderson, M. A.; Oliver, A. G.; McIndoe, J. S. *Chem. Commun.* **2010**, *46*, 7412.

[166] Chisholm, D. M.; McIndoe, J. S. *Dalt. Trans.* **2008**, 3933–3945.

[167] Urgaonkar, S.; Verkade, J. G. *J. Org. Chem.* **2004**, *69*, 9135–9142.

[168] Domon, B.; Aebersold, R. *Science (80-.).* **2006**, *312*, 212–217.

[169] Carr, S. A.; Anderson, L. *Clin. Chem.* **2008**, *54*, 1749–52.

[170] Norris, A.; Whitelegge, J.; Faull, K.; Toyokuni, T. *Biochemistry* **2001**, *40*, 3774–3779.

[171] Norris, A.; Whitelegge, J.; Faull, K.; Toyokuni, T. *Anal. Chem.* **2001**, *73*, 6024–6029.

[172] Wang, Y.; Lin, W.-Y.; Liu, K.; Lin, R. J.; Selke, M.; Kolb, H. C.; Zhang, N.; Zhao, X.-Z.; Phelps, M. E.; Shen, C. K. F.; Faull, K. F.; Tseng, H.-R. *Lab Chip* **2009**, *9*, 2281–2285.

[173] Šojić, D. V.; Anderluh, V. B.; Orčić, D. Z.; Abramović, B. F. *J. Hazard. Mater.* **2009**, *168*, 94–101.

[174] Qiao, J.-P.; Sun, X.-T.; Zhu, L. *Rapid Commun. Mass Spectrom.* **2009**, *23*, 1264–1268.

[175] Zhuo, Q.; Deng, S.; Yang, B.; Huang, J.; Yu, G. *Environ. Sci. Technol* **2011**, *45*, 2973–2979.

[176] Lam, M. W.; Young, C. J.; Mabury, S. A. *Environ. Sci. Technol.* **2005**, *39*, 513–522.

[177] Janusson, E.; Zijlstra, H. S.; Nguyen, P. P. T.; MacGillivray, L.; Martelino, J.; McIndoe, J. *Chem. Commun.* **2017**, *53*, 854–856.

[178] Repeated washing with acid was required to reduce aniline contamination to the levels shown. At a catalyst loading of 0.1%, observing aniline binding suggested a contamination level of approx. 0.1% (ppm).

[179] Barder, T.; Walker, S.; Martinelli, J.; Buchwald, S. L. *J. Am. Chem. Soc.* **2005**, *127*, 4685–4696.

[180] Weber, P.; Biafora, A.; Doppiu, A.; Bongard, H.-J.; Kelm, H.; Gooßen, L. J. *Org. Process Res. Dev.* **2019**,

[181] Dennis, J. M.; White, N. A.; Liu, R. Y.; Buchwald, S. L. *J. Am. Chem. Soc.* **2018**, *140*, 4721–4725.

[182] Dennis, J. M.; White, N. A.; Liu, R. Y.; Buchwald, S. L. *ACS Catal.* **2019**, *9*, 3822–3830.

[183] Arrechea, P. L.; Buchwald, S. L. *J. Am. Chem. Soc.* **2016**, *138*, 12486–12493.

[184] McFarlane, J.; Henderson, B.; Donnecke, S.; McIndoe, J. *Organometallics* **2019**, *38*, 4051–4053.

[185] Weber, W. *Silicon Reagents for Organic Synthesis*; Springer-Verlag: Berlin, 1983.

[186] Bennetau, B.; Rajarison, F.; Dunoguès, J.; Babin, P. *Tetrahedron* **1993**, *49*, 10843–10854.

[187] Tamao, K.; Ishida, N.; Tanaka, T.; Kumada, M. *Organometallics* **1983**, *2*, 1694–1696.

[188] Jones, G. R.; Landais, Y. *Tetrahedron* **1996**, *52*, 7599–7662.

[189] Hatanaka, Y.; Hiyama, T. *J. Org. Chem.* **1988**, *53*, 918–920.

[190] Hatanaka, Y.; Hiyama, T. *Tetrahedron Lett.* **1990**, *31*, 2719–2722.

[191] Nozawa-Kumada, K.; Osawa, S.; Sasaki, M.; Chataigner, I.; Shigeno, M.; Kondo, Y. *J. Org. Chem.* **2017**, *82*, 9487–9496.

[192] Denmark, S. E.; Kallemeyn, J. M. *Org. Lett.* **2003**, *5*, 3483–3486.

[193] Yamanoi, Y. *J. Org. Chem.* **2005**, *70*, 9607–9609.

[194] Hamze, A.; Provot, O.; Alami, M.; Brion, J. D. *Org. Lett.* **2006**, *8*, 931–934.

[195] Yamanoi, Y.; Nishihara, H. *Tetrahedron Lett.* **2006**, *47*, 7157–7161.

[196] McNeill, E.; Barder, T. E.; Buchwald, S. L. *Org. Lett.* **2007**, *9*, 3785–3788.

[197] Yamanoi, Y.; Nishihara, H. *J. Org. Chem.* **2008**, *73*, 6671–6678.

[198] Iizuka, M.; Kondo, Y. *European J. Org. Chem.* **2008**, *2008*, 1161–1163.

[199] Dilman, A. In *Mod. Synth. Process. React. Fluorinated Compd. Prog. Fluorince. Sci. Ser.*; Groult, H., Leroux, F. R., Tressaud, A., Eds.; Elsevier: Amsterdam, 2017; pp 181–199.

[200] Beier, P.; Zibinsky, M.; Prakash, S. G. K. *Org. React.* **2016**, *91*, 1–492.

[201] Hryshchuk, O. V.; Varenyk, A. O.; Yurov, Y.; Kuchkovska, Y. O.; Tymtsunik, A. V.; Grygorenko, O. O. *Eur. J. Org. Chem.* **2020**, *2020*, 2217–2224.

[202] Wang, F.; Luo, T.; Hu, J.; Wang, Y.; Krishnan, H. S.; Jog, P. V.; Ganesh, S. K.; Prakash, G. K.; Olah, G. A. *Angew. Chem. Int. Ed.* **2011**, *50*, 7153–7157.

[203] Nosik, P. S.; Poturai, A. S.; Pashko, M. O.; Melnykov, K. P.; Ryabukhin, S. V.; Volochnyuk, D. M.; Grygorenko, O. O. *Eur. J. Org. Chem.* **2019**, *2019*, 4311–4319.

[204] Nosik, P. S.; Ryabukhin, S. V.; Grygorenko, O. O.; Volochnyuk, D. M. *Adv. Synth. Catal.* **2018**, *360*, 4104–4114.

[205] Bychek, R. M.; Levterov, V. V.; Sadkova, I. V.; Tolmachev, A. A.; Mykhailiuk, P. K. *Chem. – Eur. J.* **2018**, *24*, 12291–12297.

[206] Kolomeitsev, A.; Movchun, V.; Rusanov, E.; Bissky, G.; Lork, E.; Röschenthaler, G.-V.; Kirsch, P. *Chem. Commun.* **1999**, 1017–1018.

[207] Maggiarosa, N.; Tyrra, W.; Naumann, D.; Kirij, N. V.; Yagupolskii, Y. L. *Angew. Chem. Int. Ed.* **1999**, *38*, 2252–2253.

[208] Dilman, A. D.; Levin, V. V.; Zelinsky, N. D. *Acc. Chem. Res* **2018**, *51*, 1272–1280.

[209] Campos, K. R.; Coleman, P. J.; Alvarez, J. C.; Dreher, S. D.; Garbaccio, R. M.; Terrett, N. K.; Tillyer, R. D.; Truppo, M. D.; Parmee, E. R. *Science (80-.).* **2019**, *363*.

[210] Bzeih, T.; Naret, T.; Hachem, A.; Jaber, N.; Khalaf, A.; Bignon, J.; Brion, J.-D.; Alami, M.; Hamze, A. *Chem. Commun.* **2016**, *52*, 13027–13030.

[211] Bzeih, T.; Zhang, K.; Khalaf, A.; Hachem, A.; Alami, M.; Hamze, A. *J. Org. Chem.* **2019**, *84*, 228–238.

[212] Touré, B. B.; Hall, D. G. *Chem. Rev.* **2009**, *109*, 4439–4486.

[213] Cox, J. B.; Kimishima, A.; Wood, J. L. *J. Am. Chem. Soc.* **2019**, *141*, 25–28.

[214] Zhu, X.; McAtee, C. C.; Schindler, C. S. *J. Am. Chem. Soc.* **2019**, *141*, 3409–3413.

[215] He, C.; Stratton, T. P.; Baran, P. S. *J. Am. Chem. Soc.* **2019**, *141*, 29–32.

[216] Barroso, R.; Valencia, R. A.; Cabal, M.-P.; Valdés, C. V. *Org. Lett.* **2014**, *16*, 2264–2267.

[217] Johansson Seechurn, C.; Carin, C.; Kitching, M. O.; Colacot, T. J.; Snieckus, V. *Angew. Chem.* **2012**, *51*, 5062–5085.

[218] Negishi, E., Ed. *Handbook of Organopalladium Chemistry for Organic Synthesis*; Wiley: New York, 2002.

[219] Kumada, M. *Pure Appl. Chem.* **1980**, *52*, 669–679.

[220] Tsuji, J. *Palladium Reagents and Catalysts*; Wiley: Chichester, 2004.

[221] Li, H.; Johansson Seechurn, C.; Colacot, T. *ACS Cat.* **2012**, *2*, 1147–1164.

[222] Ming So, C.; Kwong, F. *Chem. Soc. Rev.* **2011**, *40*, 4963–4972.

[223] Fortman, G.; Nolan, S. *Chem. Soc. Rev.* **2011**, *40*, 5151–5169.

[224] Sellars, J.; Steel, P. *Chem. Soc. Rev.* **2011**, *40*, 5170–5180.

[225] Jana, R.; Pathak, T.; Sigman, M. *Chem. Rev.* **2011**, *111*, 1417–1492.

[226] Echavarren, A. *ChemCatChem* **2010**, *2*, 1331–1332.

[227] Barluenga, J.; Moriel, P.; Valdés, C.; Aznar, F. *Angew. Chem.* **2007**, *46*, 5587–5590.

[228] Xiao, Q.; Ma, J.; Yang, Y.; Zhang, Y.; Wang, J. *Org. Lett.* **2009**, *11*, 4732–4735.

[229] Barluenga, J.; Florentino, L.; Aznar, F.; Valdés, C. *Org. Lett.* **2011**, *13*, 510–513.

[230] Barluenga, J.; Tomás-Gamasa, M.; Aznar, F.; Valdés, C. *Adv. Synth. Catal.* **2010**, *352*, 3235–3240.

[231] Barluenga, J.; Tomás-Gamasa, M.; Moriel, P.; Aznar, F.; Valdés, C. *Chem. - A Eur. J.* **2008**, *14*, 4792–4795.

[232] Shao, Z.; Zhang, H. *Chem. Soc. Rev.* **2012**, *41*, 560–572.

[233] Aziz, J.; Brachet, E.; Hamze, A.; Peyrat, J.-F.; Bernadat, G.; Morvan, E.; Bignon, J.; Wdzieczak-Bakala, J.; Desravines, D.; Dubois, J.; Tueni, M.; Yassine, A.; Brion, J.-D.; Alami, M. *Org. Biomol. Chem.* **2013**, *11*, 430–442.

[234] Timmerman, J. C.; Sims, N. J.; Wood, J. L. *J. Am. Chem. Soc.* **2019**, *141*, 10082–10090.

[235] Aziz, J.; Brion, J.-D.; Alami, M.; Hamze, A. *RSC Adv.* **2015**, *5*, 74391–74398.

[236] Zhou, Q.; Gao, Y.; Xiao, Y.; Yu, L.; Fu, Z.; Li, Z.; Wang, J. *Polym. Chem* **2019**, *10*, 569–573.

[237] Ping, W.-W.; Jin, L.; Wu, Y.; Xue, X.-Y.; Zhao, X. *Tetrahedron* **2014**, *70*, 9373–9380.

[238] Sullivan, R. J.; Freure, G. P. R.; Newman, S. G. *ACS Catal.* **2019**, *9*, 5623–5630.

[239] Nanalysis Corp, NMReady-60PRO. https://www.nanalysis.com/nmready-60pro.

[240] Maschmeyer, T.; Prieto, P. L.; Grunert, S.; Hein, J. E. *Magn. Reson. Chem.* **2020**, *58*, 1234–1248.

[241] Giberson, J.; Scicluna, J.; Legge, N.; Longstaffe, J. In *Annu. Reports NMR Spectrosc.*; Webb, G. A., Ed.; Elsevier Ltd.: London, 2021; Vol. 102; pp 153–246.

[242] Tan, H.; Houpis, I.; Liu, R.; Wang, Y.; Chen, Z. *Org. Lett.* **2015**, *17*, 3548–3551.

[243] Hansch, C.; Leo, A.; Taft, R. *Chem. Rev.* **1991**, *91*, 165–195.

[244] Lu, J.; Donnecke, S.; Paci, I.; Leitch, D. *ChemRxiv* **2021**,

[245] Zhao, X.; Jing, J.; Lu, K.; Zhang, Y.; Wang, J. *Chem. Commun.* **2010**, *46*, 1724.

[246] Miller, V. P.; Yang, D. Y.; Weigel, T. M.; Han, O.; Liu, H. W. *J. Org. Chem.* **2002**, *54*, 4175–4188.

[247] Wentrup, C. *Angew. Chemie Int. Ed.* **2020**,

[248] Zeise, W. C. *Ann. der Phys. und Chemie* **1831**, *97*, 497–541.

[249] Hunt, L. *Platin. Met. Rev.* **1984**, *28*, 76–83.

[250] Love, R. A.; Koetzle, T. F.; B Williams, G. J.; Andrews, L. C.; Bau, R. *Inorg. Chem.* **1975**, *14*, 2653–2657.

[251] Black, M.; Mais, R. H. B.; Owston, P. G. *Acta Cryst.* **1969**, *25*, 1753–1759.

[252] Dewar, M. *Bull. Soc. Chim. Fr.* **1951**, C71.

[253] Dewar, M. *Bull. Soc. Chim. Fr.* **1951**, C79.

[254] Chatt, J.; Duncanson, L. A. *J. Chem. Soc.* **1953**, 2939–2947.

[255] Chatt, J.; Duncanson, L. A.; Venanzi, L. M. *J. Chem. Soc.* **1955**, 4456–4460.

[256] Albright, T. A.; Hoffmann, R.; Thorn, D. L. *J. Am. Chem. Soc.* **1979**, *101*, 3801–3812.

[257] Foulds, G. A.; Thornton, D. A. *J. Mol. Struct.* **1983**, *98*, 309–314.

[258] Kubota, M.; Parks, G. In *Inorg. Synth.*; Cowley, A. H., Ed.; Inorganic Syntheses; John Wiley & Sons, Inc.: Hoboken, NJ, USA, 1996; Vol. 31; pp 244–245.

[259] Meieranz, S.; Stefanopoulou, M.; Rubner, G.; Bensdorf, K.; Kubutat, D.; Sheldrick, W. S.; Gust, R. *Angew. Chemie Int. Ed.* **2015**, *54*, 2834–2837.

[260] Scherer, O. J.; Nahrstedt, A. *Angew. Chemie Int. Ed. English* **1979**, *18*, 234–235.

[261] Weninger, A.; Baecker, D.; Obermoser, V.; Egger, D.; Wurst, K.; Gust, R. *Int. J. Mol. Sci.* **2018**, *19*, 1612.

[262] Luo, J.; Wu, Y.; Zijlstra, H. S.; Harrington, D. A.; Mcindoe, J. S. *Catal. Sci. Technol* **2017**, *7*, 2609.

[263] Luo, H.; Wu, G.; Xu, S.; Wang, K.; Wu, C.; Zhang, Y.; Wang, J. *Chem. Commun.* **2015**, *51*, 13321–13323.

[264] Chock, P.; Halpern, J.; Paulik, F.; Shupack, S.; Deangelis, T. In *Inorg. Synth. Reagents Transit. Met. Complex Organomet. Synth. Vol. 28*; Angelici, R. J., Ed.; John Wiley & Sons, Inc., 1990; pp 349–351.

[265] Dub, P. A.; Rodriguez-Zubiri, M.; Daran, J.-C.; Brunet, J.-J.; Poli, R. *Organometallics* **2009**, *28*, 4764–4777.

[266] Hou, G.-L.; Govind, N.; Xantheas, S. S.; Wang, X.-B. *J. Phys. Chem. A* **2018**, *122*, 56.

[267] Harrison, D. E.; Taube, H. *J. Am. Chem. Soc.* **1967**, *89*, 5706–5707.

[268] Hidai, M.; Tominari, K.; Uchida, Y.; Misono, A. *J. Chem. Soc. D Chem. Commun.* **1969**, 1392.

[269] Bell, B.; Chatt, J.; Leigh, G. J. *J. Chem. Soc. D Chem. Commun.* **1970**, 842a–842a.

[270] Chatt, J. *Platin. Met. Rev.* **1969**, *13*, 9–14.

[271] Yamamoto, A.; Kitazume, S.; Pu, L. S.; Ikeda, S. *Chem. Commun.* **1967**, 79–80.

[272] Holland, P. L. *Dalt. Trans.* **2010**, *39*, 5415–5425.

[273] Bhutto, S. M.; Holland, P. L. *Eur. J. Inorg. Chem.* **2019**, *2019*, 1861–1869.

[274] Lu, E.; Atkinson, B. E.; Wooles, A. J.; Boronski, J. T.; Doyle, L. R.; Tuna, F.; Cryer, J. D.; Cobb, P. J.; Vitorica-Yrezabal, I. J.; Whitehead, G. F.; Kaltsoyannis, N.; Liddle, S. T. *Nat. Chem.* **2019**, *11*, 806–811.

[275] MacLachlan, E. A.; Fryzuk, M. D. Synthesis and reactivity of side-on-bound dinitrogen metal complexes. 2006.

[276] Sellmann, D. *Angew. Chemie Int. Ed. English* **1974**, *13*, 639–649.

[277] Evans, W. J.; Ulibarri, T. A.; Ziller, J. W. *J. Am. Chem. Soc.* **1988**, *110*, 6877–6879.

[278] Kozak, C. M.; Mountford, P. *Angew. Chemie Int. Ed.* **2004**, *43*, 1186–1189.

[279] Chatt, J.; Dilworth, J. R.; Richards, R. L. *Chem. Rev.* **1978**, *78*, 589–625.

[280] Bowman, A. C.; Milsmann, C.; Atienza, C. C. H.; Lobkovsky, E.; Wieghardt, K.; Chirik, P. J. *J. Am. Chem. Soc.* **2010**, *132*, 1676–1684.

[281] Burgess, B. K. *Chem. Rev.* **1990**, *90*, 1377–1406.

[282] Burgess, B. K.; Lowe, D. J. *Chem. Rev.* **1996**, *96*, 2983–3011.

[283] Simpson, F. B.; Burris, R. H. *Science (80-.).* **1984**, *224*, 1095–1097.

[284] Rutledge, H. L.; Tezcan, F. A. *Chem. Rev.* **2020**, *120*, 5158–5193.

[285] Rees, D. C.; Howard, J. B. Nitrogenase: Standing at the crossroads. 2000.

[286] Burdett, J. K.; Graham, M. A.; Turner, J. J. *J. Chem. Soc., Dalt. Trans.* **1972**, 1620–1625.

[287] Citra, A.; Wang, X.; Bare, W. D.; Andrews, L. *J. Phys. Chem. A* **2001**, *105*, 7799–7811.

[288] Kündig, E. P.; Moskovits, M.; Ozin, G. A. *Can. J. Chem.* **1973**, *51*, 2710–2721.

[289] Ozin, G. A.; Klotzbuecher, W. E. *J. Am. Chem. Soc.* **1975**, *97*, 3965–3974.

[290] Du, Y.; Zhang, N.; Cui, M.; Liu, Z.; Liu, S. *Rapid Commun. Mass Spectrom.* **2012**, *26*, 2832–2836.

[291] Feifan, X.; Pieter, C.; Jan, V. B. *J. Mass Spectrom.* **2017**, *52*, 434–441.

[292] Rijs, N. J.; Weiske, T.; Schlangen, M.; Schwarz, H. *Anal. Chem.* **2015**, *87*, 9769–9776.

[293] Lorenzo, J.; Delgado, A.; Montaña, Á. M.; Mesas, J. M.; Alegre, M. T.; Rodríguez, M. D. C.; Avilés, F. X. *Eur. J. Med. Chem.* **2014**, *83*, 374–388.

[294] Chalkley, M. J.; Drover, M. W.; Peter, J. C. *Chem. Rev.* **2020**, *120*, 5582–5636.

[295] Zocher, E.; Sigrist, R.; Chen, P. *Inorg. Chem.* **2007**, *46*, 11366–11370.

[296] Narancic, S.; Bach, A.; Chen, P. *J. Phys. Chem. A* **2007**, *111*, 7006–7013.

[297] Rodgers, M. T.; Armentrout, P. B. *Mass Spectrom. Rev.* **2000**, *19*, 215–247.

[298] Rodgers, M. T.; Ervin, K. M.; Armentrout, P. B. *J. Chem. Phys.* **1997**, *106*, 4499–4508.

[299] Wyttenbach, T.; Von Helden, G.; Batka, J. J.; Carlat, D.; Bowers, M. T. *J. Am. Soc. Mass Spectrom.* **1997**, *8*, 275–282.

[300] Asbury, G. R.; Hill, H. H. *Anal. Chem.* **2000**, *72*, 580–584.

[301] Roscioli, K. M.; Zhang, X.; Li, S. X.; Goetz, G. H.; Cheng, G.; Zhang, Z.; Siems, W. F.; Hill, H. H. *Int. J. Mass Spectrom.* **2013**, *336*, 27–36.

[302] Borsdorf, H.; Eiceman, G. A. *Appl. Spectrosc. Rev.* **2006**, *41*, 323–375.

[303] Kanu, A. B.; Dwivedi, P.; Tam, M.; Matz, L.; Hill, H. H. *J. Mass Spectrom.* **2008**, *43*, 1–22.

[304] Lalli, P. M.; Iglesias, B. A.; Toma, H. E.; Sa, G. F.; Daroda, R. J.; Silva Filho, J. C.; Szulejko, J. E.; Araki, K.; Eberlin, M. N. *J. Mass Spectrom.* **2012**, *47*, 712–719.

[305] Karpas, Z.; Cohen, M. J.; Stimac, R. M.; Wernlund, R. F. *Int. J. Mass Spectrom. Ion Process.* **1986**, *74*, 153–159.

[306] Retegan, M. mep.py (sourcecode), github repository. 2019.

[307] Grimme, S. *J. Chem. Phys.* **2006**, *124*, 034108–1–16.

[308] Kozuch, S.; Gruzman, D.; Martin, J. M. *J. Phys. Chem. C* **2010**, *114*, 20801–20808.

[309] Neese, F. *WIREs Comput. Mol. Sci.* **2012**, *2*, 73–78.

[310] Tang, C. Y.; Thompson, A. L.; Aldridge, S. *J. Am. Chem. Soc.* **2010**, *132*, 10578–10591.

[311] Fang, H.; Choe, Y.-K.; Li, Y.; Shimada, S. *Chem. - An Asian J.* **2011**, *6*, 2512–2521.

[312] Göttker-Schnetmann, I.; White, P. S.; Brookhart, M. *Organometallics* **2004**, *23*, 1766–1776.

[313] Spaulding, L.; Reinhardt, B. A.; Orchin, M. *Inorg. Chem.* **1972**, *11*, 2092–2094.

[314] Crotti, A. E. M.; Previdi, D.; Donate, P. M.; Scott McIndoe, J. *Inorganica Chim. Acta* **2020**, *508*, 119654.

[315] Rodriguez, J.; Dhanjee, H. H.; Buchwald, S. L. *Org. Lett.* **2021**, *23*, 777–780.

[316] Ting, M. Y.; Yunker, L. P.; Chagunda, I. C.; Hatlelid, K.; Vieweg, M.; McIndoe, J. S. *Catal. Sci. Technol.* **2021**, *11*, 4406–4416.

[317] Wei, R.; Hall, A. M. R.; Behrens, R.; Pritchard, M. S.; King, E. J.; Lloyd-Jones, G. C. *European J. Org. Chem.* **2021**, *2021*, 2331–2342.